Università di Pisa

DIPARTIMENTO DI INGEGNERIA CIVILE E INDUSTRIALE

Corso di Laurea Magistrale in Ingegneria Meccanica

THERMOPHYSICAL AND MECHANICAL CHARACTERIZATION OF ADVANCED MATERIALS FOR THE LHC COLLIMATION SYSTEM

Relatori:

Ch.mo Prof. Ing. Renzo Valentini

Ing. Michael Guinchard

Laureanda:

Laura Bianchi

II Appello anno 2017
Anno accademico 2015/2016

Acknowledgments

I would like to express my gratitude towards my supervisor at CERN, Eng. Michael Guinchard, who provided me trust and guidance during the months of internship in his laboratory, and to my thesis advisor Prof. Eng. Renzo Valentini of the University of Pisa for the valuable advices and support.

My colleagues added value to the work done, both for the scientific and cultural consultations, the professional recommendations and the friendly environment. Among them, I want to thank all the member of the MML of the EN department (Eugénie, Philippe, Morgane, Lucile, Luigi, Roland and Lukasz), particularly Óscar Sacristan de Frutos, for the constant availability and teachings. I wish to thank also Alessandro, Federico, Jorge and Inigo, for the daily exchange of information and collaboration.

At the end of this part of my life, I can say that school years would not have been the same without my friends Alice C., Alice L., Claudio, Leonardo, Margherita and Mattia, incomparable mates who shared with me intense days of study and cheerful moments.

Thanks to all the relatives and to the closer people, a source of encouragement and joy.

My life path could not have been possible without the day-by-day love, support and patience dispensed by my parents, Andrea and Maria Letizia, and my boyfriend, Andrea, who helped me facing any obstacle and gave me the most sincere and benevolent advices.

Ringraziamenti

Vorrei ringraziare il mio Professore Ing. Renzo Valentini dell'Università di Pisa, relatore di questa tesi, per avermi fornito supporto e consigli utili durante la redazione del lavoro e il mio supervisore al CERN, Ing. Michael Guinchard, per la sua guida e la fiducia riposta in me durante i mesi di stage presso il suo laboratorio di misure meccaniche.

Sono riconoscente a tutti i colleghi che, grazie agli scambi di opinioni scientifiche e culturali, ai consigli professionali e all'ambiente amichevole che hanno saputo creare attorno a me sin dal mio arrivo, hanno contribuito alla realizzazione della tesi. Ringrazio dunque tutti i membri del laboratorio di misure meccaniche del Dipartimento di Ingegneria (Eugénie, Philippe, Morgane, Lucile, Luigi, Roland e Lukasz) ed in particolar modo Óscar Sacristan de Frutos, mio mentore, per i dialoghi e gli insegnamenti quotidiani. Tra gli altri, ci tengo a ringraziare Alessandro, Federico, Jorge e Inigo per gli scambi di informazioni e la collaborazione quotidiana.

Ringrazio gli amici (di infanzia e di università), che hanno reso gli anni di studio più leggeri e mi sono rimasti vicini, nonostante la lontananza: Alice C., Alice L., Claudio, Leonardo, Margherita e Mattia.

Ringrazio i parenti e le persone che sono state al mio fianco e hanno creduto in me.

Infine, il mio ringraziamento più grande va ai miei genitori, Maria Letizia e Andrea, e al mio ragazzo, Andrea. Il loro amore e i loro consigli sono stati indispensabili: mi hanno dato la forza di inseguire i miei sogni, affrontare gli ostacoli ed intraprendere le mie scelte.

Abstract

The aim of the thesis is to describe the methods employed for the thermo-physical and mechanical characterization and to show the results of the campaign conducted over two ceramic matrix composites, CFC FS140® and MG-6403-Fc, which are candidates as jaws materials in the LHC collimation system. The work was conducted at the European Organization for Nuclear Research (CERN, Geneva), in the framework of the R&D activities done by the EN department. The goal of this project is to develop and characterize materials able to withstand highly energetic particles interactions to protect the accelerator's components and to clean the beam. In the first part of the thesis, the instruments employed for the thermal and mechanical analysis are studied, from the mathematical models to the standard test methods. These instruments are: horizontal push-rod dilatometer, differential scanning calorimeter, laser flash apparatus and universal testing machine. The results of the analysis show lower thermal and electrical conductivities of the CFC chosen, with respect with the one currently in use. The MoGR grade is in line with the previously developed ones, suggesting further improvement in the manufacturing process. The status of the collimators materials' development process after these characterization, sees the MoGR as baseline material for the primary and secondary collimators and the CFC to produce spares. Carrying out the campaign had been of paramount importance in understanding the physical principles and the technology behind the techniques, and to acquire experience in the thermo-physical and mechanical test engineering.

Riassunto

Lo scopo della tesi è quello di descrivere le tecniche impiegate per la caratterizzazione termofisica e meccanica di materiali innovativi nell'ambito della fisica nucleare, oltre a quello di presentare i risultati ottenuti dalla campagna su due compositi. Il lavoro, svolto presso l'Organizzazione Europea per la Ricerca Nucleare (CERN) di Ginevra, rientra nel progetto di ricerca e sviluppo finalizzato alla realizzazione di compositi avanzati per le ganasce dei collimatori dell'LHC. I test sono stati eseguiti nel Laboratorio di misure meccaniche della sezione EN-MME-EDM per mezzo di una macchina universale di trazione, un calorimetro differenziale a scansione, un dilatometro orizzontale e un apparato laser flash. I materiali investigati sono due compositi a matrice grafitica rinforzati l'uno con fibre di carbonio (CFC FS140®) e l'altro con carburi di molibdeno (MoGR, MG-6403-Fc). I risultati ottenuti mostrano come il CFC testato abbia conducibilità termica ed elettrica inferiori rispetto a quello attualmente impiegato nei collimatori, verosimilmente a causa dell'insufficiente temperatura finale di grafitizzazione. MG-6403-Fc mostra proprietà intermedie fra quelle dei due più promettenti gradi di MoGR finora sviluppati. La caratterizzazione svolta su questi due materiali ha permesso di ottenere importanti informazioni per il progetto di collimazione e di programmare le prossime tappe del lavoro di ricerca, oltre ad acquisire una più profonda conoscenza delle tecniche e un approccio critico alla scienza della misura.

Index

Introduction

This introductive chapter depicts the background of the R&D activities carried out by the Mechanical and Material Engineering group of the Engineering department, aiming at the development of novel materials for the upgrade of the LHC's collimation system. The aim and structure of the thesis are explained in the final paragraph.

Background

CERN: European Organization for Nuclear Research

After the Second World War, a small group of European physicists, inspired by the establishment of several international organizations, dreamed about a European laboratory for atomic physics aimed to unite the efforts of European scientists. Thanks to their vision, CERN (*Conseil Européen pour la Recherche Nucléaire*) was founded in 1954 in Geneva, Switzerland (see Figure 0.1), and today it counts 22 member states and leads what has become the largest particle physics laboratory in the world. Here, everyday physicists and engineers work together to find answers to some of the most ancient dilemmas that afflicted humanity: which are our origins? What is the structure of the matter?

These investigations are commonly carried out by means of particle accelerators, and at CERN it is possible to accelerate particles with the highest-energy particle accelerator in the world, the Large Hadron[1] Collider (LHC).

Figure 0.1 Aerial view of the CERN site and accelerator complex.

CERN's accelerator complex

The LHC is the last machine of a bigger complex (see Figure 0.2), consisting of a succession of smaller linear and circular accelerators with increasingly higher energies. The whole system is meant to prepare two counter-circulating proton (sometimes lead ions) beams starting from the extraction of hydrogen atoms from a bottle. The protons are first injected in the Proton Synchrotron Booster (PSB), and then sequentially in the Proton Synchrotron (PS) and Super Proton Synchrotron (SPS), where they reach the energy of 450 GeV[2]. (1) This downstream system of the LHC, also prepares the beam as a sequence of 2808 bunches, each one containing $1{,}1 \cdot 10^{11}$ protons, and injects them in the 27-km long LHC in two opposite directions

[1] Hadrons are particles made of quarks, like protons and ions.
[2] The electronvolt (eV) is the unit of measurement of energy generally used in particle physics. It represents the energy of an electron accelerated by a potential difference of 1 V. In SI units: $1\,eV = 1{,}602 \cdot 10^{-19}\,C \cdot 1\,V = 1{,}602 \cdot 10^{-19}\,J$.

(clockwise and counter-clockwise). The collisions between the two beams occur within 4 main experiments or detectors: CMS, ATLAS, ALICE and LHCb.

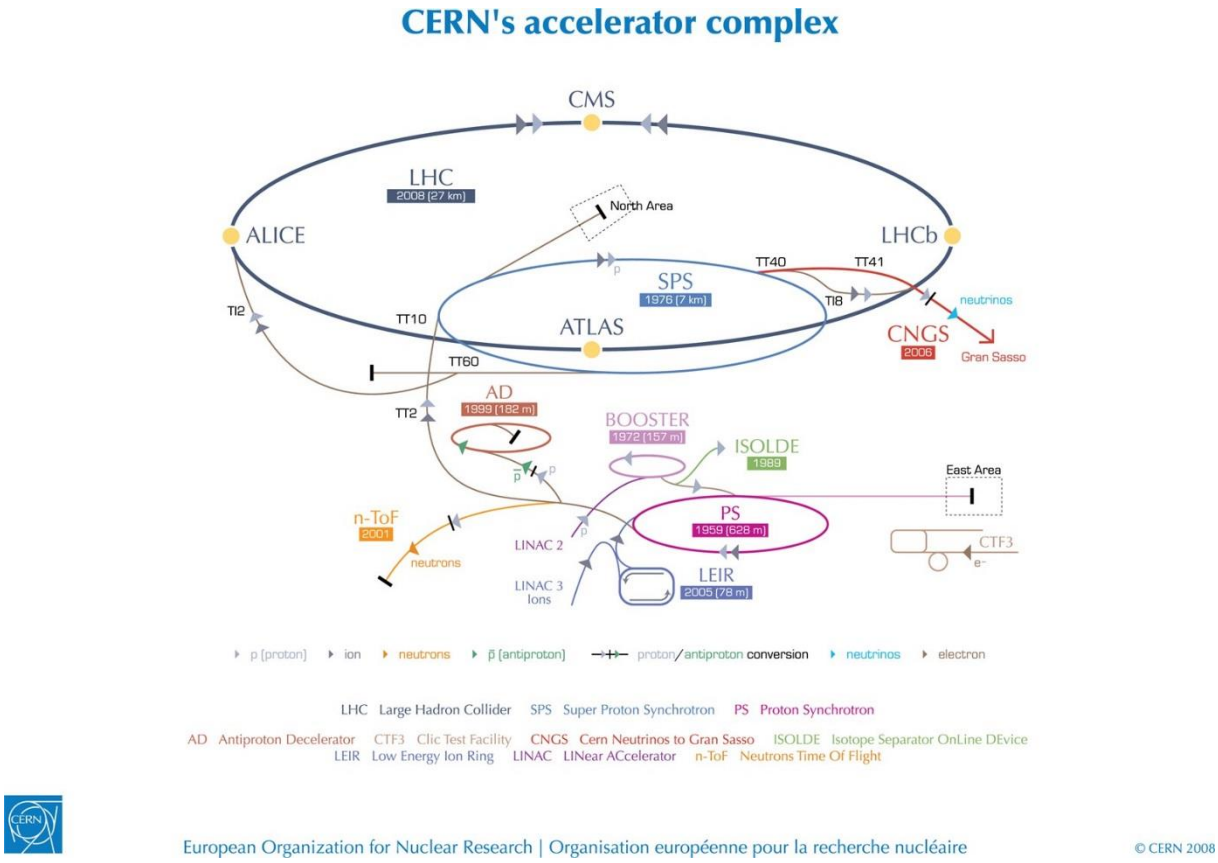

Figure 0.2 CERN's accelerator complex. Credits CERN.

The LHC

In the LHC, sixteen (eight per beam) Radio Frequency accelerating cavities accelerate the beams up to the energy of 7 TeV and their speed can reach 0.999999991 times the speed of light in vacuum. In SI units, each beam stores an energy of 362 MJ ($2808\ bunches \cdot 1{,}1 \cdot 10^{11}\ protons \cdot 7\ TeV = 362\ MJ$), enough to melt 498,4 kg of copper. (2)

More than 1200 superconducting magnets (dipoles, quadrupoles, sextupoles, octupoles, decapoles etc), operating between 1,9 K and 4,5 K, optimize the beams trajectories. Cryogenic temperatures are necessary to guarantee the superconductivity of the coils. For example, in the main dipoles, a temperature of 1,9 K (-271,3 °C) permits to decrease the electrical resistance of the niobium-titanium conductors allowing the circulation of 11.700 A of current and the generation of 8,33 T magnetic field. (3)

The superconducting magnets are sensitive to any kind of heating: an increase of temperature would lead to the passage from superconductivity to normal conductivity (magnet quench). The passage of nominal current would not be allowed and the temperature would increase further leading to catastrophic failure (as occurred during the accident of 2008).

During normal operation, a source of heating is represented by interactions between the magnets and beam intercepting devices and the beam halo. Hence, it has been fundamental to foresee a protective system, capable to reduce the beam losses and withstand the highest energetic particle beam: the Collimation system.

The Collimation system

The collimation system consists of more than 100 collimators mainly placed in the 3rd and 7th octant of the LHC (beam cleaning sections) and before and after the 4 main experiments (see Figure 0.3).

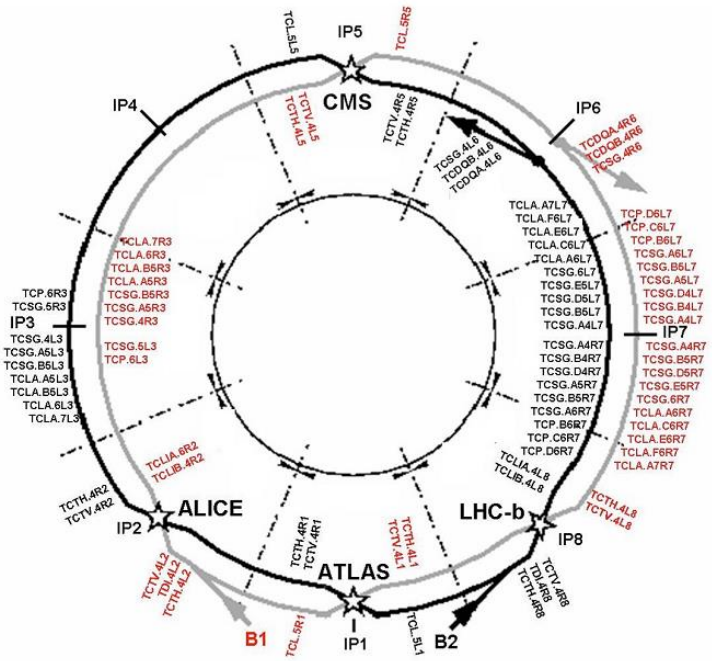

Figure 0.3 Position of the collimators in the LHC.

The collimators are Beam Intercepting Devices (BID) designed to accomplish two main functions:

- Beam cleaning: during normal operations, it is unavoidable to have beam losses, that due to particles deviating from the ideal trajectory and impacting the surrounding

components. As said, the interaction between these high energetic particles and the magnets can lead to magnet quenches. Thanks to two parallel jaws (see Figure 0.6), differently oriented in the collimators, which intercept the beam halo, only the core of the beam is let free to circulate. Figure 0.4 shows how the interaction between the halo and the primary collimator jaws origins a shower of secondary particles: for this reason, the collimation systems has been realized with a multi-stage cleaning architecture, relying on the properties of different jaws materials.

- Machine protection: this function is required in case of accident, when orbit errors occur.

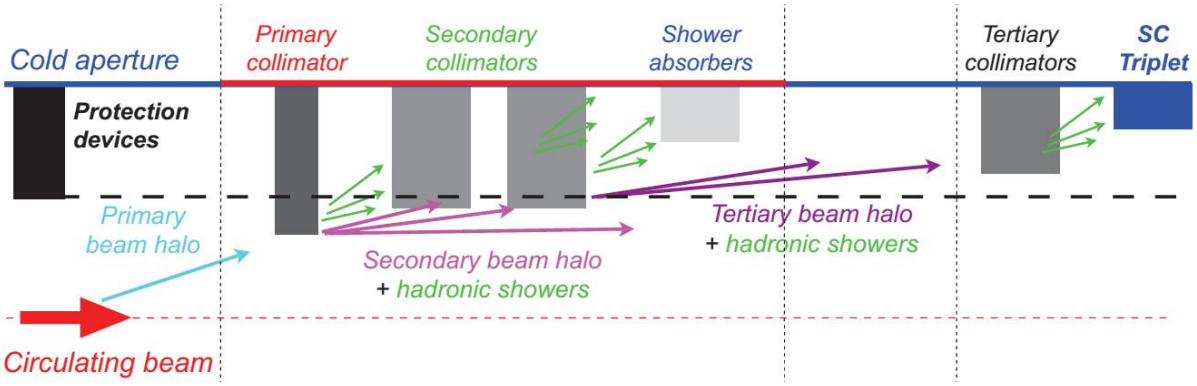

Figure 0.4 Interaction between beam halo and collimator jaws. Credits S. Redarelli. **(4)**

Among others, the following parameters influenced the design of the collimation system (see Figure 0.6):

- Radio frequency impedance: the electromagnetic field of the beam generates an electron cloud along the collimator, which interacts with the following beam and limit the LHC from reaching its maximum energy. Therefore, it is important to have a good charge evacuation (high electrical conductivity).
- Vacuum: the collimators environment is characterized by the ultra-high vacuum of the LHC ($10^{-13} atm$). This defines constraints regarding the outgassing rates and the maximum operational temperature of the jaws.
- Dimensional stability: flatness (100 µm over 1 m), reproducibility of jaw settings and knowledge of the collimator gap (<50 µm) are of paramount importance for the beam cleaning and stability (see Figure 0.5).

- Maintenance and reliability: to allow safe working condition for the operators in case of maintenance, the whole design and choice of the material properties should minimize the dose rates.

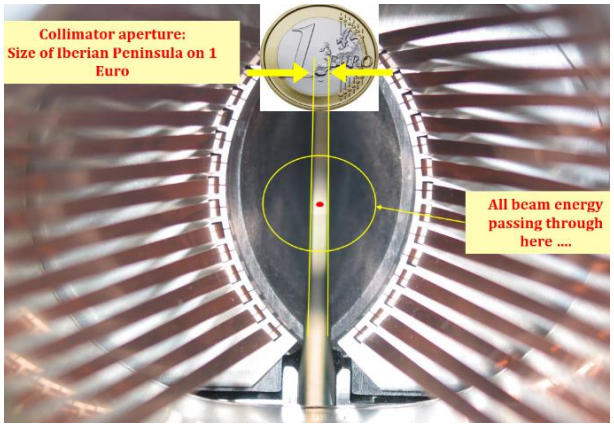

Figure 0.5 Front view of the collimator jaws showing the aperture.

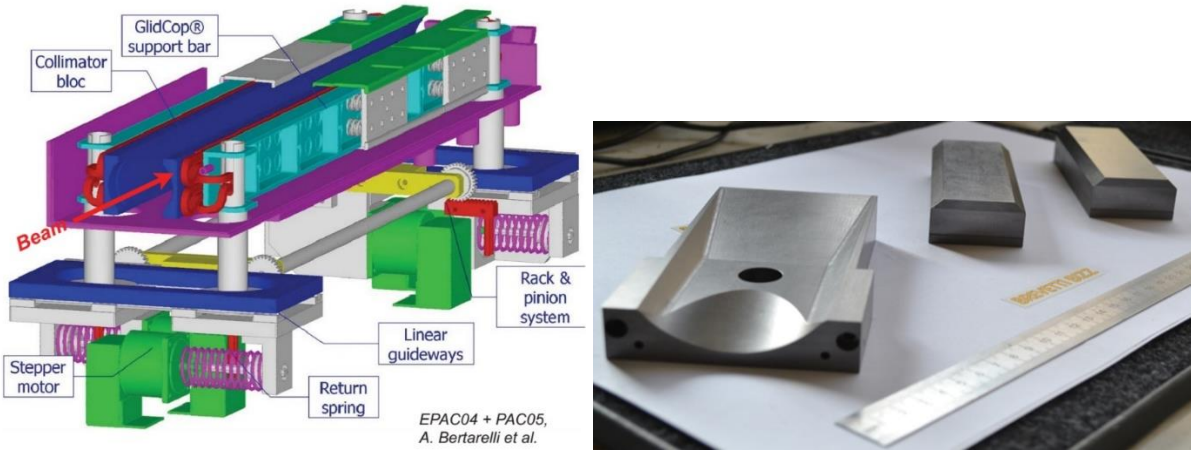

Figure 0.6 Assembly of a collimator and collimator blocks.

Aim and structure of the thesis

This work contains the scientific background and the results of the activities carried out during a working period at the Mechanical measurement laboratory (EN-MME-EDM) of CERN as Technical student. The scope of the job was to perform the thermo-physical and mechanical characterization of novel materials, mainly aimed at the upgrade of the collimators, specifically used for the jaws of the primary and secondary collimators. In fact, the upgrade of the current collimators is necessary to face the higher beam energies foreseen by the HiLumi LHC. The

HL-LHC project targets an increment of the luminosity[3] of the accelerator, increasing the energy of the beam from $362\ MJ$ to $692\ MJ$ by 2020. The thermo-physical characterization was carried out by means of a differential scanning calorimeter, a push-rod dilatometer and a laser flash apparatus. The mechanical tests were performed with a universal testing machine and impact excitation technique.

The first two chapters describe the state of the art of the materials object of the thesis (MoGR and CFC), including a general overview of the figures of merit, and of the instruments and techniques used for the measurements.

Chapter 3 represents the experimental part of the work and describes two of the materials tested during the working period and the devices employed, with reference to the international standards.

The results of the characterization campaign are shown in the fourth chapter and their analysis is developed in the fifth one.

The final chapter concludes the work and outline the future developments following the activities carried out.

[3] One of the most important parameter of an accelerator is the luminosity, which indicates the number of collisions that occur in a certain period. The higher the luminosity, the higher the number of collisions and therefore the quantity of data and the probability to observe rare events. To increase the luminosity, it is possible to increase the number of hadrons per bunch and/or to squeeze them in the smallest amount of space.

1 State of the art: materials

The thesis work focuses on the thermo-physical and mechanical characterization of two materials: carbon fibers - carbon (CFC FS140®) and molybdenum graphite (MoGR, MG-6403-Fc), a molybdenum carbide - reinforced ceramic matrix composite (CMC). Both materials have a graphitic ceramic matrix. The reinforcement, also ceramic, is provided by carbon fibers in the CFC case and by molybdenum carbide in the MoGR. After introducing the Figures of Merit, defined to evaluate the performances of the material when embarked in a collimator, the predecessors of the two families of materials tested are described. In the final part, a full overview of the materials currently employed in the collimators is depicted.

1.1 Figures of Merit

During the past years, several Figures of Merit (FoMs) have been defined to evaluate and rank the candidate materials, taking into account the harsh environment and the requirements that the collimators need to withstand. In a recent paper (5), four indexes relying on constant temperature-independent material properties are proposed (for anisotropic materials the averaged values in the three directions are considered):

- *Thermomechanical robustness*: this index assesses the material robustness against particle beam impacts. When a particle hits a structure, it transfers instantaneously its kinetic energy to the impacted body under the form of heat. Thermal shock problems

can then occur to the impacted material, which experiences a sudden temperature change and induced thermal stresses and deformations. This index is based on both the admissible strain, or strain to failure ε_{adm}, and the melting temperature T_m of the material:

$$\mathrm{TRI} = \frac{\varepsilon_{\mathrm{adm}}}{\varepsilon_{ref}} \cdot \left(\frac{T_m}{\Delta T_q} - 1 \right)^m \quad \textbf{1.1}$$

Where m is a coefficient related to the material softening with a temperature increase, ε_{ref} and ΔT_q are the strain and the temperature increase generated by a reference beam impact:

$$\varepsilon_{\mathrm{adm}} = \frac{R_M}{\bar{E}\,(1-\upsilon)} \quad \textbf{1.2}$$

$$\varepsilon_{\mathrm{ref}} = \bar{\alpha}\,\Delta T_q \quad \textbf{1.3}$$

$$\Delta T_q = \frac{C_R \rho^n}{c_p X_g} \quad \textbf{1.4}$$

Where $\bar{E}$ is the average Young's modulus, υ the Poisson's ratio, $\bar{\alpha}$ the average CTE, c_p the specific heat, X_g the geometric radiation length, C_R a scaling factor and n a constant related to the energy distribution generated by the impact (empirically observed to be ~0.2). It is worth to notice in equation 1.4 that the energy deposited by the beam and therefore the temperature rise, is directly proportional to the density.

- *Thermal stability*: this parameter gives an indication of the geometrical stability of the material under steady-state particle losses. Differently from the TRI, the TSI is related to an equilibrium scenario with the heat slowly deposited on the material and evacuated through a cooling system. The TSI is therefore strongly related to the heat evacuation capacity of the material, and therefore its thermal conductivity, and is proportional to the radius of curvature of an elongated structure induced by a non-uniform temperature distribution.

$$TSI = \frac{\bar{\lambda}\, X_g}{\bar{\alpha}\, C_s\, \rho^n} \quad \textbf{1.5}$$

where $\bar{\lambda}$ is the average thermal conductivity and C_s a scaling factor.

- *Electrical conductivity:* this property must be maximized in the collimators to minimize the Radio Frequency impedance (as explained in the Introduction). In fact, the collimators are the devices closest to the beam and their contribution to the whole LHC impedance is the highest.
- *Radiation resistance*: irradiation of materials by energetic particles causes microstructural defects which translate into a degradation of the thermo-physical properties. Radiation resistance is defined as the ability of the material to maintain its properties under and after irradiation.

The FoMs are an efficient tool to quickly predict the behavior of a material when embarked in a collimator. For a more precise estimation, however, the response of the material under the particle beam is usually precisely evaluated by numerical methods, which makes use of material models where the key thermo-physical and mechanical properties are expressed as a function of the temperature. The properties required by the models were therefore extensively measured during the characterization campaign detailed in this work.

1.2 Graphite

Graphite is a ceramic material and represents one of the allotropes of carbon. It is made of a continuous stack of graphene planes, a structure where C atoms are arranged in a honeycomb cell, forming covalent bonds with other three atoms. The graphene layers are bonded together by weak Van der Waals forces, which for this reason can easily slide on top of each other. On the other hand, it presents high strength, stiffness and low coefficient of thermal expansion (CTE) in the planar direction, thanks to the covalent bonds. Despite being a ceramic material, it shows good electrical conductivity along the graphene layers (higher than $2\ MS/m$ for ideal graphite along the basal plane). Graphite is the most stable form of carbon on Earth in standard conditions. Commercial graphite has worse properties than the ideal crystal (Figure 1.1), because it contains defects and it is polycrystalline.

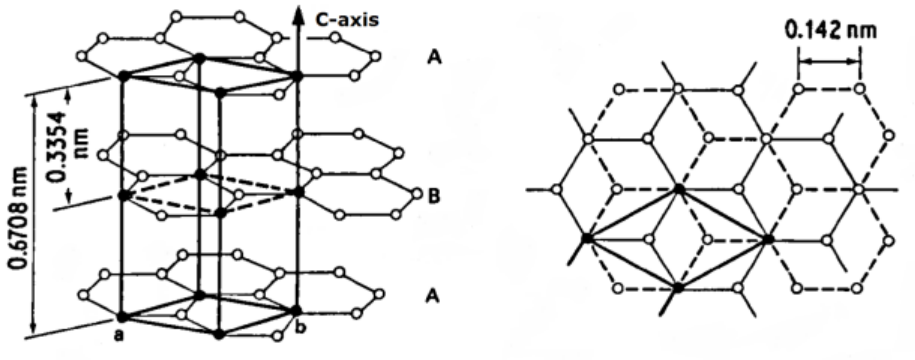

Figure 1.1 Graphite structure **(6)**.

Graphite occurs in nature in metamorphic and igneous rocks and it can be produced artificially processing petroleum, coal or pitch coke. Artificial graphite production starts from raw material that is ground up, bound and heated above its softening point. At this point, the material can be variously shaped by extrusion, molding or isostatic pressing. The crystals are oriented according to the process adopted. For examples, extrusion is chosen to produce carbon fibers. The following step is the carbonization, which consists in the decomposition of organic compounds into carbon through baking at $700 \div 1000$ ℃ (with simultaneous elimination of volatile components). The final phase is the graphitization, consisting in heating up to 3000 ℃ in an electric kiln for up to 3-weeks time: at this temperature, the carbon atoms are arranged in the graphitic crystalline structure.

1.3 Ceramic matrix composites

This family of composites, produced by sintering technique, features a ceramic matrix and a second ceramic phase as a reinforcement. The advantages of a ceramic matrix are: high hardness, chemical stability, high melting temperature and thermal stability. On the other hand, it confers low electrical conductivity and brittleness to the composite. For these reasons, they are commonly used as small insert for cutting tools, while for collimator applications their electrical conductivity is not high enough. The reinforcements are usually ceramics in form of fibers, which add stiffness and strength. The main parameters to be defined in this family of composites are the quantity of reinforcement, its shape, dimension and orientation, the quality of the interface and the porosity.

1.4 Conventional reference system

Before dealing with the details of the collimators materials, it is important to introduce the reference system conventionally adopted to refer to the collimator geometry, to the manufacturing process, to the preparation of the samples and to the main direction of the composites. The three directions are depicted in Figure 1.2.

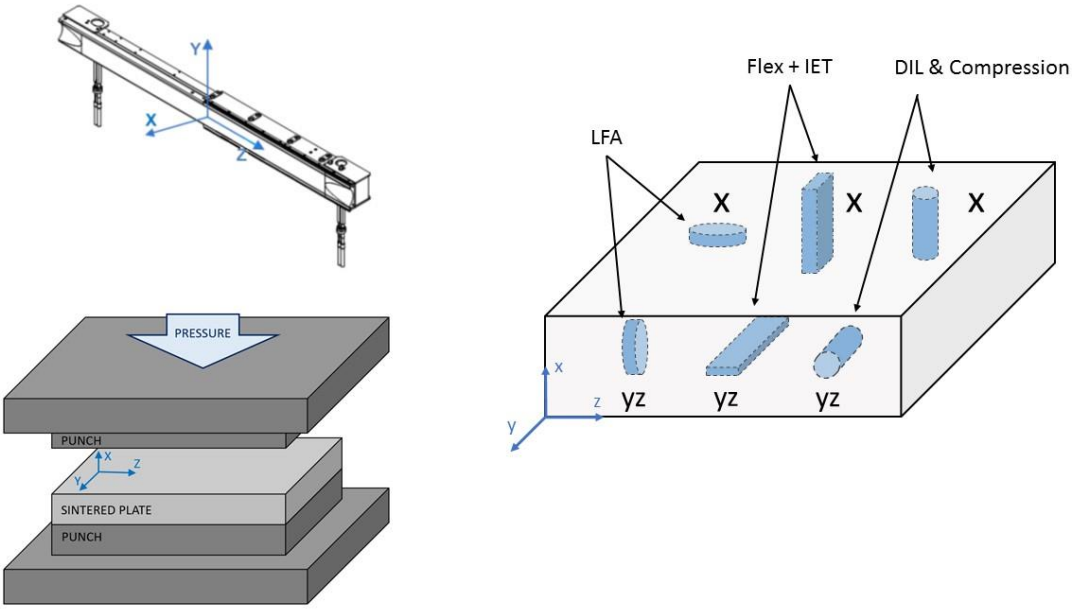

Figure 1.2 Reference system adopted for collimator, manufacturing process and sampling.

- x: direction perpendicular to the plane of the jaw
- y: direction in the plane of the jaw, perpendicular to the beam
- z: direction in the plane of the jaw, parallel to the beam.

During the hot-pressing procedure, the pressure is applied in direction x.

The samples are cut along two directions: they have their axis either parallel to x (hereafter identified by the index x) or in the plane yz (hereafter called yz samples).

1.5 Carbon fiber – Carbon composites

1.5.1 CFC fields of use

Reinforced carbon – carbon is appropriate for a wide range of high temperature applications where a high thermal shock resistance, high thermal diffusivity and low CTE are required: a famous example is its usage for the conical nose of the Space Shuttle. Since the 1970s it has

been adopted in the brake disks of Formula One cars. Other typical applications are in electronics, in energy production (armor tiles of nuclear plants), and to build components of heat treatment furnaces.

1.5.2 CFC AC150®

The CFC currently used in the collimators (AC150 manufactured by the Japanese Tatsuno[4]) is a 2D composite with 40% carbon fibers randomly disposed in a graphite matrix to create several layers parallel to the yz plane (see Figure 1.2). The jaws had been hot-rolled to confer slightly different mechanical properties along the two planar directions, as shown in Table 1.1. The resulting material is orthotropic with different properties along the pressing direction and along the two perpendicular directions. It has been chosen in 2004 for the primary and secondary collimators thanks to its low CTE and best compromise between low electrical resistivity and high strength.

Property	**Unit**	**Value**		
Density	[g/cm^3]	$\rho = 1.885$		
Specific Heat	[J/kgK]	$c_p = 712$		
Young Modulus	[GPa]	$E_{xx} = -$	$E_{yy} = -$	$E_{zz} = 62$
Shear Modulus	[GPa]	$G_{xy} = 2.16$	$G_{xz} = 33$	$G_{yz} = 33$
Poisson's Ratio	[-]	$\upsilon = 0.16$		
Flexural Strength	[MPa]	$R_{Fl,x} = 10.3$	$R_{Fl,y} = 104$	$R_{Fl,z} = 139$
Coefficient of Thermal Expansion	[10^{-6} K^{-1}]	$\alpha_x = 11$	$\alpha_y = -0.8$	$\alpha_z = -0.8$
Thermal Conductivity	[W/mK]	$\lambda_x = 54$	$\lambda_y = 233$	$\lambda_z = 304$
Electrical Conductivity	[MS/m]	$\sigma_x = 0.03$	$\sigma_y = 0.18$	$\sigma_z = 0.24$

Table 1.1 CFC AC150® properties at room temperature along the three directions defined in 1.4.

The production of CFC follows a process similar to graphite, with the addition of the reinforcing carbon fibers (Figure 1.3).

[4] http://www.tatsunojapan.com/

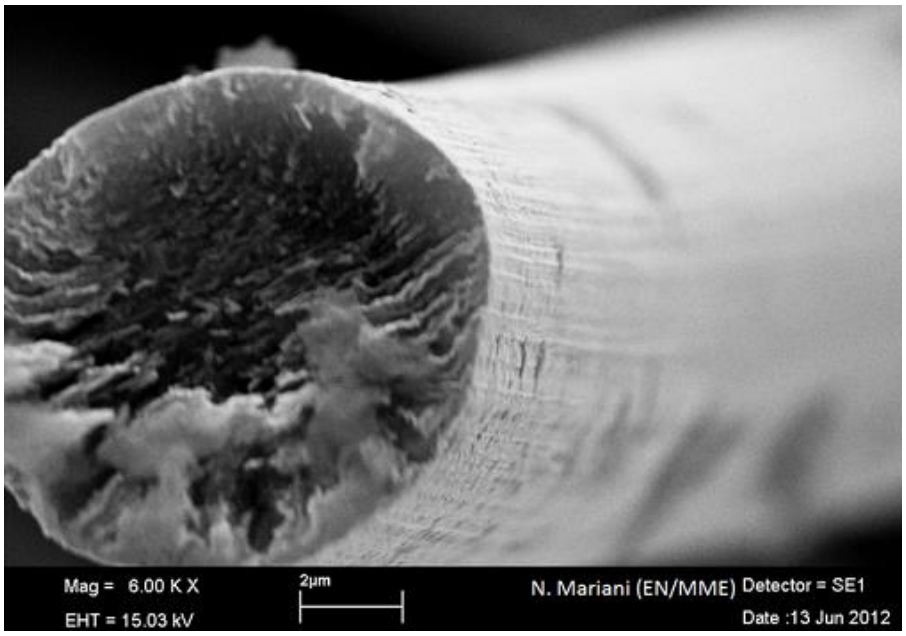

Figure 1.3 Image of a pitch-derived carbon fiber.

1.6 Molybdenum carbide – Graphite composites

1.6.1 R&D

In recent years, a R&D program has been launched at CERN with the aim of developing novel materials for the collimators: the requirements of these protective devices have become more compelling in view of the upgrade of the LHC (HL-LHC) and, even more, of the proposed construction of the FCC (Future Circular Collider[5]). For example, the CFC currently used in the primary and secondary collimators might limit the full exploitation of the HL-LHC potential, due to its high RF impedance induced by its very low electrical conductivity. The novel materials shall optimize the combination of FoMs and efforts have been done to find a compromise between the excellent properties of available graphitic materials, such as low density, high thermal stability and low thermal expansion, and those typical of metals or transition metal-based ceramics, such as high mechanical strength and high electrical conductivity. CERN, partly within the EuCARD collaboration, involved several partners from the academic, technology and industrial sectors and developed new advanced materials, among which the most promising are:

[5] The FCC, Future Circular Collider Study aims to reach collision energies of 100 TeV, by means of a 80-100 km long accelerator. https://fcc.web.cern.ch/Pages/default.aspx

- Copper – Diamond (CuCD): it is a diamond-reinforced Metal Matrix Composite (MMC) produced by Rapid Hot-Pressing (RHP) of copper with addition of synthetic diamonds and boron (initial volume composition: 60% diamonds, 39% copper, 1% boron). The resulting composite has very good thermal and electrical conductivity, and the CTE is $0.33 \div 0.5$ times that of pure copper. The disadvantages are the difficulties in the machining, the high brittleness in respect to copper and the low melting point (copper melts at 1084 °C).
- Molybdenum Copper – Diamond (MoCuCD): this material was developed to improve the mechanical strength of CuCD and decrease the CTE. This MMC is also obtained by RHP technique, with the addition of Molybdenum as a third element. Despite the efforts, the material presents good thermal conductivity and compaction but still brittle behavior and slightly higher CTE.
- Molybdenum carbide – Graphite composite (MoGR): due to the high density and the low melting point of Cu-based materials, the research focused on a family of graphitic composites molybdenum carbide – based. Graphite shows a number of advantages over diamond: it has lower density, it represents the most stable form of carbon, while diamond is metastable and converts into graphite when heated, and it is less expensive. Molybdenum carbide has been chosen because of its refractory nature with promising properties up to 2000 °C. More details about the development of this material are included in the following paragraph.

1.6.2 MoGR

The first studies over metal carbide – graphite composites were carried out in the 1960s by NASA (7): the molybdenum-graphite investigated had a brittle behavior and low mechanical strength. In 2012, CERN established a cooperation with the Italian company BrevettiBizz[6] (Verona, IT) to develop the production of this composite. Since then, several grades of MoGR have been realized and tested. A broad range of parameters has been tested: composition, powder types (spheroidal natural graphite flakes with or without addition of mesophase pitch-derived carbon fibers), dimensions (average graphite flake diameter 45 µm, molybdenum powder between 5 - 45 µm and carbon fibers in the range 250 µm – 3 mm) and processing cycle.

[6] http://www.brevettibizz.com/

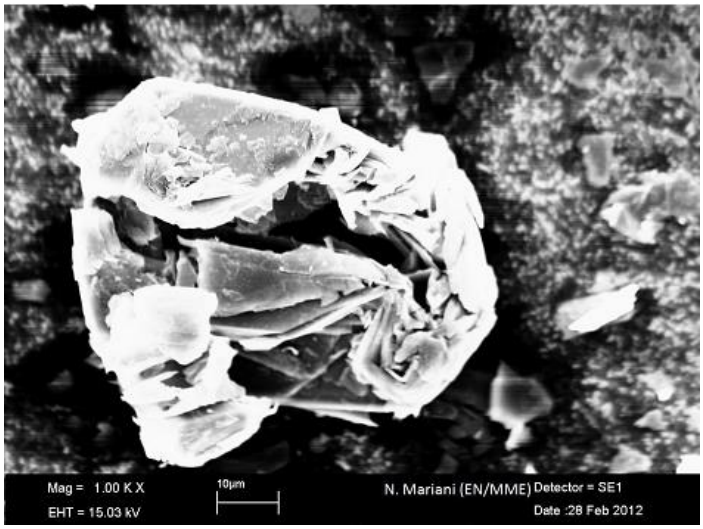

Figure 1.4 SE image at high magnification of a graphite flake.

Production

The composite is produced by powder metallurgy technology, with the hot-pressing technique. At the beginning of the material development, the solid phase sintering technique, based on the diffusion of C atoms inside the Mo BCC lattice interstitial, was adopted, exploring a range of temperatures below the melting point of the carbides. The technique has then been abandoned because of the better results obtained with a liquid phase sintering. The first step in the production is the preparation of the green body by compaction of the powders at room temperature applying a pressure of 300 MPa.

Figure 1.5 Hot-pressing machine at BrevettiBizz.

The green body is then housed in a special graphite mold made by two punches and a jacket, and the sintering cycles are performed thanks to a hot-pressing sintering machine (see Figure 1.5), which applies a pressure of 35 MPa and can reach temperatures higher than 2600 °C inside the mold. The process is called Spark Plasma Sintering (SPS), also known as Field Assisted Sintering Technique (FAST) or Pulsed Electric Current Sintering (PECS): the heat generation is produced internally in the sintered material by the passage of a large electric current, which induces energy losses by Joule effect. The sintering temperature is above the eutectic Mo-C corresponding to a content of C of 45% and a temperature of 2589 °C (see Figure 1.6). The liquid phase allows a mechanism called catalytic graphitization by dissolution and diffusion of carbon atoms, typical of Metal Carbide-Carbon composites (8) (6): C atoms dissolve and diffuse in the liquid carbide and the graphite crystallites can grow and bond between themselves. The applied uniaxial pressure orients the composite structure, which results transversely isotropic: the graphite planes are oriented perpendicularly to the pressing direction.

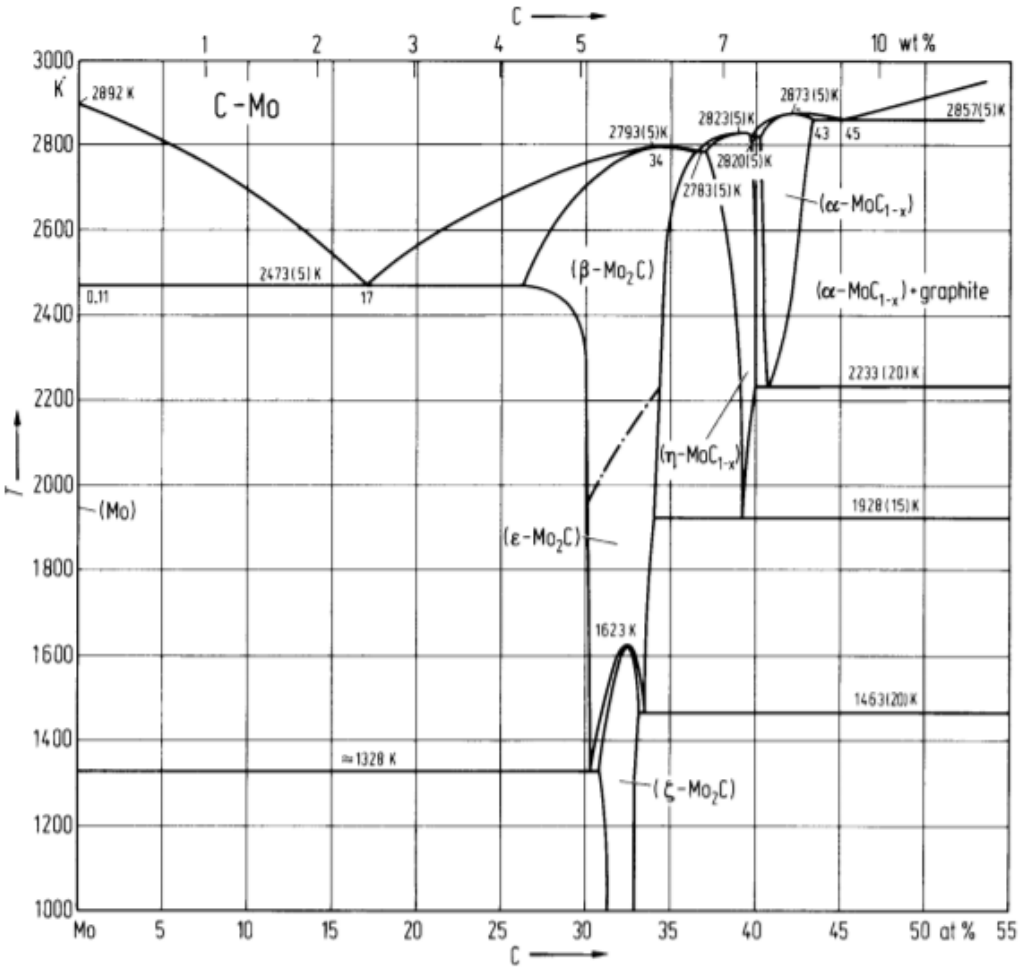

Figure 1.6 Molybdenum-Carbon phase diagram. The eutectic temperature $MoC_{(1-x)}$-graphite is at 2857 K (2584°C) (45 at% C)

During the melting of the carbides, part of the liquid phase spills out of the mold: being difficult to quantify this amount, also the final porosity and the actual metal content are difficult to calculate, they can be estimated a posteriori with microscopy analyses performed on the final material. Another parameter which is difficult to determine is the temperature inside the mold: in fact, the temperature during the sintering process is measured by means of a pyrometer reading the temperature of the lower punch: however, it is possible to know that the eutectic point is reached and melting occurs because of the abrupt change in height (change of density) of the plates. The sintered plate (see Figure 1.7) is extracted from the molds and submitted to a pressure-less heat treatment in order to release its internal stresses. The composition and production parameters of two MoGR grades are presented in Table 1.2, while their properties are reported in Table 1.3.

Figure 1.7 MoGR sintered plate.

Parameter	**Unit**	**MG-6403-Ga**		**MG-6541-Aa**	
		S	**PS**	**S**	**PS**
Estimated T	[°C]	2600	2100	2600	2100
Time	[s]	1200	3000	1200	3000
Pressure	[MPa]	35	0	35	0
Atmosphere		$10^{-1}\ mbar\ N_2 + H_2$		$10^{-1}\ mbar\ N_2 + H_2$	
Vol. Mo	[%]	4.5		4.3	
Vol. GR	[%]	95.3		90.9	
Vol. CF	[%]	0		4.75	
Vol. Ti	[%]	0.2		0.05	

Table 1.2 Process and composition parameter for two different grades of MoGR. S = sintering, PS = post sintering phases.

The graphite powder used is a crystalline powder graphite with spheroidal flakes provided by Asbury Carbons Company. The average particle size is 45 μm and at least 90% of the particles

ranges between 20 and 80 μm. Molybdenum and titanium particles are in average 5 μm and the purity of the powder is above 99.9%. Titanium is added as phase stabilizer dopant.

1.7 Current collimator materials

Besides the already described CFC, the other materials currently embarked in the collimator jaws are:

- Tungsten heavy alloy (Inermet180): it is obtained by liquid phase sintering of powders (95% W, 3.5% Ni and 1.5% Cu in weight). The Ni-Cu phase melts and infiltrates the voids between W grains. It is used in the tertiary collimator jaws and exhibits good thermal and mechanical properties combined with a high density: for these reasons, it is an efficient particles absorber.
- Dispersion-strengthened copper (Glidcop Al-15): its production is based on the powder metallurgy. A fine dispersion of nano-metric alumina particles inside Cu grains is realized, mixing together a pre-alloyed powder of Cu with small concentration of Al and fine copper oxide powder. The mixture is compacted and cold worked by extrusion to reduce Cu grain size. The alumina blocks the propagation of the dislocations maintaining good mechanical properties at high temperatures (it is the Cu alloy which presents the highest resistance to creep), whilst the thermal properties remain closed to those of pure Cu. Glidcop was initially candidate for the HL-LHC secondary collimator absorber, but its high density determined its rejection. Conversely, it is employed in the jaw support bars (see Figure 0.6) because it maintains high yield stress after brazing and because this component is not impacted by protons, therefore higher densities are not problematic.

The properties of the materials described in this chapter are collected in the following Table 1.3.

Property	Unit	CFC AC150®	Inermet180	GlidcopAl-15	MG-6403-Ga		MG-6541-Aa	
		ROM			yz	x	yz	x
Density	[g/cm^3]	1.885	18	8.93	2.49		2.49	
Melting Temperature	[°C]	3650	1400	1083	2589		2589	
Specific Heat	[J/kgK]	712	150	391	604		643	
Elastic Modulus	[GPa]	62	360	130	65	4.1	73	4.7
CTE	[10^{-6} K^{-1}]	3.9	5.25	16.6	2.03	9.26	2.3	10
Thermal Conductivity	[W/mK]	197	90.5	365	547	56	507	45
Electrical Conductivity	[MS/m]	0.14	8.6	53.8	0.88	0.08	0.98	0.06
TRI	[-]	1596	0.6	5.3	274		267	
TSI	[-]	54	0.1	0.8	43.3		37	

Table 1.3 Tables of properties and FoMs at room temperature for the aforementioned materials. Note that while for the MoGR grades the properties are given for the two direction of anisotropy, the values for CFC results from the ROM (rule of mixtures) average. For CFC properties along its main direction see **Table 1.1**

2 State of the art: methods

This Chapter introduces the thermo-physical and mechanical properties necessary to characterize the materials candidate for the production of the primary and secondary collimators jaws and to optimize the finite element models for simulations. After an overview of the techniques developed for their measurements, those adopted by the Mechanical measurement laboratory of CERN are described.

2.1 Thermo-physical properties and their measurement

2.1.1 Specific heat

The relationship between enthalpy, temperature and pressure for a substance can be written as:

$$dh = c_p dT + B_h dp \tag{2.1}$$

Where

$$c_p = \left(\frac{dh}{dT}\right)_p \qquad B_h = \left(\frac{dp}{dT}\right)_h \tag{2.2}$$

c_p is a thermodynamic coefficient called specific heat at constant pressure. To understand its meaning consider the case of a system free to expand subjected to a source of heat q at constant pressure ($dp = 0$). In this case the variation of energy u is:

$$du = dq - pdv \quad \textbf{2.3}$$

Where $-pdv$ represents the work of dilatation (negative because done by the system on the outside), dv being the variation of volume of the system. Remembering the definition of enthalpy $h = u + pv$ and substituting in equation 2.1:

$$dq = c_p dT \quad \textbf{2.4}$$

Hence, c_p can be read as the ratio between the heat inputted in a system and its change of temperature. Its unit of measurement in SI units is $\frac{J}{kgK}$, so an equivalent definition is that the specific heat represents the amount of heat needed to increase the temperature of a unitary mass of 1 degree Kelvin.

2.1.2 Methods for measuring the specific heat

The specific heat is usually measured with an instrument called calorimeter which is also able to measure the heat of chemical reactions and phase changes. One of the first calorimeter used to measure specific heat was Regnault's calorimeter (Henry-Victor Regnault, 1810-1878) composed by a dewar containing water and the examined substance: the water is mixed and its temperature measured with a thermometer. The c_p of the substance is calculated from the variation of temperature of the water:

$$m_w c_{pw} \Delta T = m_s c_{ps} \Delta T$$

Many different types of calorimeter have been developed and the one of interest for this thesis is based on the differential scanning calorimetry and is detailed in the following paragraph. Another method to determine the specific heat is the laser flash technique, also used for measuring the thermal diffusivity, and described in paragraph 2.1.6. The latter is a comparative method which leads to reliable results only if the same amount of heat is provided to both a reference sample and the unknown sample, condition which is hardly achieved.

Differential scanning calorimetry

When a sample is subjected to a linear temperature program, Equation 2.4 express how the heat flow rate into the sample is directly proportional to the material specific heat. The principle of the differential scanning calorimetry consists in measuring the heat flow of both the unknown material and a reference sample to determine the specific heat as a function of temperature. In a differential scanning calorimeter (DSC, see Figure 2.1), a sample holder containing two symmetrical measuring cells is housed inside a furnace, and subjected to a linear temperature program preceded and followed by isothermal steps (see Figure 2.2). Each of the measuring cells hosts a closed pan: one of them is always empty while the other contains the sample material. The measuring cells are fitted with thermocouples connected in series. Hence, the output signal will be proportional to the difference of temperature of the measuring cells.

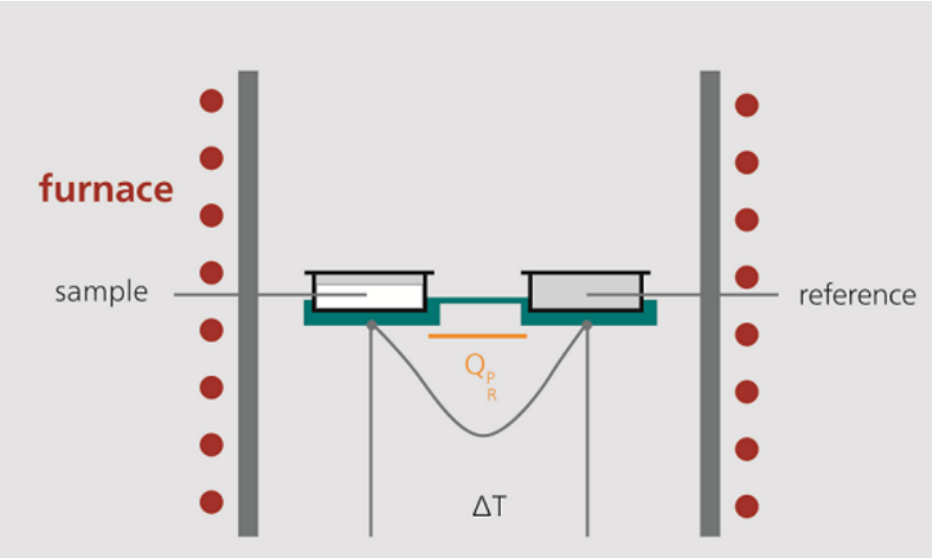

Figure 2.1 Schematic of a DSC. Credits NETZSCH.

Before measuring the standard and the unknown sample a baseline measurements is necessary to establish the thermal capacity of the instrument itself: this is carried out with empty pans. When the temperature starts increasing there may be an offset from the isothermal baseline due to different thermal capacities of the two sample holders. Once the baseline is determined the sample is placed in the pan and subjected exactly to the same temperature program: once again, during the ramp there will be an offset from the isothermal signal due to the heat absorption of the material. In Figure 2.2 the difference of area subtended for the materials and baseline offset represents the change in heat content $\Delta Q = \int_{t_1}^{t_2} \frac{dq}{dt} dt$.

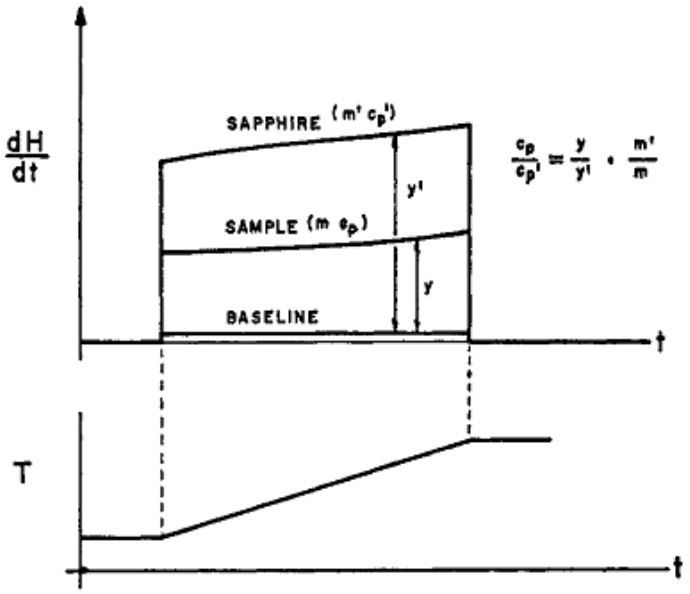

Figure 2.2 Temperature program and calculation of c_p. **(9)**

The measurements of both the unknown material and of a standard with a well-known specific heat (like sapphire or POCO-graphite) allows the determination of c_p as follows:

$$\frac{c_p}{c_p'} = \frac{m'y}{my'} \qquad \textbf{2.5}$$

Where y and y' are the coordinate deflections for sample and standard respectively.

2.1.3 Coefficient of thermal expansion

All the materials change their dimension whenever a temperature change occurs: this fact is fundamental in the design of components subjected to temperature changes, because the way they react to temperature changes and the way they are constrained reflects on their state of tension and deformation. The coefficient of thermal expansion expresses the expansion of the material with temperature as the fractional increase in length per unit rise in temperature.

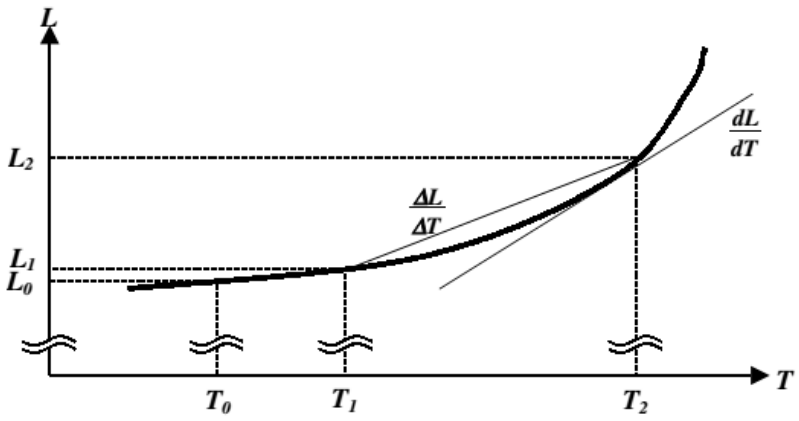

Figure 2.3 Length of the sample as a function of temperature.

Figure 2.3 shows the change in length of a material with the temperature. The coefficient of thermal expansion can be variously defined, but the two most common expressions are:

- Average coefficient of thermal expansion (CTE): this parameter refers to a temperature range measured starting from a reference temperature T_0 that must be stated.

$$CTE(T) = \frac{\frac{L_2 - L_0}{L_0}}{(T_2 - T_0)} = \frac{1}{L_0}\frac{\Delta L}{\Delta T} \qquad \textbf{2.6}$$

  Where L_0 is the length at the reference temperature. This value can be seen as the slope of the secant the points corresponding to T_2 and T_0 on the expansion curve.

- Thermal expansivity: this definition refers to a single temperature and is the slope of the tangent to the curve of expansion in the point of interest. This is the limit of equation 2.6 when T_2 and T_0 come closer.

$$\alpha_t = \frac{1}{L}\frac{dL}{dT} \qquad \textbf{2.7}$$

The coefficient of thermal expansion is a temperature dependent property: typically increasing with the temperature. Its SI unit is K^{-1}: common values for metals and alloys are within $10\ 10^{-6}$ to $30\ 10^{-6}\ K^{-1}$, while ceramics range from $1\ 10^{-6}$ to $20\ 10^{-6}\ K^{-1}$.

2.1.4 Methods for measuring the coefficient of thermal expansion

To measure this property, it is needed to sense both the displacement and the temperature. The displacement measurement can rely on several physical principles which are at the base of the following, suitable for different situations:

- Mechanical dilatometry: the displacement of the sample resulting from the temperature change is transmitted mechanically to a sensor, like a linear variable differential transformer (LVDT). Typically, the displacement is transmitted by one or 2 rods (push-rod dilatometers), that are in contact with the sample. The contact between the rod and the sample is guaranteed by a tracking force, in the horizontal configuration, and by their own weight in the vertical set-ups. The sample is embedded in a furnace, big enough to produce a uniform heating along the specimen. During the measurements, also the components of the instrument (rods and sample holder) are subjected to heating/cooling and expand/contract accordingly: accurate results can only be obtained if the material of the set-up is suitable. For temperatures up to 1000 ℃ (or lower depending on affinity with the tested materials) vitreous silica is suggested. At higher temperatures alumina and isotropic graphite are recommended: it is important that both tube and rods are produced from the same batch of material with the same orientation. The temperature can be measured with thermocouples of pyrometers.
- Optical method: the dimensional change in the samples is measured optically with different techniques, that can be identified as follows:
    - Optical imaging: this absolute technique of measurement is based on the tracking of the spatial movement of images, which are targets of the samples, such as its extremities, machined grooves, holes or indentation or pins attached. The targets are viewed in a direction perpendicular to the displacement by optical sensors. The illumination of the targets can be done from the front (image created by the reflected light) or from the rear (image created by the profile). Good results are obtained when the temperature is uniform between the targets or when the gradient can be determined.
    - Optical interference: this method measures the distance between 2 points in terms of number of wavelengths travelling parallel to the direction of displacement. It represents an absolute method if the sample chamber is under vacuum, when there is no need for corrections for the change in refractive index

of the air with the temperature. An arrangement can be the one shown in Figure 2.4, where the sample S is placed in between two optical flats A and B.

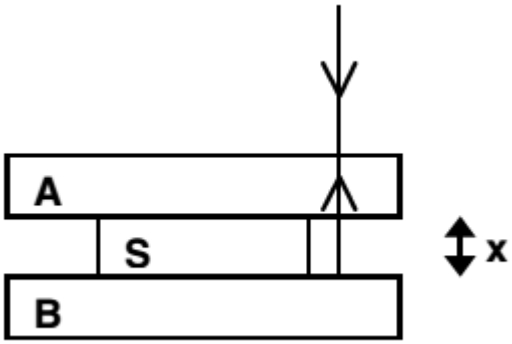

Figure 2.4 Set-up for optical interferometers with the sample S in between two optical flats A and B. **(10)**

The flats' distance change as the sample expands. A beam of monochromatic light is reflected from the bottom surface of A (transparent) and from the top surface of B. The two reflected rays interfere constructively or destructively according on the distance x. At high temperatures, there are effects that must be considered like the emitted light from the specimen and the deterioration of the optical reflective surface with the time.

  - Speckle pattern interferometry: the speckle effect is a particular interference effect that occurs when two coherent and collimated laser beams are directed onto a surface. This pattern change when the surface illuminated is deformed.

- Diffraction technique: the sample is in the form of powder, rotating crystal or polycrystalline wire and enclosed in a suitable furnace. Monochromatic x-rays are directed on the specimen and part of them is reflected with different angles. Using Bragg's relation, the distance between crystal planes can be calculated. This technique is advantageous for measuring weak materials. Noteworthy that not always the measurement of the expansion of the lattice corresponds to the bulk CTE (for example when there is more than one phase).

Mechanical push-rod dilatometer scheme

The method adopted in this work is the mechanical dilatometry through the horizontal push-rod dilatometer, whose main components are shown in Figure 2.5. The sample is kept in place

by the sample holder in the homogeneous temperature zone of the furnace. The temperature of both the sample and the furnace are monitored through thermocouples. One of the push-rod extremities is always in contact with the sample (the contact is guaranteed by a spring), while the other one is connected to the linear variable displacement transducer (LVDT).

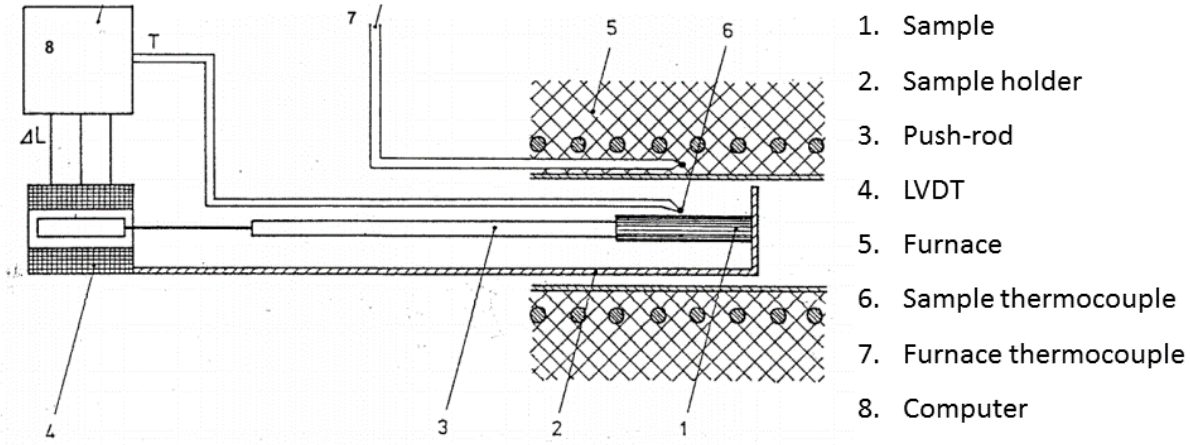

Figure 2.5 Scheme of a horizontal push-rod dilatometer.

As already mentioned, all the materials in the furnace expand, therefore the sensed length variation is the contribution of sample, sample holder and pushrod change in length. To obtain the data of the sample is necessary to calibrate the instrument, typically measuring a reference material. A calibration constant can be evaluated as:

$$A_{Ti} = \left[\left(\frac{\Delta L}{L_0}\right)_t - \left(\frac{\Delta L}{L_0}\right)_m\right]_{Ti} \qquad \textbf{2.8}$$

where the index T_i refers to a general temperature at which the length is L_i, t and m refer to the certified and the measured expansion of the reference material, respectively. The measured expansion of the sample can then be corrected with the calibration constant as follow:

$$\left[\frac{\Delta L}{L_0}\right]_{Ti} = \left[\left(\frac{\Delta L}{L_0}\right)_m + A\right]_{Ti} \qquad \textbf{2.9}$$

The linear expansion of the test specimen is then used for the calculation of its coefficient of thermal expansion:

$$[CTE]_{Ti} = \left[\frac{1}{\Delta T}\frac{\Delta L}{L_0}\right]_{Ti} \qquad \textbf{2.10}$$

2.1.5 Energy balance equation, thermal conductivity and thermal diffusivity

A physical property of a system is an extensive quantity if its value depends on the dimension of the system itself: its magnitude results from the sum of the values of the same quantity for the subsystems. Examples of extensive quantity are: volume, mass, energy and entropy. The properties which are size-independent are intensive quantities, such as: pressure, density and temperature. A system can be represented by the fluid contained in a volume $V(t)$ confined by a closed surface $S(t)$, variable with the time t. The general extensive quantity (mass dependent) can be expressed as a function of time and position $\vec{r}$, $c(\vec{r},t)$. It is possible to express the variation during the time of this property through the balance equation as follows:

$$\frac{d}{dt}\iiint_V \rho c \, dV = -\oiint_S \rho c(\vec{v} - \vec{v}_S)\vec{n} \, dS + \oiint_S \vec{J} \cdot \vec{n} \, dS + \iiint_V \rho \Phi \, dV \qquad \textbf{2.11}$$

where $\vec{v}$ is the speed of the fluid, $\vec{v}_s$ the speed of the surface, $\vec{n}$ the external versor of the surface, J the flux of the quantity c through the surface per unit area and time, and Φ represents the sources/sink of c per unit mass inside the system. It is worth to identify the global meaning of each term of this equation. The term at the left is clearly the variation with the time of the extensive quantity. This variation is given by a convective term (quantity of c inputted/removed from the system by the incoming/outgoing mass) plus a term of flux of c through the surface of the system, plus a term of generation/destruction of c inside the system.

It is possible to write the energy balance of a system substituting to c the total energy of the system, given by the sum of the internal energy and the kinetic energy:

$$u_0 = u + \frac{v^2}{2} \qquad \textbf{2.12}$$

In this case the flux of energy is the heat flux $\vec{J} = \vec{q}''$ [W/m^2], Φ is the generation/distruction of heat q''' and in the hypothesis of homogeneity, isotropy and constant volume, 2.11 becomes:

$$\frac{d}{dt}\iiint_V \rho u \, dV = -\oiint_S \overrightarrow{q''} \cdot \vec{n} \, dS + \iiint_V q''' \, dV \qquad \textbf{2.13}$$

Thanks to Green's theorem it is possible to rewrite the surface integral and express everything with integrals on the volume:

$$\frac{d}{dt}\iiint_V \rho u \, dV = -\iiint_V div q''' \, dV + \iiint_V q''' \, dV \qquad \textbf{2.14}$$

Being the volume arbitrary this leads to:

$$\rho \frac{\partial u}{\partial t} = -div\vec{q}'' + q''' \qquad \textbf{2.15}$$

The heat flux is defined by Fourier's postulate:

$$\vec{q}'' = -\lambda grad T \qquad \textbf{2.16}$$

where the proportionality constant λ [W/mK] is called thermal conductivity and it is a physical property of the substance. The meaning of this postulate is that the heat flows in the direction opposite to the temperature gradient, hence from "hotter to colder" system's regions. For a solid the variation of energy can be expressed as:

$$du = c_p dT \rightarrow \frac{\partial u}{\partial t} = c_p \frac{\partial T}{\partial t} \qquad \textbf{2.17}$$

Substituting equations 2.16 and 2.17 in equation 2.15 we obtain the so-called Fourier's equation or the thermal conductivity equation:

$$\rho c_p \frac{\partial T}{\partial t} = div(\lambda grad T) + q''' \qquad \textbf{2.18}$$

which can be written also:

$$\frac{\partial T}{\partial t} = \frac{\lambda(T)}{\rho(T) c_p(T)} \nabla^2 T + \frac{q'''}{\rho(T) c_p(T)} \qquad \textbf{2.19}$$

At this point it is possible to define the thermal diffusivity as:

$$a(T) = \frac{\lambda(T)}{\rho(T) c_p(T)} \qquad \textbf{2.20}$$

[m^2/s], which expresses how fast the heat propagates in the material. Figure 2.6 shows an overview of the values of thermal conductivity for various materials: low conductive materials are called insulating.

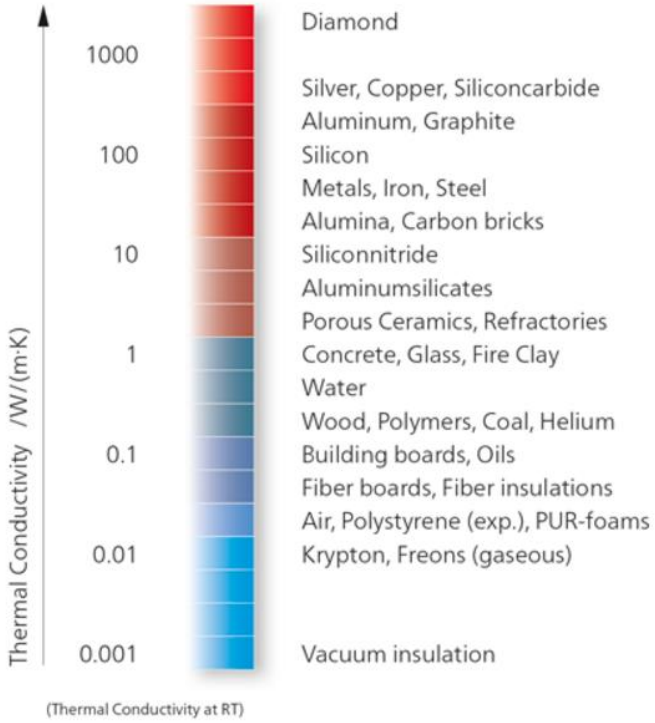

Figure 2.6 Indicative thermal conductivity values at room temperature [W/mK]. Credits NETZSCH.

2.1.6 Methods for measuring thermal conductivity

Most of the methods for measuring the thermal conductivity are direct, in the sense that they aim at the measurement of this quantity reproducing thermal situations in the material that allow the use of the Fourier's postulate. Among these methods there are:

- Direct heating: an electrical current is circulated through the sample which heats up by Joule heating. The measured voltage drop and temperature difference relate to the thermal conductivity and electrical resistivity. The application of this method is limited to electrically conductive materials.
- Comparative method: it is based on the comparison of temperature gradients. A sample of the unknown material is sandwiched between two reference samples whose extremity faces are at different temperatures. Measuring the temperature gradient of the 3 samples and knowing that the heat flux through thermal resistances in series is the same, it is

possible to calculate the unknown thermal conductivity. This method is very simple, but characterized by high uncertainties.

- Guarded heat flow meter method: it is similar to the previous method where instead of references a flux gauge is used to determine the heat flux and the sample is placed between a hot and a cold surface.
- Hot wire method: this method is suitable for thermal insulating materials. An electrical conductive wire is embedded in the sample: for example, if the sample is a cylinder the hot wire would be placed along its axis. When an electrical current flows in the wire, it heats up and can be considered a linear heat source for the sample. The temperature rise in the cylinder, which is inversely proportional to the square radius, is measured and the thermal conductivity calculated.

These methods have some disadvantages like the surface heat losses, the thermal contact resistance between the sample and its heat sinks/sources, besides large sample sizes and length of time required. Moreover, they can be used in a relative short range of temperature. The method of the laser flash is an indirect method for measuring the thermal conductivity, measuring the thermal diffusivity instead. It is characterized by lower uncertainties and the highest range of temperature (see Figure 2.7). Its functioning principle is described in the following paragraph.

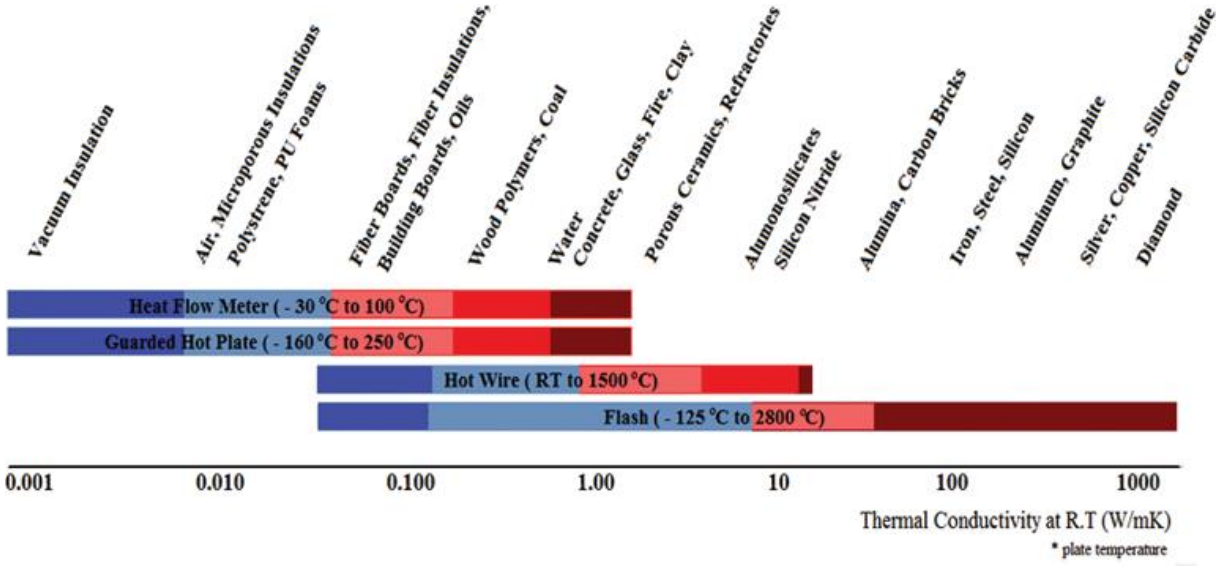

Figure 2.7 Operative ranges of different measurements method for thermal conductivity. Credits NETZSCH.

Theory and proceedings of the flash method

For all the disadvantages stated in 2.1.6 a flash method for determining thermal diffusivity had been developed and described for the first time in 1960 by Parker et al. (11). With this method some of the previous problems are solved: there is no thermal contact resistance because the heat source is a flash lamp and the heat losses are minimized by making the measurement in a very short time, during which the cooling can be neglected. The theory of the method is based on the study of Carslaw and Jaeger about the conduction of heat in solids. They solved equation 2.19, in the case of adiabatic conditions and unidimensional problem, for a solid of uniform thickness L:

$$T(x,t) = \frac{1}{L}\int_0^L T(x,0)dx + \frac{2}{L}\sum_{n=1}^{\infty} e^{\left(-\frac{n^2\pi^2 at}{L^2}\right)} \cdot \cos\left(\frac{n\pi x}{L}\right)\int_0^L T(x,0)\cos\left(\frac{n\pi x}{L}\right)dx \qquad \textbf{2.21}$$

When a pulse of energy Q is instantaneously and uniformly absorbed in a small gap g at the front surface of the solid the temperature distribution in this moment is:

$$\begin{cases} T(x,0) = \dfrac{Q}{\rho c_p g} \; for \; 0 < x < g \\ T(x,0) = 0 \; for \; g < x < L \end{cases} \qquad \textbf{2.22}$$

Therefore, the temperature history at rear face of the solid can be written from equation 2.21 with the initial conditions 2.22:

$$T(L,t) = \frac{Q}{\rho c_p g}\left[1 + 2\sum_{n=1}^{\infty}(-1)^n e^{\left(-\frac{n^2\pi^2 at}{L^2}\right)}\right] \qquad \textbf{2.23}$$

It is possible to define the following dimensionless parameters:

$$V(L,t) = \frac{T(L,t)}{T_M} \qquad \textbf{2.24}$$

$$\omega = \frac{\pi^2 at}{L^2} \qquad \textbf{2.25}$$

where T_M is the maximum temperature reached by the rear face. Equation 2.26 correlates these two terms which are plotted in Figure 2.8:

$$V = 1 + 2\sum_{n=1}^{\infty}(-1)^n e^{(-n^2\omega)} \qquad \textbf{2.26}$$

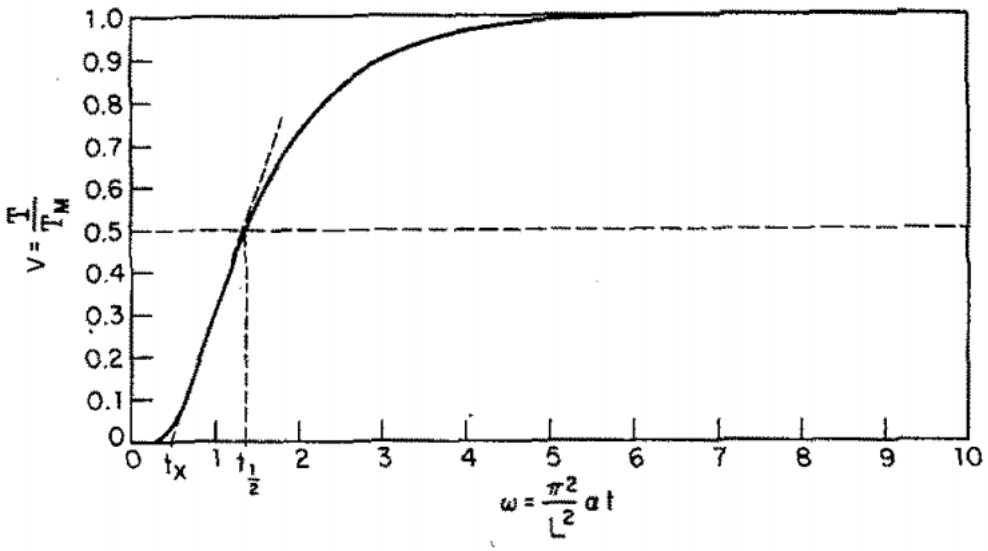

Figure 2.8 Dimensionless plot of the rear surface. **(11)**

Thanks to this relationship it is possible to determine an expression for the thermal diffusivity a. When $V = 0.5$, $\omega = 1.38$ hence:

$$a = \frac{1.38L^2}{\pi^2 t_{0.5}} = 0.1388\frac{L^2}{t_{0.5}} \qquad \textbf{2.27}$$

$t_{0.5}$ is the time necessary to the rear face to reach half of its maximum temperature. Knowing the amount of energy Q absorbed by the front face it is possible to evaluate the specific heat of the material with the relationship $c_p\rho = \frac{Q}{LT_M}$. The first set-up was composed of a commercially available flash tube able to dissipate 400 J at each flash. The sample was blackened with camphor black to maximize the energy absorption and the sample holder was also opaque to avoid irradiation of the sample. The temperature at the rear face of the sample was measured with a thermocouple and its output voltage was presented on an oscilloscope and photographed with a Polaroid land camera. The method had an important success presenting some relevant advantages: simple equipment, small specimen size, possibility to measure at high and low temperatures by pre-heating or pre-cooling the system. After the first experiment and publication, the method had been developed by modelling the system under less ideal boundary conditions. Different scientists contributed in optimizing the model, among which:

- Cowan (12): he considered the heat losses due to convection and radiation at both front and rear surfaces for a finite square impulse. He expressed dimensionless solutions for different heat losses, concluding that the measurement of thermal diffusivity by pulse method should give reliable results also when the heat losses cause a reduction of the maximum temperature of the rear face of 80-90% the no-losses value.
- Cape and Lehman (13): they brought important improvements to the initial theory, considering both heat losses due to radiation and finite pulse-time effects. The former effect is considered by solving the thermal energy balance (equation 2.19) for a cylinder sample of radius r_0, with boundary conditions deriving from the Stefan-Boltzmann radiation law for grey bodies:

$$q = \sigma\epsilon(T^4 - T_0^4) \qquad \textbf{2.28}$$

Where $\sigma = 5.67\ 10^{-8}\frac{W}{m^2K^4}$ is the Stefan-Boltzmann constant, ϵ is the emissivity (between 0 and 1 for grey bodies), T the temperature of the sample and T_0 the ambient temperature. They expressed the temperature rise at the rear face (normalized to the maximum temperature) in function of the time (normalized to the characteristic time $t_c = \left(\frac{L}{\pi}\right)^2\frac{1}{a}$, that represents roughly the time needed to the heat pulse to propagate the thickness of the sample) for different values of a dimensionless parameter dependent to the radiation heat losses, Y.

$$Y = Y_x + \left(\frac{L}{r_0}\right)^2 Y_r \qquad \textbf{2.29}$$

$$Y_r = 4\sigma\varepsilon_r T_0^3\lambda^{-1}r_0 \qquad \textbf{2.30}$$

$$Y_x = 4\sigma\varepsilon_x T_0^3\lambda^{-1}L \qquad \textbf{2.31}$$

The solution is shown in Figure 2.9. We can distinguish two situations:

1. Low temperatures, Y<<1 (negligible radiation heat losses): in this case the solution is equal to equation 2.27 derived by Parker et al., and the temperature rises from T_0 to the constant final temperature $T_0 + \delta\_max$ (see curve 1). For $Y = 0$, $\frac{t}{t_c} = 1.388$.

2. High temperatures, $Y <\cong 1$ (see curves 2, 3 and 4): $\frac{t}{t_c} < 1.388$ and the use of equation 2.27 would lead in error. An iterative procedure must be applied to evaluate a: an initial value can be obtained with 2.27, and Y can be estimated with reasonable values of emissivities. Using the corresponding curve one can obtain a new value for a and so on.

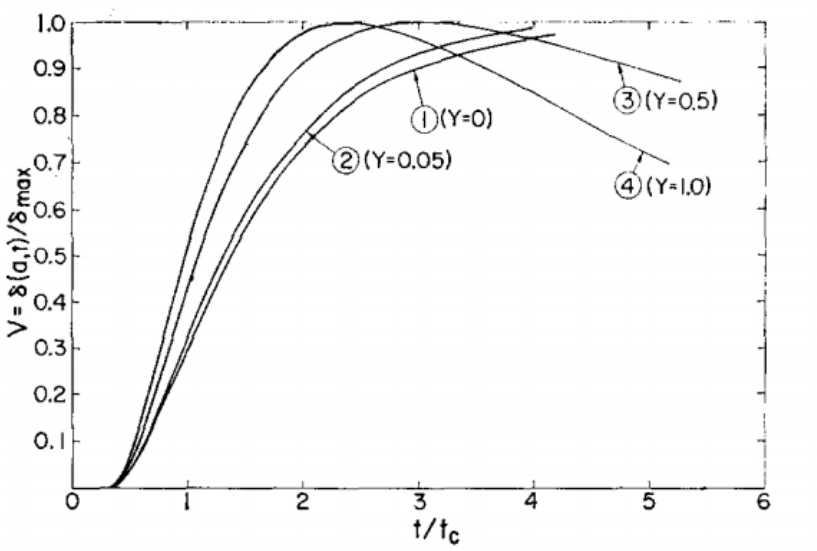

Figure 2.9 Normalized temperature rise of the rear face of the sample in function of time, for different heat losses.

For $Y < 5\ 10^{-2}$ the approximation of Parker et al., is accurate to about 5%.

The finite pulse time effect has been investigated for those cases when τ, the pulse duration, is comparable to the characteristic diffusion time t_c. In this situation, the rise in temperature is expected to be retarded. In Figure 2.10 it is possible to observe that as τ becomes closer to t_c the coefficient of equation 2.27 increases, hence the correction is in the opposite sense to the one applied to compensate for heat losses.

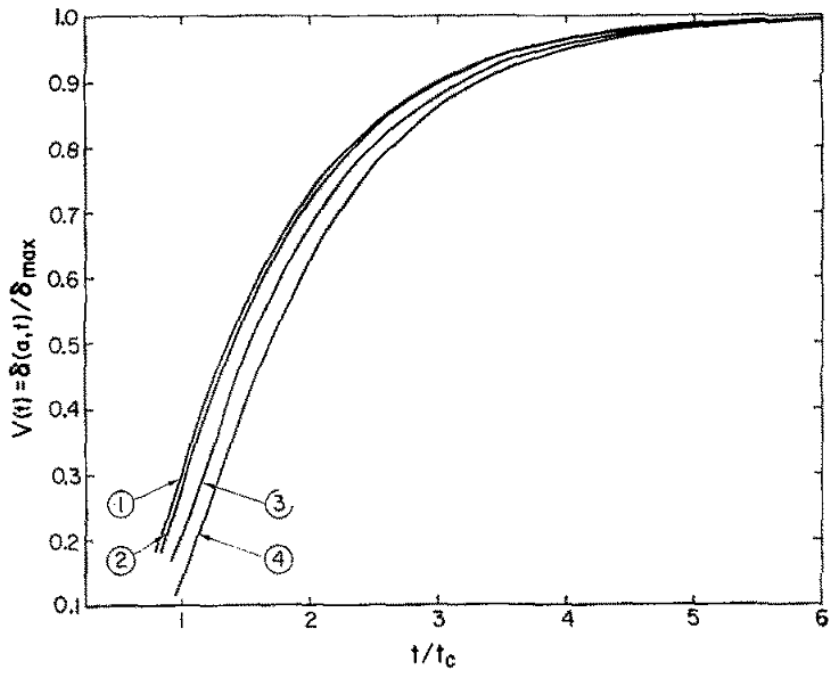

Figure 2.10 Normalized temperature rise at the back surface. Curve 1 is for $\boldsymbol{\tau = 0.01\ t_c}$, curve 2 for $\boldsymbol{\tau = 0.1\ t_c}$, curve 3 for $\boldsymbol{\tau = 0.51 t_c}$ and curve 4 for $\boldsymbol{\tau = 0.91 t_c}$.

- Clark and Taylor (14): starting from the theoretical solution found by Cape and Lehman, they developed the so-called ratio method, aimed to avoid the iterative procedure. With the previous results, they plotted the ratio between t/t_c evaluated for 2 different percent rise (eliminating t_c) which decrease with increasing heat loss and validated the method testing a reference POCO-Graphite.

Laser flash apparatus scheme

The instrument of interest for this thesis and based on the flash method technique is the laser flash apparatus, see Figure 2.11. The sample is placed on a tube-shaped sample holder embedded in a furnace. The laser pulse is sent to the bottom (front) face of the sample by an optical fiber and the temperature increase on the upper (rear) face is sensed by an infrared detector. The furnace allows thermalize the test specimen at the desired temperature and to measure the diffusivity corresponding at different temperatures. Both the temperature of the sample surroundings and of the furnace are measured with thermocouples.

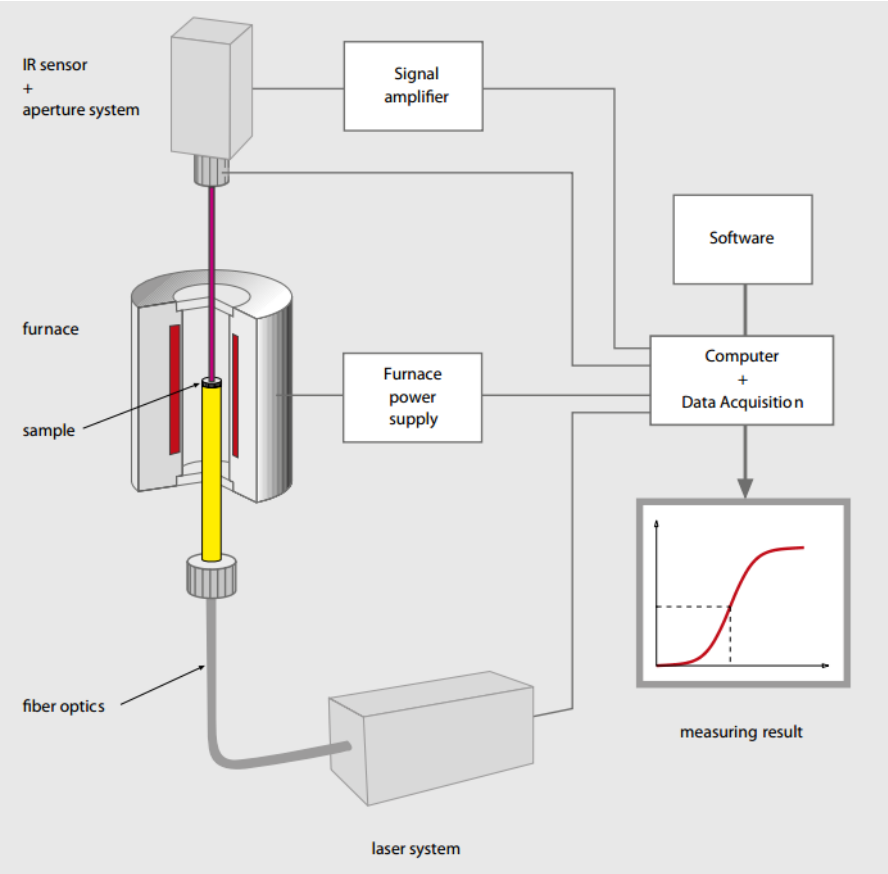

Figure 2.11 Scheme of a laser flash apparatus.

2.2 Mechanical properties and their measurement

2.2.1 Mechanical properties

When considering an isotropic homogeneous material, its elastic tensor is fully described with two elastic properties, typically the Elastic Modulus E [GPa], the Poisson ratio ν [-] or the Shear modulus [GPa]. The materials of interest of this work are anisotropic, meaning that they have direction-dependent properties which are different in the direction parallel to the hot-pressing direction and perpendicular to it. For this kind of materials, five properties are needed to define the elastic tensor. The Young's modulus can be expressed in two different ways (see Figure 2.12): we can imagine to cut the composite perpendicularly to the load application direction in which case, to conserve the continuity of the matter, the deformation of the phases must be the same for matrix and reinforcement (Voight assumption); if we rather cut the material parallel to the load application the stresses on the phases must coincide to balance the force.

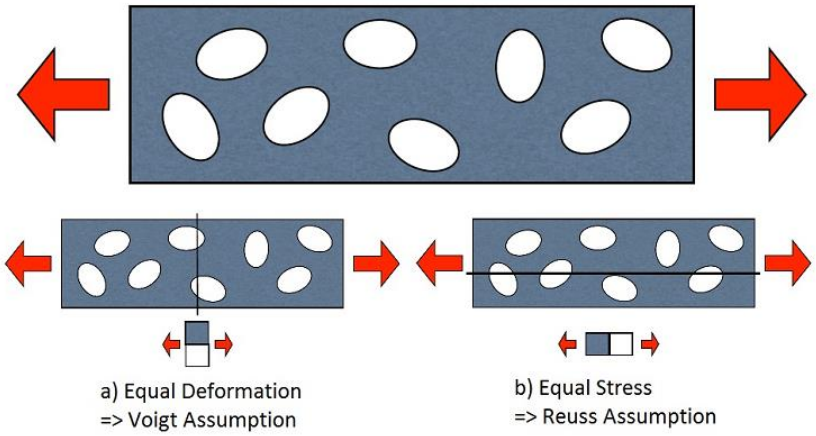

Figure 2.12 Scheme of Voigt and Reuss assumption for a reinforced composite.

$$E_V = f_{vm}E_m + f_{vr}E_r \quad \textbf{2.32}$$

$$E_R = \left(\frac{f_{vm}}{E_m} + \frac{f_{vr}}{E_r}\right)^{-1} \quad \textbf{2.33}$$

Where the index v indicates the volumetric fraction, m the matrix and r the reinforcement. These two assumptions represent the upper and lower limit of the isotropic composite respectively.

The materials tested are graphitic CMC reinforced with fibers or carbides, which have typically a brittle behavior and limited plasticity. Non-ductile materials lack of any method of flowing or yielding to accommodate the stresses applied, they basically don't allow the movement of dislocations. In this kind of material any flaw or crack (critical defect) can act as a stress concentrator, giving rise to a tri-axial stress state of tension. As soon as the intensification of the stress overcomes the material's resistance, the highest stresses flaw tip propagates causing the failure of the piece. Hence, in these kind of materials, the strength depends on the flaws, usually smaller than 100 µm, which are difficult to eliminate and to see. This leads to a huge scatter of the size of the critical defect and consequently to a huge scatter on the values representative of the strength. As consequences: the strength cannot be determined until the test piece breaks, it requires a large number of tests to have reliability on the average, there will be always test pieces significantly weaker and stronger than the average.

2.2.2 Methods for measuring the mechanical properties

The most known method to determine the behavior of a material in its elastic range is the tensile test, which consists in applying an increasing force along the axis of a beam-shaped specimen. Both the load and the strain of the sample are recorded and depicted in the stress-strain curve of the material: from these curves (see Figure 2.13), it is possible to extract information about the material, such as ductile/fragile nature, Young's modulus (slope of the linear section of the stress-strain curve), strain to rupture, stress to rupture, resilience etc.

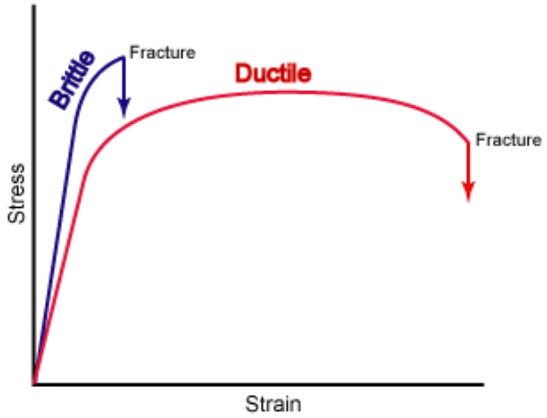

Figure 2.13 Stress-strain curves representing brittle and ductile behaviors.

Despite its advantages, this method is not suitable to characterize the test specimens available during this work, too small (due to manufacturing reasons) and not keen to be clamped in the tensile tool jaws. Moreover, it is difficult to identify a purely linear region where to evaluate the slope. Therefore, two different techniques are applied for the characterization: flexural test and impact excitation technique (IET). When possible, also compression tests are performed to have a more complete overview of the material behavior.

Compression test

One of the main advantages of this technique is the test specimen's geometry: the sample is a cylinder with flat extremities which do not need to interface with any fixture. In fact, the second big advantage of the technique is the simplicity of the compression tooling: the specimen is placed between two rigid plates that approaching each other give rise to a state of tension of simple compression (provided there is no friction between the sample's basis and the plates). The stress can be evaluated as follows:

$$\sigma_c = \frac{F}{A} \qquad \textbf{2.34}$$

Where F is the compressive force and A the cross sectional area of the specimen. The most important quantities obtained from these tests are the stress and strain to rupture in compression.

Impact Excitation Technique

This dynamic method is a non-destructive technique widely used to characterize brittle materials, such as ceramics, as it requires a small specimen of simple geometry and allows to obtain Young's modulus, Poisson ratio and Shear modulus with a single measurement and set-up. On the other hand, it is sensitive to flaw in the geometry (machining damages, surface finish and poor geometric tolerances). The sample is a beam test-piece with uniform cross-section and the method relies on the fact that the vibration modes of the bodies are determined by their mass, geometry and elastic properties. The modes are determined by measuring the vibration of the test specimen when stricken by a hammer: the sample would "ring" and the sound spectrum recorded to obtain the resonance frequencies (the method is also known as "Natural frequencies method"). At the basis of the method there are the modes of vibration of the prismatic beam, whose principal ones are:

- Flexural (out-of-plane and in-plane): depend on the Young's modulus of the test-piece in the longitudinal direction (roughly independent of the material anisotropy for a slender beam). For a bar of isotropic and homogeneous material of mass m, length l, width b and thickness t, the Young's modulus can be formulated as:

$$E = 0.9465 \left(\frac{m f_f^2}{b}\right)\left(\frac{L^3}{t^3}\right) T \qquad \textbf{2.35}$$

Where the parameter T is:

$$T = 1 + 6.585(1 + 0.0752\nu + 0.8109\nu^2)\left(\frac{t}{L}\right)^2 - 0.868\left(\frac{t}{L}\right)^4 - \left[\frac{8.34\left(1 + 0.2023\nu + 2.173\nu^2\left(\frac{t}{L}\right)^4\right)}{1 + 6.338(1 + 0.1408\nu + 1.536\nu^2)\left(\frac{t}{L}\right)^2}\right] \qquad \textbf{2.36}$$

If $L/t > 20$ the expression can be simplified as $T = 1 + 6.858(t/L)\text{^}2$, eliminating the need to know the Poisson's ratio a priori. In a free-free prismatic beam the out-of-plane

modes of vibration present nodes (minimum vibration) and antinodes (maximum vibration) along the length as depicted in Figure 2.14.

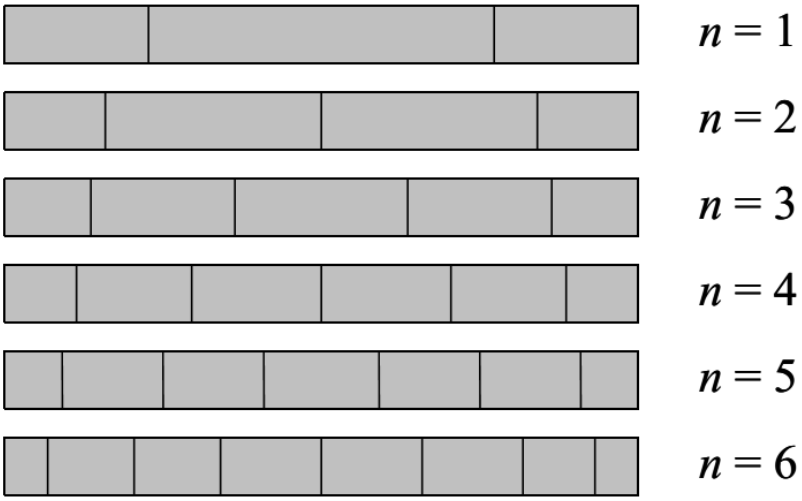

Figure 2.14 Out-of-plane vibration modes of a free-free beam: nodal lines.

The first vibration mode has nodes at 0.223 times the length from the extremities and antinodes in the center and at the extremities. This resonant mode can be excited in a constrained beam if this is supported at the nodes and excited (especially at the center and the extremities which are the antinodes, see Figure 2.15.

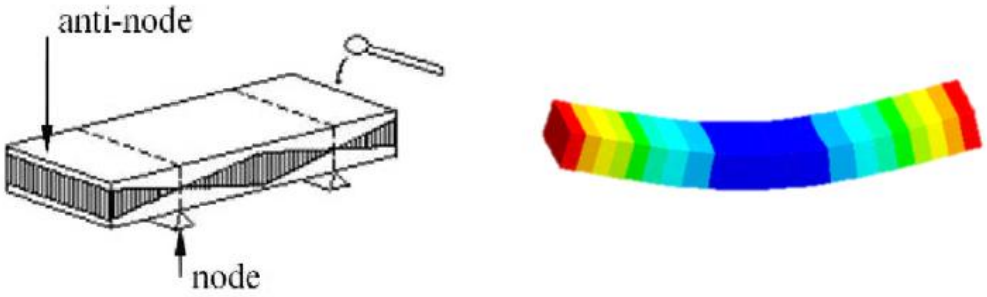

Figure 2.15 Nodes and antinodes of the first out-of-plane flexural mode.

- Torsional: for isotropic materials, it depends on the shear modulus. For anisotropic materials, it is controlled by a mix of shear stiffness in the principal planes. The shear modulus is related to the fundamental torsional frequency through the relation:

$$G = \frac{4Lmf_t^2}{bt}\left[\frac{B}{1+A}\right] \qquad \textbf{2.37}$$

Where the shape term B is:

$$B = \frac{\frac{b}{t} + \frac{t}{b}}{4\left(\frac{t}{b}\right) - 2.52\left(\frac{t}{b}\right)^2 + 0.21\left(\frac{t}{b}\right)^6} \quad \textbf{2.38}$$

And the empirical correction factor A is:

$$A = \frac{0.5062 - 0.8776\left(\frac{b}{t}\right) + 0.3504\left(\frac{b}{t}\right)^2 - 0.0078\left(\frac{b}{t}\right)^3}{12.03\left(\frac{b}{t}\right) + 9.892\left(\frac{b}{t}\right)^2} \quad \textbf{2.39}$$

From Figure 2.16 and Figure 2.17 it is possible to see that to excite the first torsional mode the beam must be supported at the center (node).

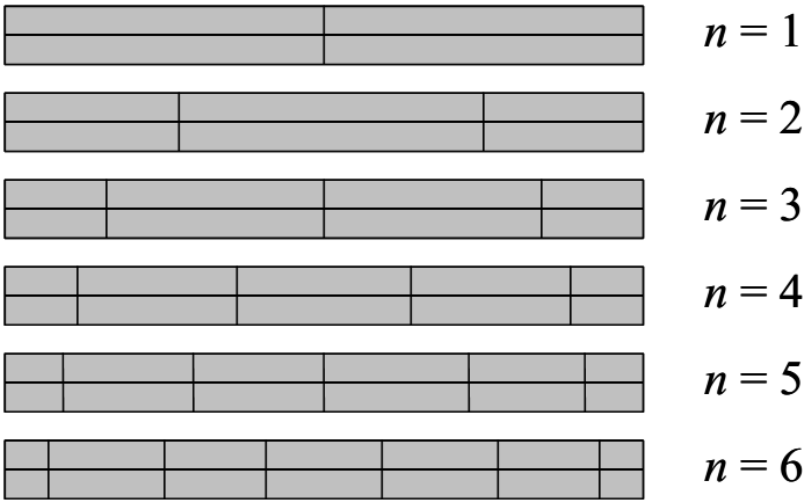

Figure 2.16 Torsional mode of a free-free prismatic beam: nodal lines.

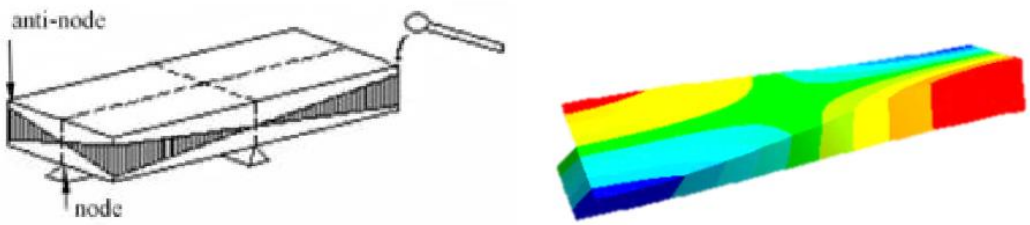

Figure 2.17 Nodes and antinodes of the first torsional mode.

- Longitudinal: these modes of vibration, depend on the Young's modulus and the Poisson's ratio in the longitudinal direction. They are associated to higher frequencies (lower displacements) which are more difficult to be sensed by the available instrumentation.

Looking at Figure 2.14 and Figure 2.16, it is clear how the nodal lines of the first flexural and second torsional mode are similar: this suggests to use the same constraint configuration employed to determine the first flexural mode also for determining the second torsional (which ratio with the fundamental is 2:1). With one single set-up it is possible to determine E from the fundamental flexural mode by striking the sample at the center, and G from the second torsional mode by hitting it at the extremities (at a location off of the longitudinal nodal line). The Poisson's ratio can then be evaluated as:

$$\nu = \frac{E}{2G} - 1$$

The theory described in this paragraph is valid for isotropic materials, while those tested are anisotropic: there exist more complex methods, which are actually used, to extract the elastic properties of anisotropic materials from the sound spectrum recorded.

Flexural test

The flexural test consists in bending the bar-shaped test specimen, applying a force perpendicular to its axis. While the force increases, the stresses inside the beam increase in an elastic fashion (within the elastic range): those in the convex side of curvature are tensile stresses while those in the concave side are compressive stresses, both directed along the axis of the specimen. Compressive and tensile stresses have different effects on the behavior of brittle materials: while the former tend to close the voids and cracks, the latter promote the propagation of cracks. Therefore, when performing these tests the convex side of the specimen in the vicinity of the surface (where the stress intensity is higher) is normally where the fracture starts. The flexural test presents some advantages in comparison to the tensile test, such as: no problems of gripping, easy alignment, cheap set-up, rapidity. Among the disadvantages there is the tendency of superficial flaws to dominate the behavior.

There are two main set-ups available to perform flexural tests: the three-point and four-point bending see Figure 2.18.

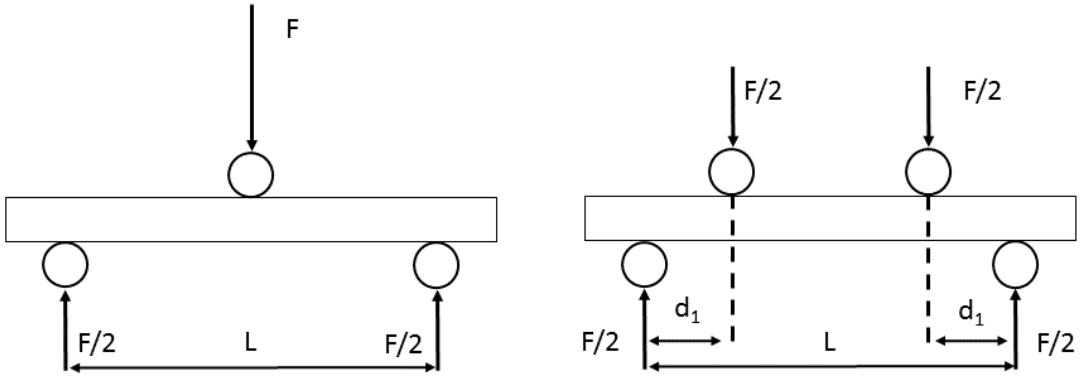

Figure 2.18 Support and load application in the 3- and 4-point bending.

The stress at fracture can be evaluated for a thin beam with rectangular section as follows:

$$\sigma_{f3} = \frac{3F_m l}{2bh^2} \quad \textbf{2.40}$$

$$\sigma_{f4} = \frac{3F_m d_1}{bh^2} \quad \textbf{2.41}$$

Where F_m is the maximum force applied, l the support span, $d_1$the distance between the inner loading roller and the outer support, b the width of the test piece and h its thickness. The stresses evaluated are called nominal flexural stresses because they refer to the outer fiber and may be greater than the value which caused the fracture origin at the critical defect. Three-point bending it is easier to perform while the four-point arrangement is normally preferred because a larger volume of material is at the same level of nominal stress, resulting in a method which is more searching for big defects. A consequence is that the ultimate stresses evaluated with the three-point bending are generally higher. The Standards usually define the more appropriate method or they allow both.

As described in the NPL guide No.98 (15), the flexural test can be performed as an alternative method to the tensile test for the determination of the Young's modulus. Using a thin beam tests specimen, the calculation (Timoshenko theory) can be done measuring the deformation of the outer fiber by measuring either the displacement or the net out-of-plane displacement of two points of the sample surface or applying strain gages on the face of the specimen at the span center. In the latter case, the one adopted during the tests, the expression of the Young's modulus becomes (4-point bending configuration):

$$E = \frac{3(F_2 - F_1)d_1}{bh^2\varepsilon} \quad \textbf{2.42}$$

Where F_1 and F_2 are the upper and lower level of forces selected from the recordings and ε the corresponding measured strain.

3 Experimental work: materials and methods

3.1 Materials

In the framework of the R&D project on the collimators' jaws materials, two different graphitic composites are selected for the mechanical and thermo-physical characterization: CFC FS140® and MG-6403-Fc. Both are candidates for the production of new primary and secondary collimators.

3.1.1 CFC FS140®

This carbon fiber-carbon composite is manufactured by the Japanese Tatsuno, as the CFC AC150® described in 1.5.2. Tatsuno's CFC is the absorber material used on the low-density collimators (primary and secondary) since 2004, due to its decent electrical conductivity and high strength. During the development of the new TCPPs (primary collimators), this same CFC was expected to be employed but since the first order the Asiatic manufacturer had changed the provider of raw CF, from the AK-150 Across Co. to the FS140 CFC Design Co. Hence, a new and complete thermo-physical and mechanical characterization is required. Many information about this material are missing, since they have not been provided by the manufacturer, both regarding the composition and the details of the production process. In general, the production

process of CFCs follows the one of graphite, explained in 1.2 , with the addition of carbon fibers. The graphitization temperature is 2500 ℃, 300 ℃ less than the CFC AC150®.

The material was ordered in the shape of a plate of dimension $1230\ mm\ x\ 500\ mm\ x\ 27\ mm$. The plate was then machined in the CERN's workshop by conventional milling and turning to obtain the samples listed in Table 3.1 and shown in Figure 3.1:

Test	Dimension [mm]	Direction	Nr of samples
Dilatometry	Φ 6 x 25	**yz**	6
		x	6
Calorimetry	Φ 5 x 0.75	**-**	6
LFA	Φ 12.5 x 3	**yz**	6
		x	6
Flexural test (IET)	4 x 10 x 25	**yz**	6
		x	6
Compression test	Φ 7.5 x 15	**yz**	6
		x	6
Electrical conductivity	4 x 4 x 30	**yz**	6
		x	6

Table 3.1 List of CFC FS140® samples' dimensions and cutting directions.

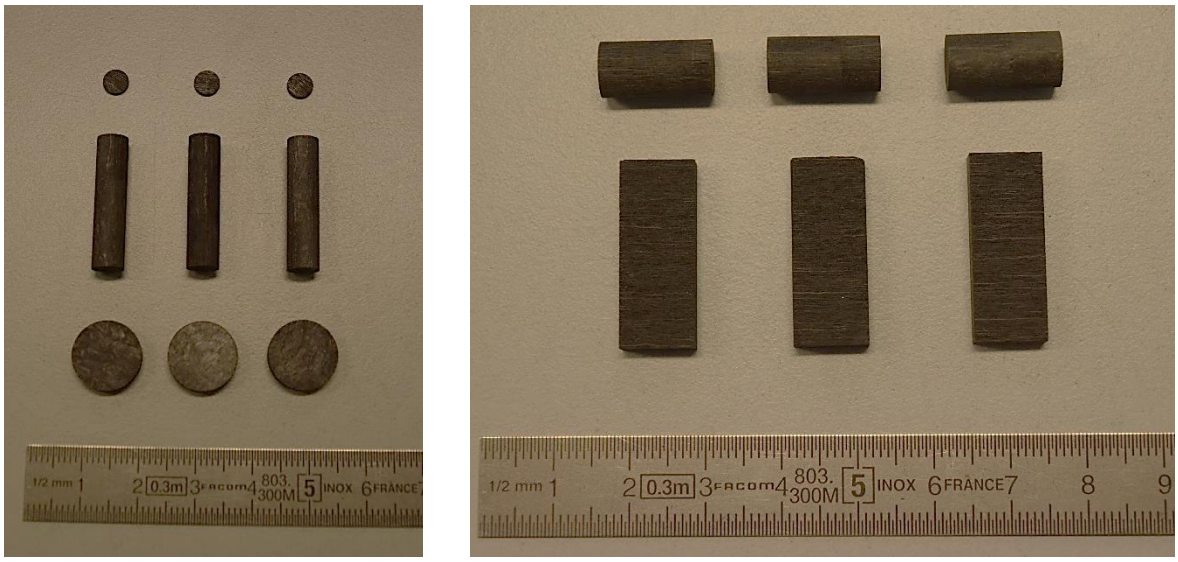

Figure 3.1 Picture of CFC FS140® test specimens for the thermo-physical (left) and mechanical (right) characterization.

A class I hydrostatic balance is used to determine the density of the material, measuring the LFA samples before the thermo-physical characterization. The averages of three measurements over each of four samples are stated in Table 3.2:

Sample	Density [g/cm^3]
S1	1.851
S2	1.882
S3	1.875
S4	1.894

Table 3.2 Density (average of three consecutive measurements) of four CFC FS140® samples. The ambient temperature was 23 °C and the density of the medium (ethanol) 0.787 g/cm^3.

3.1.2 MG-6403-Fc

This grade of molybdenum carbide reinforced graphite is one of the multiple MoGR grades produced within the collaboration with the Italian SME BrevettiBizz. Thanks to the cooperation, many more details are available in terms of composition and production process. Table 3.3 contains details about the composition, while the parameters of the production process, which is described in 1.6.2, are depicted in Table 3.4.

Vol. % Mo	4.5
Vol. % graphite	95.3
Vol. % Ti	0.2

Table 3.3 Composition of MG-6403-Fc.

Process parameter	S	PS
Estimated temperature [°C]	2600	2600
Time [s]	1200	3000
Pressure on the plate [MPa]	35	0
Atmosphere	10^{-3} mbar - air	

Table 3.4 Production process parameters. S=sintering, PS= post sintering.

The dimensions of the plate after sintering and post-sintering treatment are $150\ mm\ x\ 100\ mm\ x\ 26.5\ mm$. The samples are cut by traditional milling and turning at the BrevettiBizz facility, in the number and dimensions stated in Table 3.5:

Test	Dimension [mm]	Direction	Nr of samples
Dilatometry	Φ 6 x 10	**yz**	3
		x	3
Calorimetry	Φ 5 x 0.75	-	3
LFA	Φ 10 x 2	**yz**	2
		x	4
Flexural test	5 x 10 x 55	**yz**	5
(IET, Electrical conductivity)	5 x 10 x 25	**x**	4

Table 3.5 List of MG-6403-Fc samples' dimensions and cutting directions.

The density of the material has been measured with a hydrostatic balance, and the averages of three measurements done over two samples are in Table 3.6:

Sample	Density [g/cm^3]
S1	2.583
S2	2.589

Table 3.6 Density (average of three consecutive measurements) of two MG-6403-Fc samples. The room temperature was 24 °C and the density of the medium (ethanol) 0.791 g/cm^3.

Figure 3.2 shows a SEM image of a MG-6403-Fc sample cut along the x direction where it is possible to see the basal planes of the graphitic matrix and the molybdenum carbides here dispersed.

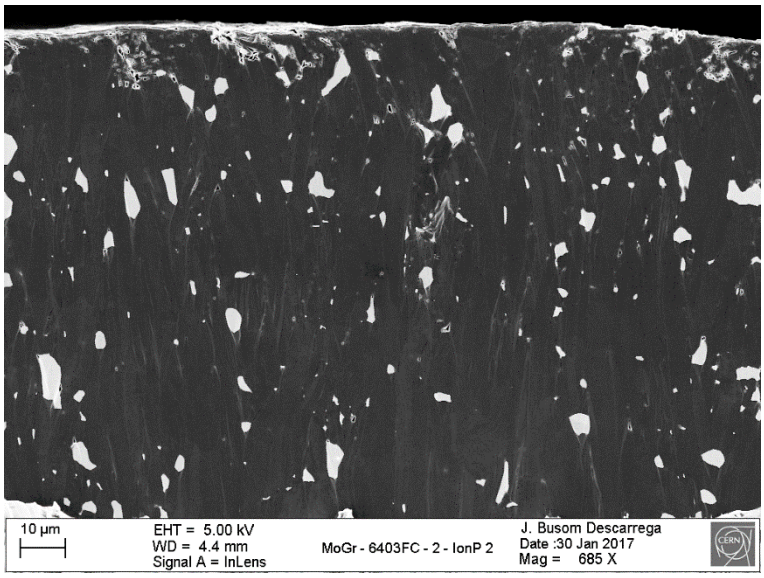

Figure 3.2 SEM image of MG-6403-Fc sample cut along the x direction.

3.2 Instruments for the thermo-physical analysis

In this section, the three instruments used for the thermo-physical characterization are described. The claimed uncertainties of measurement are evaluated as explained in Appendix.

3.2.1 Push-rod dilatometer: DIL 402 E

The method used to measure the coefficient of thermal expansion is the mechanical dilatometry through the horizontal push-rod dilatometer DIL 402 E made by NETZSCH, whose schematic functioning is described in 2.1.4. The instrument has been produced with state of the art technology and the standard test method ASTM E228, described below, is applicable.

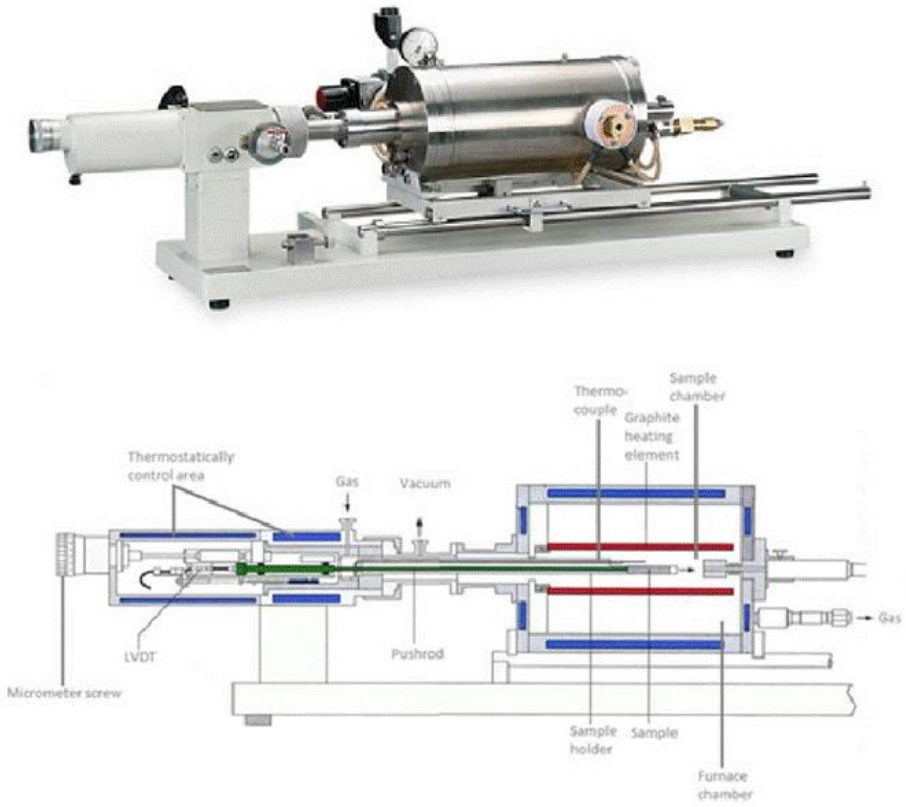

Figure 3.3 DIL 402 E by NETZSCH and its scheme.

The electrical furnace is made of graphite and can reach 2000 ℃, it is suitable to operate both under vacuum and in inert atmosphere. It is water cooled and its temperature is controlled by a W3%Re-W25%Re thermocouple. A safety system always monitors both the flow of cooling water and gas. Two set-ups of sample holder and push-rod are available: POCO-Graphite and Al_2O_3 (for use in oxidizing atmosphere up to 1680 ℃). The sample, ideally in the shape of a cylinder, is positioned inside the sample holder (see Figure 3.4) and the push-rod is approached operating a micrometer screw. The temperature in its surroundings is measured with the same type of thermocouple employed for the furnace. The LVDT is placed far from the measuring zone and is thermalized by a distilled-water closed circuit.

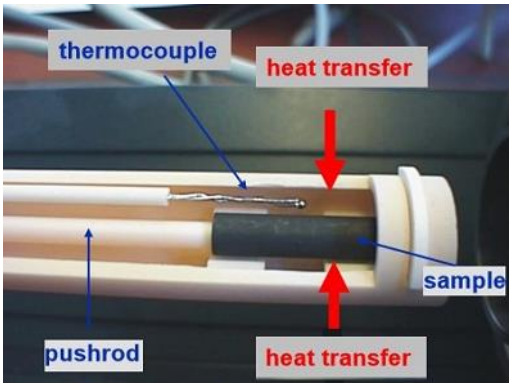

Figure 3.4 Sample of POCO-Graphite housed in the sample holder with the Alumina set-up.

Some key technical data of the instrument are collected in Table 3.7:

Technical data	
Temperature range	RT-2000 °C Graphite set-up RT-1680 °C Alumina set-up
Heating rate	0.01-50 K/min
Atmosphere	Inert (Ar, He > 2000 °C) Oxidizing (Alumina set-up) Reducing Static and dynamic
Vacuum	10^{-2} Pa
Measuring range	500-5000 µm
Load at the sample	15-45 10^{-2} N
ΔL resolution	0.125 nm/digit, 1.25 nm/digit
Other functionalities	Melting temperatures Glass transitions and softening points meas. Sintering temperature analysis Sample containers for paste, liquid and molten metals
Uncertainty (thermal expansion)	± 3.8%
Uncertainty (CTE)	± 5.3%

Table 3.7 Key technical data of DIL 402 E.

The test parameters are listed in Table 3.8:

Instrument set-up		Graphite
Atmosphere		He 100 ml/min
Temperature program	Isothermal step	10 min at 25 °C
	Heating phase	5 K/min up to 1950 °C
	Cooling phase	5 K/min down to 25 °C
	Isothermal step	10 min at 25 °C
Reference material	CFC FS140®	POCO-graphite 24.998 mm
	MG-6403-Fc	POCO-graphite 15.001 mm

Table 3.8 Dilatometry test set-up.

ASTM E228: Standard test method for linear thermal expansion of solid materials with a push-rod dilatometer (16)

The test method aims to reduce the variability of the test conditions in order to realize measurements which are comparable and to minimize the arbitrariness of the test. The Standard describes the calibration method, apparatus, procedure, preparation of the tests specimen and calculation of the quantities of interest. Some of the most important recommendation and good practices are:

- Apparatus:
    - the sample holder and push-rod should come from the same material, uncontrolled substitutions lead to increase of uncertainties. A general verification can be done measuring a specimen cut from the same material: its CTE should be smaller than $\pm 0.3\ 10^{-6}\ K^{-1}$.
    - The temperature control of the furnace at a constant rate should be monotonous within ±2°C (or 5% of the instrument's maximum temperature), while the control of equilibrium shall be within ±1°C (or ±0.05% of the instrument maximum temperature).
    - The displacement transducer must cover the expected displacement within its linear range. Its resolution must be not less than 0.1% of its linear range and a linearity of at least ±0.1% of their linear range.
    - The specimen temperature must be sensed with calibrated sensor capable to provide indication of this temperature ±0.5°C (or ±0.1% of its overall temperature range). The position of the sample thermocouple is important: a good practice is to place the head of the thermocouple equidistant from the specimen and the sample holder, and shielded from the direct view of the heating element.
- Test specimen: the specimen should be between 25 and 60 mm long and between 5 and 10 mm in diameter (or equivalent if not cylindrical). Its cross sections must be robust to prevent buckling or creep and its ends must be smooth, parallel and it should form point contact with the dilatometer. Determine the initial and final length of the sample with a measuring tool capable of reading to at least 25 µm.
- Procedure: measure the initial length of the specimen and place it in the sample holder making sure it is stable. The measurement of CTE can be done either heating (cooling) the specimen to incremental constant temperatures hold until the transducer reads variations less than ±2µm, or heating (cooling) at a constant rate equal or lower than 5°C/min. In the former case the mean temperature of the specimen may differ from the measured temperature, but the measured expansion is accurate if the calibration is done correctly.

3.2.2 Laser flash apparatus: LFA 427

The instrument used to measure the thermal diffusivity is the Laser flash apparatus LFA 427 by NETZSCH, see Figure 3.5. The instrument has been produced with state of the art technology and the standard test method ASTM E2585, is applicable.

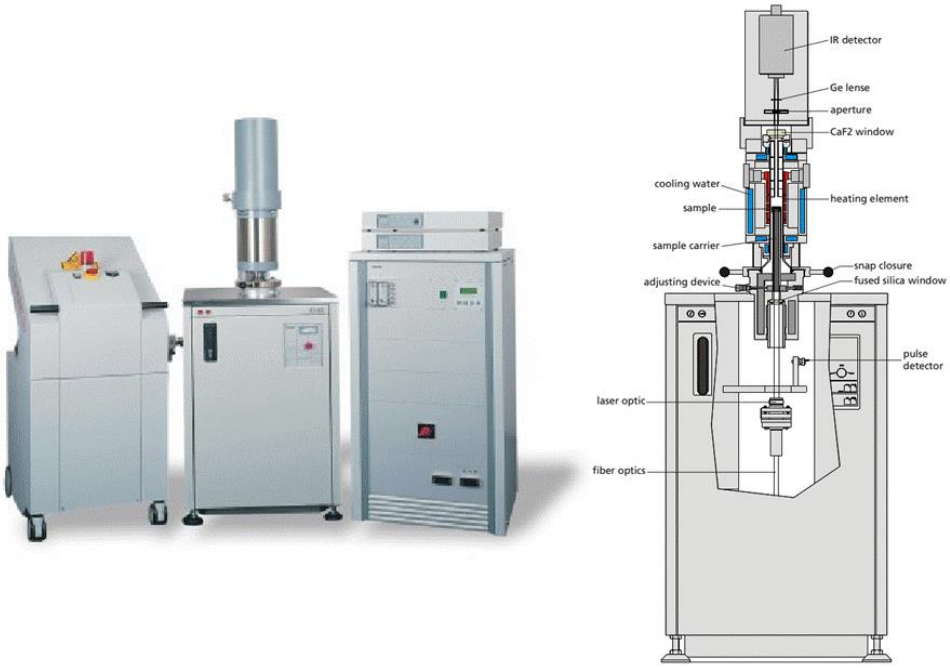

Figure 3.5 LFA 427 by NETZSCH with control cabinet, data acquisition system and laser source and scheme of the measuring part.

The electric furnace is capable to reach 2000 °C and it is made of a heating element ad insulation made of graphite and mounted in a water-cooled housing. The top and the bottom of the furnace are sealed with a calcium fluoride and fused silica lenses respectively. The measurements can be done under vacuum, in inert atmosphere and oxidizing atmosphere (alumina set-up). The vertical set-up allows an easy handling of the sample which is housed in a tube-shaped sample holder, where it lies on three tiny supports to minimize the conductive heat losses. A cap is placed on the sample to avoid direct illuminate the detector and reduce signal disturbance, see Figure 3.6.

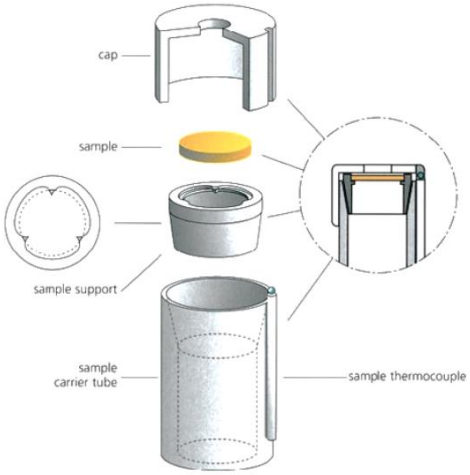

Figure 3.6 Sample holder and cap.

The optical fiber extremity is embedded in the bottom part of the device and targets the front face of the sample through the fused silica window. The IR detector (indium antimonide) is mounted directly on the top of the furnace, it has a visual contact with the upper face of the test specimen and it is nitrogen liquid cooled.

Some key technical data are listed in Table 3.9.

Technical data	
Temperature range	RT-2000 °C
Diffusivity range	0.01-1000 mm^2/s
Standard sample dimensions	0.1-6 mm thick 6-12.7 mm diameter
Atmosphere	vacuum: 10^{-5} bar static /dynamic inert gas (Ar, He) oxidizing atmosphere
Laser	Nd: YAG Power max: 25 J/pulse Pulse width: 0.3-1.2 ms Wave length: 1064 nm
IR detector	InSb
Other functionalities	Thermal contact resistance Lamellar samples In-plane measurements Powder and liquid samples Specific heat evaluation Measurement with mechanical pressure Square samples
Uncertainty (thermal diffusivity)	± 5.6%

Table 3.9 Key technical data of LFA 427 by NETZSCH.

The test parameters are listed in Table 3.10:

Instrument set-up	Graphite
Atmosphere	Ar 100 ml/min
Laser voltage	550 V
Pulse duration	0.6 ms
Temperature program	20-1950 °C divided in 20 isothermal steps 5 shots at every isothermal step
Model for calculation	Cape-Lehman + pulse correction

Table 3.10 Laser flash test set-up.

ASTM E2585: Standard practice for Thermal diffusivity by the Flash Method (17)

This practice contains some details regarding the measurement of the thermal diffusivity of primarily homogeneous isotropic and solid materials within 10^{-7} - 10^{-3} m^2/s, ranging from 75 to 2800 K. The flash method is an absolute technique, reference materials can be used to verify its performances though. This method has been shown to produce useful data also for anisotropic materials, provided that the directional thermal diffusivities are mutually orthogonal and the heat flow produced is unidirectional. A number of international round robin testing programs have shown that a measurement precision of 5% can be attained for thermal diffusivity. The standard describes the apparatus, procedure, preparation of the tests specimen and calculation of the quantities of interest. Some of the most important recommendation and good practices are:

- Apparatus:
    - The duration of the flash should be less than 2% of the half time rise to keep error due to finite pulse width less than 0.5%. The pulse intensity should be spatially uniform. Since most of the lasers have higher intensity in the center the spot should be larger than the specimen diameter. The uniformity is improved up to 95% using an optical fiber.
    - The furnace should keep the temperature constant within 4% of the maximum temperature rise over a time period equal to five times the maximum time rise.
    - The detector shall be capable to detect 0.05 K increase of temperature. The response time must be smaller than 2% the half time rise. The view windows must not absorb the radiation in the wavelength region of the detector, therefore they have to be cleaned and kept free from deposits.

- The data acquisition system must have an adequate speed to have the time resolution in determining half of the maximum temperature rise on the thermogram at least 1%.

- Test specimen: the diameter usually varies between 10 to 12.7 mm. Smaller samples provide lower energy at the rear face. The optimum thickness depends on the estimated value of thermal diffusivity and should lead to maximum temperature time rises between 10 to 1000 ms. At high temperatures, smaller samples minimize the heat loss correction. Typical thicknesses are 1-6 mm. A thickness cannot be optimal for both measurements at low and high temperatures. The faces of the specimen must be flat within 0.5% their thickness. Their surfaces should not be shiny, to avoid reflection of laser light on the front face and to produce a strong signal on the rear one, it is common to apply a thin coating layer of high emissivity material, such as graphite.

3.2.3 Differential scanning calorimeter: DSC Pegasus 404C

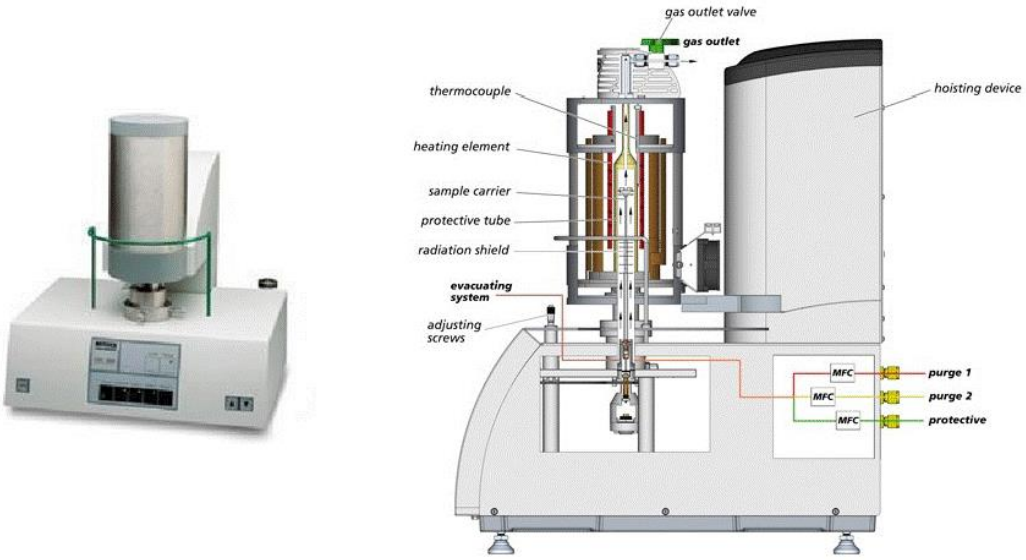

Figure 3.7 DSC Pegasus 404 C by NETZSCH and its schematic view.

The specific heat measurements are carried out with the differential scanning calorimetry DSC Pegasus 404 C by NETZSCH. The rhodium furnace is air cooled and it allows to reach 1650 °C, it can operate under vacuum or inert atmosphere. The sample holder is a Pt/Rh sensor that can host the two crucibles (as explained in 0) and senses the temperature of the test specimen and the reference pan. Its position can be adjusted by means of two micrometric screws, to have a uniform heating of the two crucibles. An oxygen trap system is also positioned on top of the shielding plates of the sample holder: this small getter is useful to reduce the amount of oxygen below 1 ppm (Figure 3.8).

Figure 3.8 Sample holder and OTS system.

Some key technical data are listed in Table 3.11.

Technical data	
Temperature range	RT-1650 °C
Reproducibility	<0.3 K for temperatures below 1000°C
Baseline reproducibility	<±1 mW for T<1500°C <±2.5 mW for T>1500°C
Uncertainty (specific heat)	± 3.5%

Table 3.11 Technical data of the DSC Pegasus 404 C.

The test parameters are listed in Table 3.12:

Instrument set-up		Graphite crucibles + alumina washers
Atmosphere		Ar 50 ml/min
Temperature program	Isothermal step Heating phase Isothermal step	20 min at 25 °C 15 K/min up to 700 °C 20 min at 700 °C

Table 3.12 Calorimetry test set-up.

DIN 51 007: General principles of differential thermal analysis (18)

This standard covers a variety of methods to analyze solid and liquid materials through the differential scanning calorimetry like chemical reactions, glass transition temperatures, phase transitions and specific heat capacity. It describes the concepts, apparatus, procedures, test specimens and evaluation. Some of the most important recommendation and good practices are:

- Apparatus:
    - The furnace shall be able to cover heating rates from 1 to 50 °C/min.

  - The temperature control should maintain a constant heating rate between 5℃/min and 50℃/min to an accuracy of 10%. In the isothermal steps the temperature shall not deviate more than 0.5% from the target temperature. When switching from a dynamic step to an isothermal program the damping in temperature should be less than 20% of the numerical value of the heating rate and the decay time should be less than 5 minutes.
  - When the sample can react with air the test must be done under controlled atmosphere (inert gas). The effect of the gas flow on the thermal measurement must be minimum and its temperature shall reach the specimen temperature by the time it reaches the specimen.
  - The differential temperature shall be measured with a device that have a limit error of no more than 0.5% and it should be able to sense temperature changes of less than 1℃.
- Procedure for measuring specific heat:
  - The measurement is carried out on one empty and one full specimen holder and the temperature program begins with an isothermal step at the initial temperature followed by a dynamic phase and ends with another isothermal step at the final temperature.

3.3 Instruments for the mechanical characterization

3.3.1 Universal testing machine: Zwick/Roell Z400

The machine used to perform the mechanical tests is a universal testing machine tailor made for the mechanical laboratory by Zwick/Roell (see Figure 3.9). It allows to perform tensile, compressive and flexural tests and to host additional fixtures designed at CERN for specific purposes.

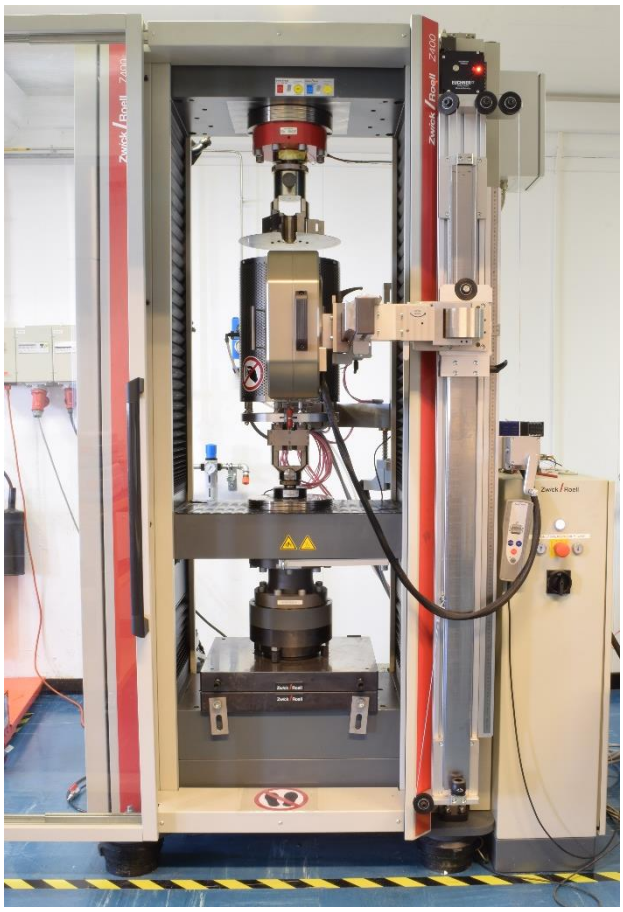

Figure 3.9 Universal testing machine Zwick Z400.

Some of the key features of the machine are listed in Table 3.13:

Component	Features
Machine	4 columns, electro-mechanical drive by two ball screws, two test areas, test speed 0.001 ÷ 250 mm/min, resolution crosshead motion 0.024 µm
High capacity load cells	400 kN 250 kN
Compression plates	55 HRC hardness 0.05 mm planarity upper plate spherically mounted

Table 3.13 Features of the universal testing machine Zwick Z400.

Compression test set-up

The compressive test set-up requires that the top plate sit on a top of a spherical bearing block. The sample is simply positioned between the compression plates in the bottom part of the

machine. The co-axiality with the machine is checked visually and minimized to reduce the effect of eccentric loading.

The test parameters adopted in the campaign are listed in Table 3.14:

Force sensor	Zwick loadcell 250 kN
Strain sensor	HBM strain gage 1-LY11-3/350
Crosshead motion rate	0.1 - 0.5 mm/min
Preload	20 N
Support span	20 mm
Loading span	10 mm

Table 3.14 Compression test parameters.

ASTM C695: Standard test method for compressive strength of carbon and graphite (19)

This test method claims some good practices regarding the apparatus, test specimen and procedure regarding the determination of the compressive strength over carbon and graphite products. The compression test provides a measure of the maximum loading capacity of these materials, which typically support higher loads in compression. Among the recommendation:

- The test specimens should be cylinder with planar ends faces perpendicular to the cylindrical surface to within 0.001 mm/mm of diameter. The edges should be sharp and without flaws. The diameter should be greater than 10 times the maximum particle size. The ratio height/diameter should range between 1.9 and 2.1.
- Regarding the positioning, the deviation of the specimen axis to the machine axis should be within 5% of the sample diameter. The load should be applied continuously at a constant rate of the crosshead displacement. The crosshead rate should lead to breaking times higher than 30 s.

Flexural set-up

The 4-point bending test is performed with a dedicated fixture realized at CERN's workshop, which allow to adjust the loading and support spans and to change the interfacing components' material. This results in a flexible tooling able to house specimens of various sizes and to properly test materials with completely different mechanical properties (plastic, ceramics and metals). The set-up used to test the specimens object of this work is shown in Figure 3.10: the support blocks are made of steel AISI 304L, the rollers of tungsten carbide and their diameter is 6 mm.

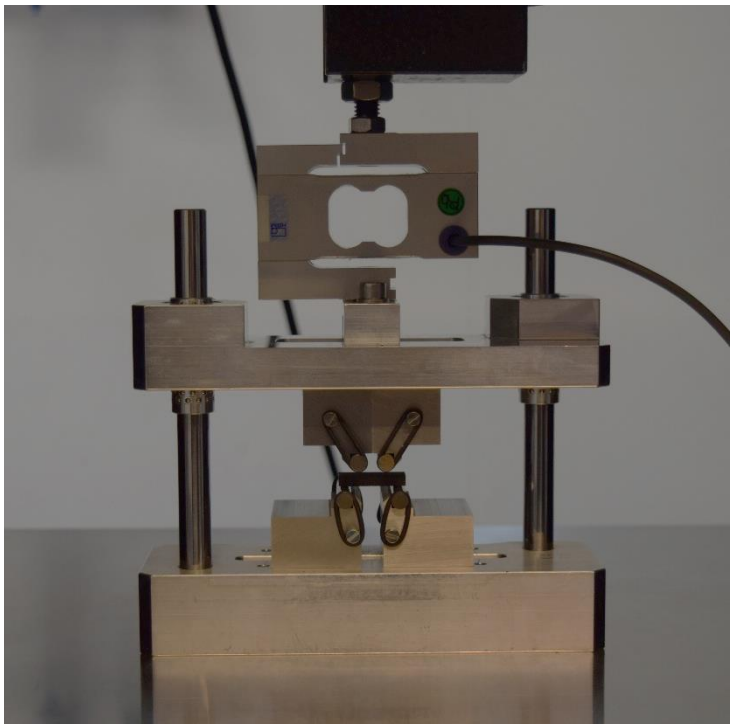

Figure 3.10 Fixture for the 4-point bending test.

Force sensor	HBM load cell S2M 1000 N
Strain sensor	HBM strain gage 1-LY11-3/350
Crosshead motion rate	0.1 mm/min
Preload	0 - 20 N

Table 3.15 Bending test parameters.

ASTM C1161: Standard test method for flexural strength for advanced ceramics at ambient temperature (20)

The standard provides indications regarding the preparation and execution of the flexural test in both 3- and 4-point configuration over advanced ceramic materials. Some of the key aspects are:

- Apparatus
    - The loading should be done in any suitable machine capable to provide a uniform rate. Its accuracy should be within 0.5%.
    - The bearings of the fixture must be free to roll outward (support bearings) and inward (loading bearings), to relieve frictional constraints.
- Specimen
    - The test specimen has rectangular cross section of standardized dimensions and its four longitudinal faces should be parallel within 0.015 mm.

- Carefully handle and store the test specimens to avoid introduction of random flaws.

- Procedure
  - The preload should be choses so that the corresponding stress don't exceed 25% of the mean strength.
  - The crosshead rate should be chosen so that the strain rate in the sample is in the order of $1*10^{-4}$ s^{-1}. The strain rate is evaluated as $\in= 6ds/L\hat{}2$ where d is the thickness, s the crosshead speed and L the support span. The times to failure for ceramics range between 3 and 30 s.

3.3.2 Impact excitation technique

IET set-up and devices

The set-up adopted to carry out the impact excitation technique is very simple and it is shown in Figure 3.11. The test specimen is supported by two wires that can be positioned in correspondence of the antinode lines. The specimen is excited by striking it with a small mass attached to the extremity of a flexible bar. The frequencies excited are sensed by a microphone connected to a spectrum analyzer. The analysis of the spectrum is done by means of the PAK software.

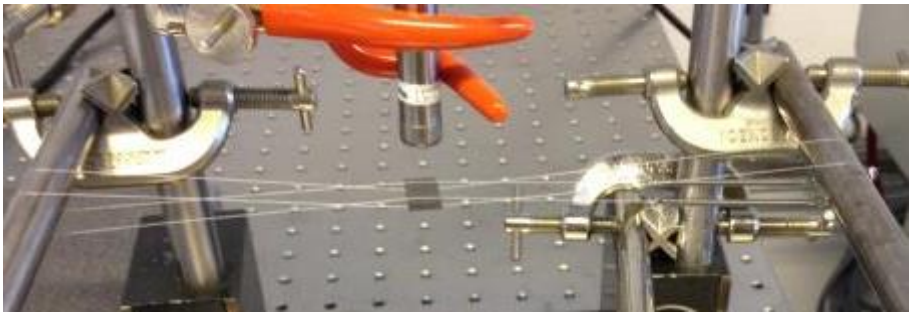

Figure 3.11 IET set-up.

ASTM C1259: Standard test method for dynamic Young's modulus, shear modulus, and Poisson's ratio for advanced ceramics by impulse excitation of vibration (21)

The test method describes the procedure to determine the dynamic Young's modulus, using the resonant frequency in the flexural mode of vibration, and the dynamic shear modulus, using the torsional resonant mode of vibration. The Poisson's ratio is computed starting from these two. Although the relationship between resonant frequency and dynamic modulus stated in the standard are only valid for homogeneous, elastic and isotropic materials, the good practices and

recommendations are adopted for the tests carried out on the materials object of this study to determine the resonant frequency. If anisotropy and inhomogeneity are considered it is also possible to determine the elastic properties for these materials. Some of the key points of the procedure are:

- Apparatus
    - It consists of an excitation tool, a transducer to convert the mechanical vibration into electrical signal, an electronic system (signal amplifier/conditioner, signal analyzer and frequency readout device) and a support system.
    - The impulse should induce a measurable mechanical vibration without displacing or damaging the specimen. The transducer frequency range would be 100 Hz ÷ 50 kHz.
    - The support should isolate the test specimen from outer vibration without restricting the mode of vibration of interest. Test specimens should be supported along the nodal lines.
- Test specimen:
    - Its shape ratio shall be chosen so that the resonant frequency fall within the range of measurement of the transducer.
    - Its surfaces should be flat. Opposite surfaces across the length and width should be parallel within 0.01 mm or ± 0.1%, opposite surfaces across the thickness within 0.002 mm or ± 0.1%.
- Procedure
    - (out-of-plane flexure) Place the non-contact transducer over an antinode point close enough to sense the vibration of interest. Strike the specimen lightly and elastically either at the center or at the edges.
    - (torsional resonant frequency) locate the transducer over a quadrant of the specimen, possibly at 0.224L from the end and near the edge. Strike the specimen at the opposite quadrant, to minimize the excitation of the flexural mode.

4 Results

In this chapter are stated the results of the thermo-physical and mechanical characterization performed over the two materials objects of the thesis. Most of the charts show the measurement of one sample, considered representative of the batch. In any case, the scatter between measurements of the same kind of sample is within the instruments uncertainties.

4.1 CFC FS140®

4.1.1 Thermo-physical characterization

Thermal expansion and CTE

The thermal expansion is measured with the pushrod dilatometer described in 3.2.1 and the CTE evaluated with the method explained in 2.1.3. A measurement of each sample has been carried out with the parameters described in Table 3.8. Not all the samples received have been tested as shown in Table 4.1, containing also the specimen's length before and after the test.

Tested/received			Initial length [mm]	Final length [mm]
yz	3/6	Sample 1	25.023	25.023
		Sample 2	25.040	25.038
		Sample 3	25.043	25.048
x	3/6	Sample 1	25.058	25.060
		Sample 2	25.074	25.089
		Sample 3	25.038	25.044
Reference temperature			Heating phase: 30°C Cooling phase: 40°C	

Table 4.1 CFC FS140® dilatometry samples details.

The graphs below depict the thermal expansion and CTE against the temperature, for *yz* and *x* samples, measured during the heating and cooling phases. For easy of exhibition only one curve per set of samples is shown: the maximum deviation of the other two samples is stated for each case in the corresponding caption.

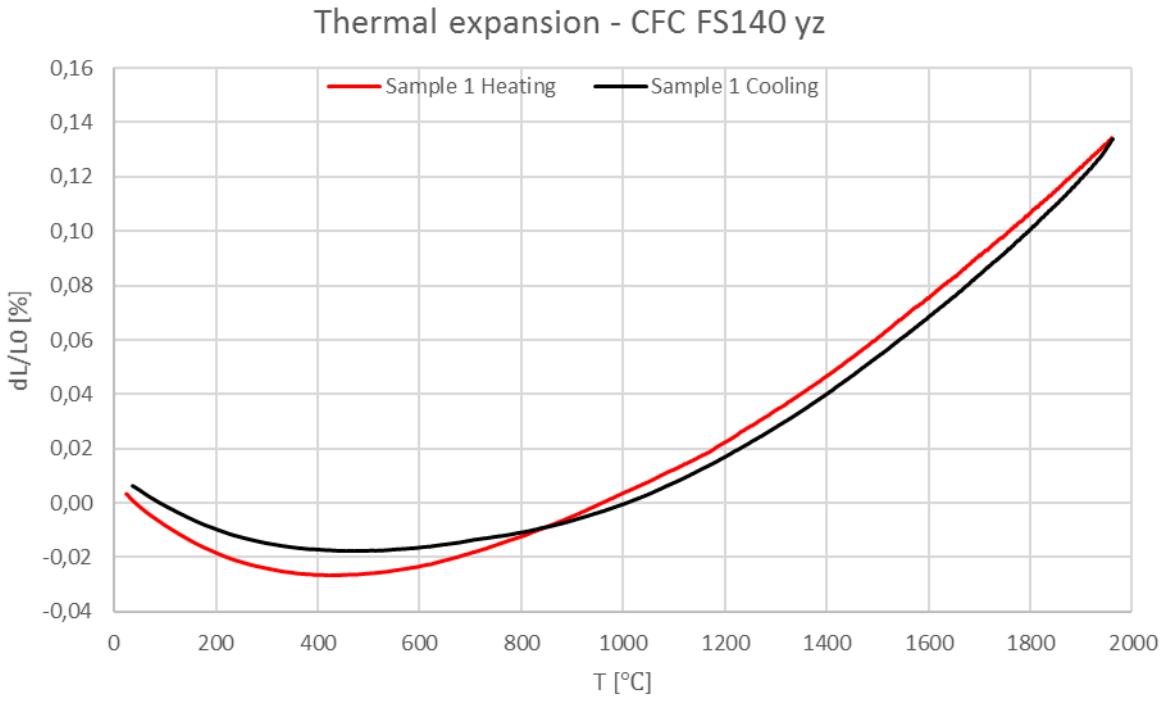

Figure 4.1 Thermal expansion against temperature for a **yz** sample of CFC FS140®, in the heating and cooling phases. Max deviation from these values is 5.3 10^{-3} %.

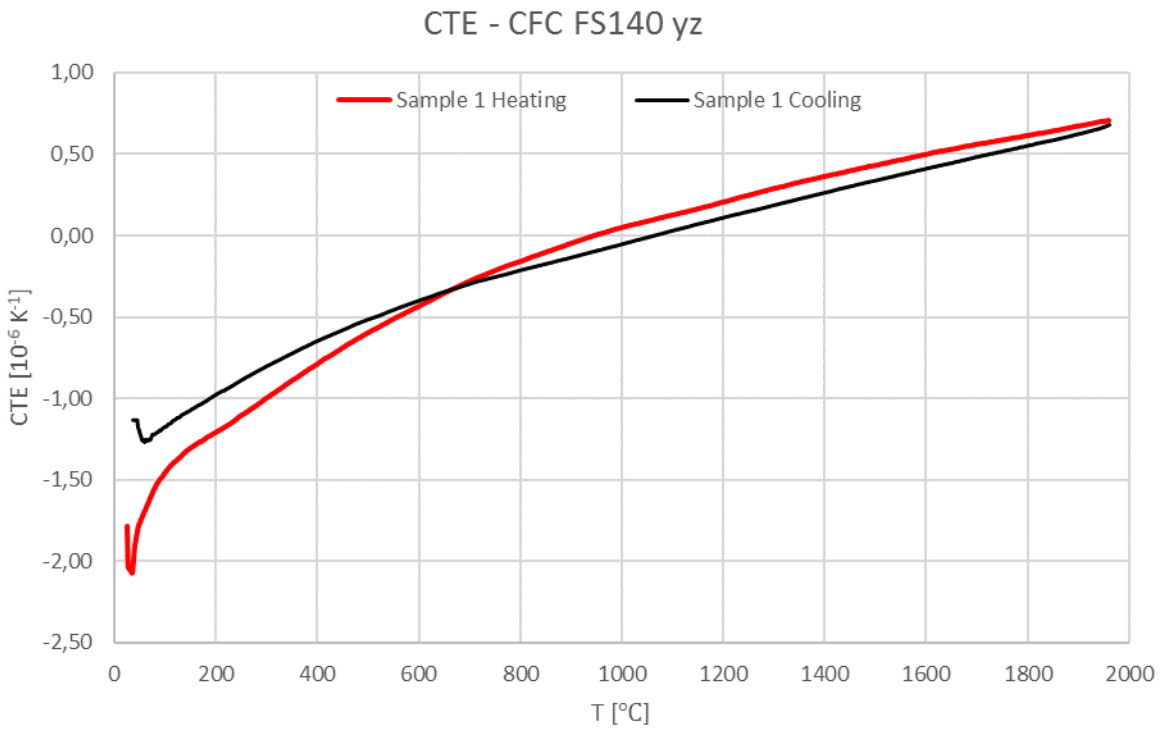

Figure 4.2 Coefficient of thermal expansion versus temperature for a **yz** sample of CFC FS140®, evaluated during the heating and cooling phases. Max deviation from these values is 0.33 10^{-6} K^{-1} during heating and 0.11 10^{-6} K^{-1} during cooling.

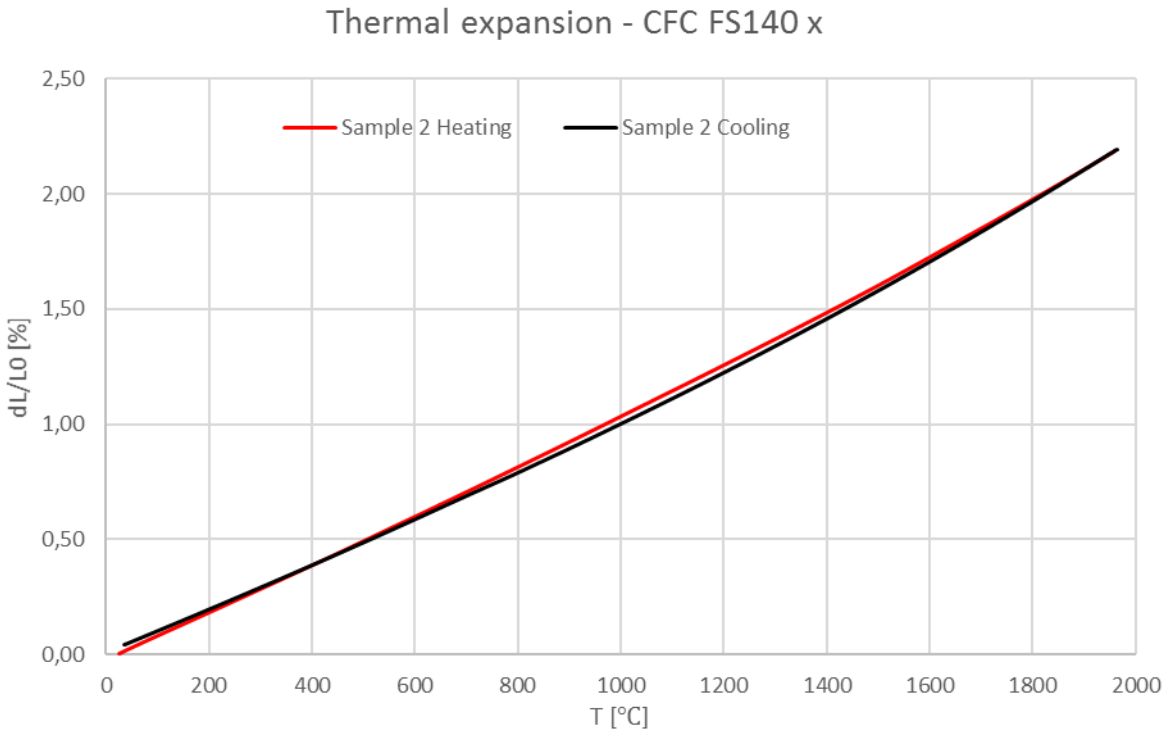

Figure 4.3 Thermal expansion against temperature for a **x** sample of CFC FS140®, in the heating and cooling phases. Max deviation from these values 2%.

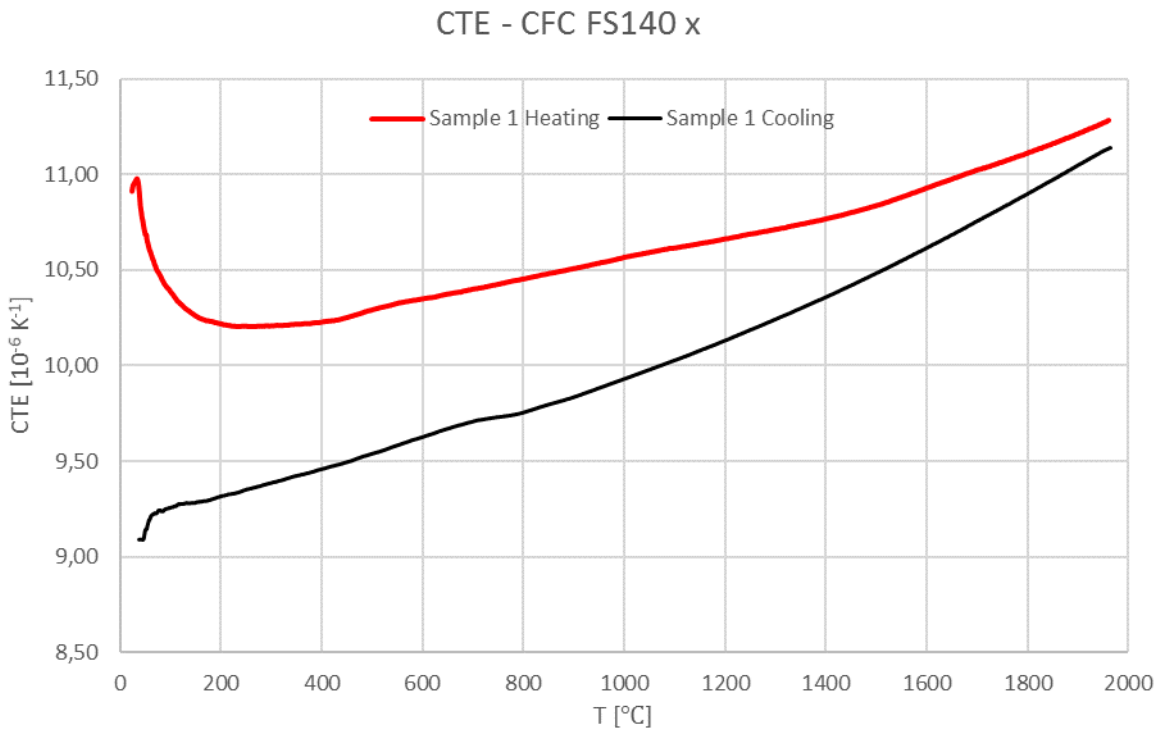

Figure 4.4 Coefficient of thermal expansion versus temperature for a **x** sample of CFC FS140®, evaluated during the heating phase. Max deviation from these values is 0.44 10^{-6} K^{-1} during the heating phase and 0.28 10^{-6} K^{-1} during the cooling phase.

Specific heat

The calorimetry analysis has been performed with the differential scanning calorimeter described in 3.2.3, and the specific heat evaluated with the method described in 2.1.2. The overview of the tested samples is listed in Table 4.2, while the test parameters are stated in Table 3.12.

Tested/received		**Mass [mg]**
3/6	Sample 1	24.6
	Sample 2	24.7
	Sample 3	25.4
Reference material	POCO graphite	40.6 mg

Table 4.2 CFC FS140® calorimetry samples details.

Every specimen has been tested three times but in the graphs below only the average of these three tests is reported for each sample. The maximum standard deviation between measurements over the same sample is 0.04 J/gK.

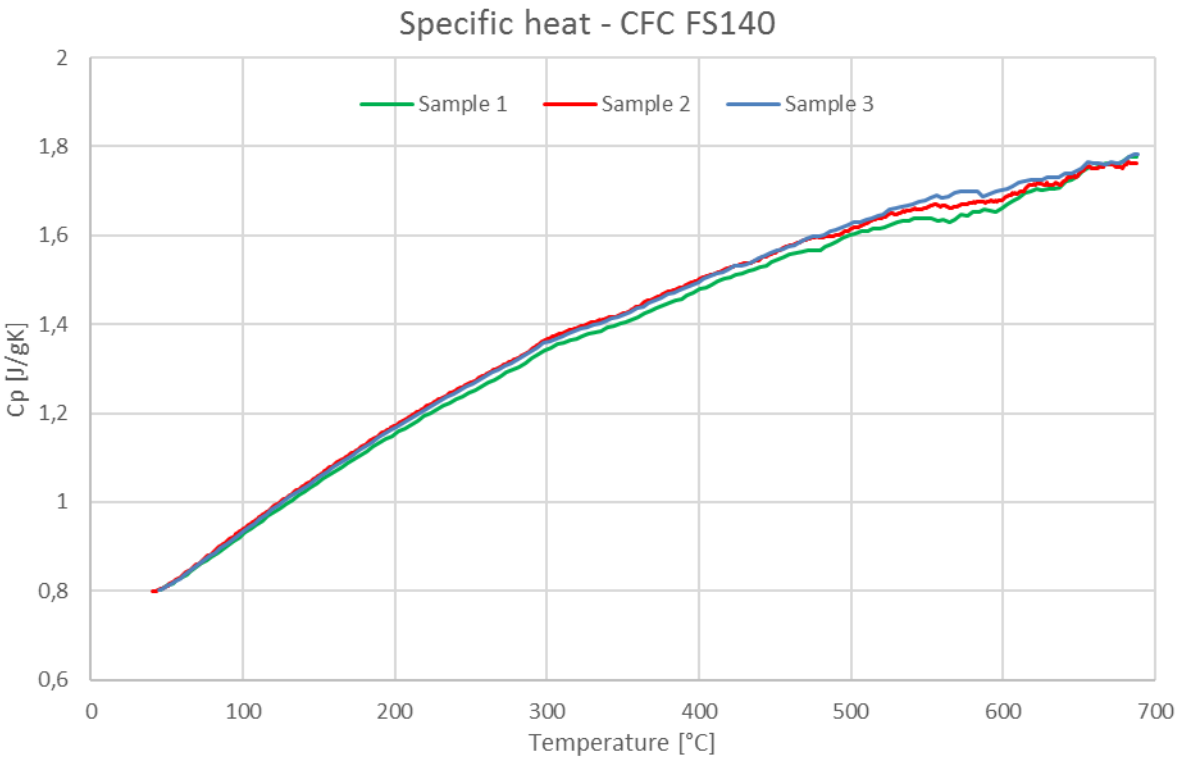

Figure 4.5 Average curves of specific heat vs temperature for three different CFC FS140®.

Thermal diffusivity and thermal conductivity

The thermal diffusivity is measured by means of the laser flash apparatus described in 3.2.2 applying the Cape-Lehman model explained in 2.1.6. The test parameters are stated in Table 3.10. The thermal diffusivity is inversely proportional to the specimen's thickness to the square power: as the temperature increase the thickness changes accordingly to the coefficient of thermal expansion. This is taken into account using the CTE values measured through dilatometry: for the yz LFA samples, the thickness variation is calculated with the CTE measured in the x direction and vice versa. In Figure 4.6 and Figure 4.7, is shown the thermal diffusivity variation with temperature for three different samples in the two directions. Every sample has been tested once.

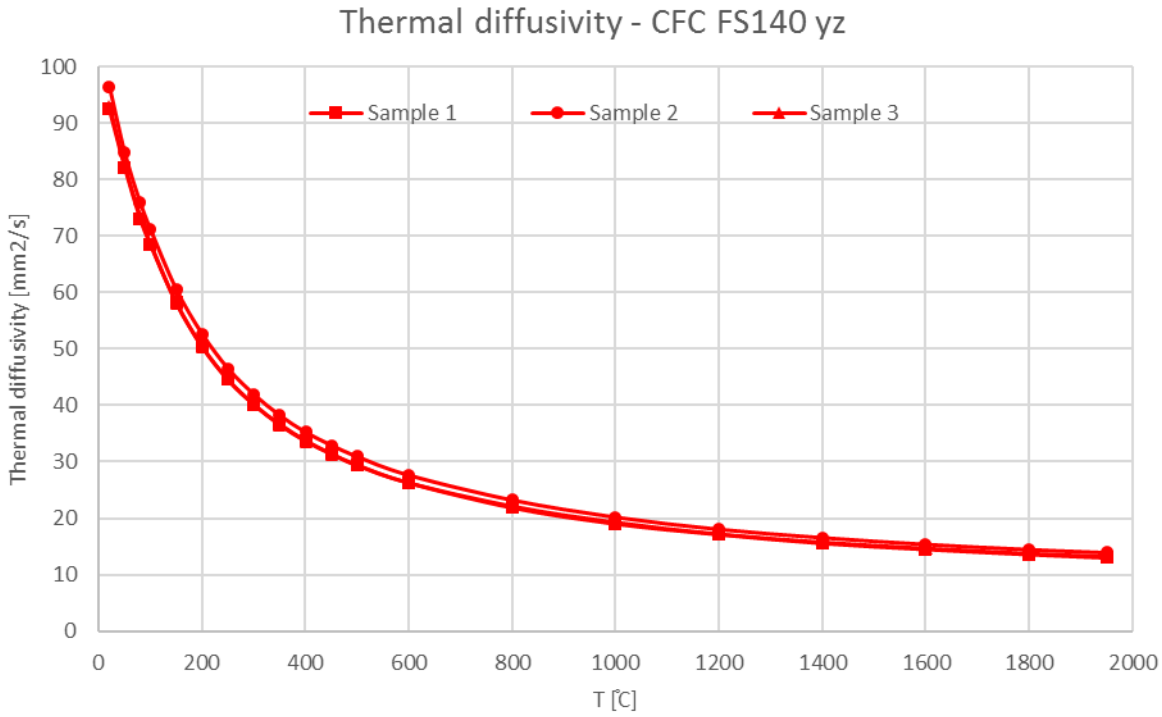

Figure 4.6 Thermal diffusivity vs temperature of three CFC FS140® **yz** samples.

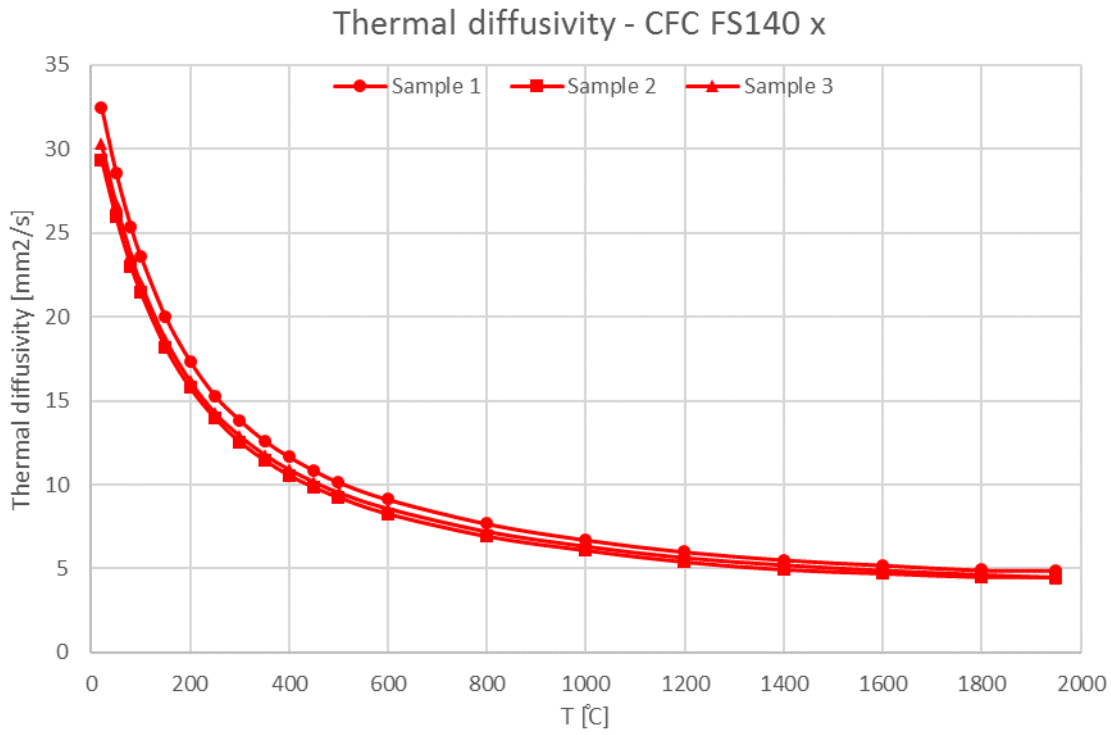

Figure 4.7 Thermal diffusivity vs temperature of three CFC FS140® **x** samples.

The thermal conductivity is calculated starting from the measured thermal diffusivity, with equation 2.20, here stated again for clarity: $\lambda(T) = \alpha(T)\rho(T)c_p(T)$, where $\alpha(T)$ is the thermal diffusivity, $\rho(T)$ is the density and $c_p(T)$ the specific heat. The specific heat values have been measured by calorimetry up to ~700 °C, while the range of measurement of the thermal diffusivity ranges from room temperature to 1950 °C: in the calculation of the thermal conductivity the values of specific heat at temperature above 700 °C have been kept constant and equivalent to the measured value at 700 °C (conservative hypothesis). Also, the density of the material is a function of the temperature: the change in volume is taken into account by correcting the diameter and the thickness of the sample with the measured values of CTE in the corresponding directions. In Figure 4.8 and Figure 4.9, it is shown the thermal conductivity calculated from room temperature to 1950 °C.

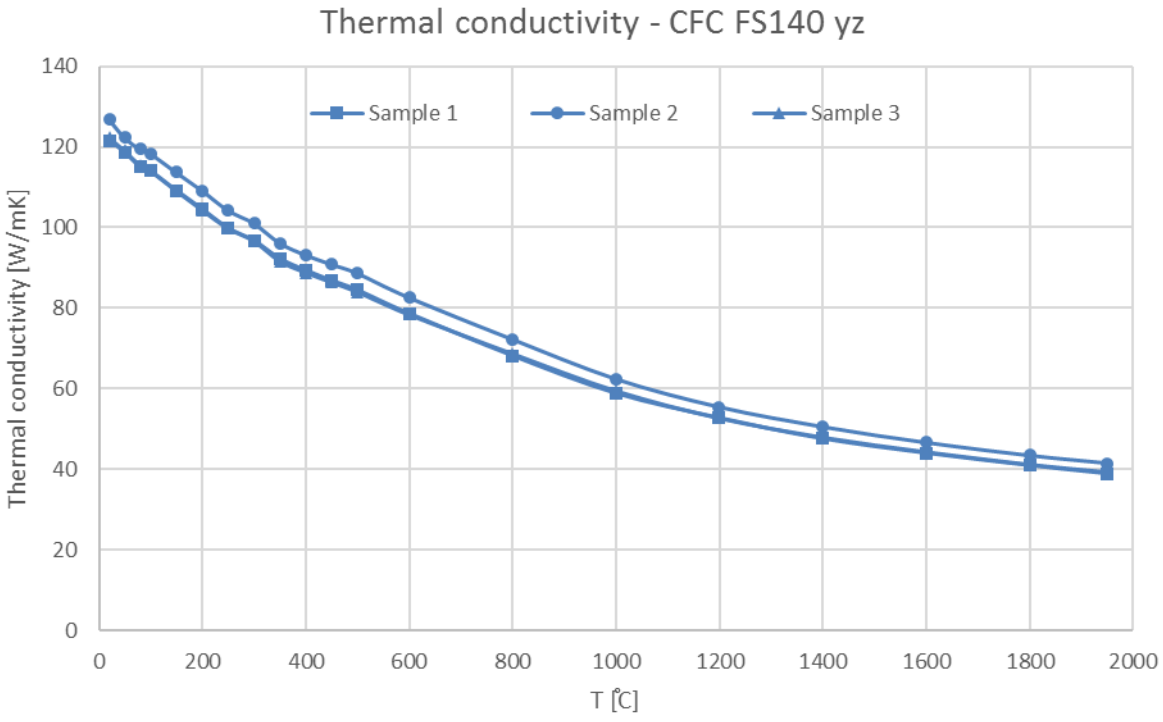

Figure 4.8 Thermal conductivity vs temperature of three CFC FS140® **yz** samples.

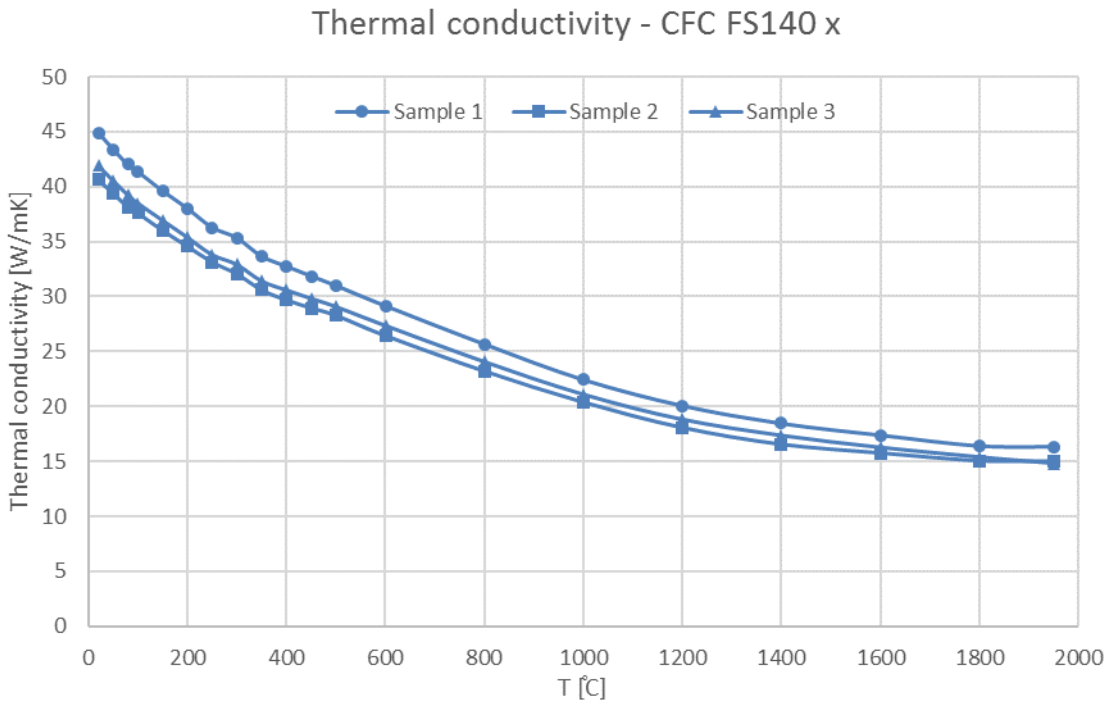

Figure 4.9 Thermal conductivity vs temperature of three CFC FS140® **x** samples.

4.1.2 Mechanical characterization

Compression test

The compression tests were carried out using the universal testing machine and the configuration described in 3.3.1, over three sample per direction machined with the geometry stated in Table 3.1. The results of the tests are shown in the following Figure 4.10 and Figure 4.11. In the case of the x samples (see Figure 4.11) the choice of the strain gauges was not adequate because unable to bear such big deformation. Hence, the values of the compression stresses to rupture are stated in the legend and in Table 4.3, which contains also the other meaningful results of the compression tests.

Compressive properties		Stress to rupture [MPa]	Strain to rupture [µm/m]
yz	Sample 1	94.4	1123
	Sample 2	101.7	761
	Sample 3	99.3	656
x	Sample 1	92.6	-
	Sample 2	86.6	-
	Sample 3	90.1	-

Table 4.3 Compressive properties of CFC FS140®. No data available for strain to rupture.

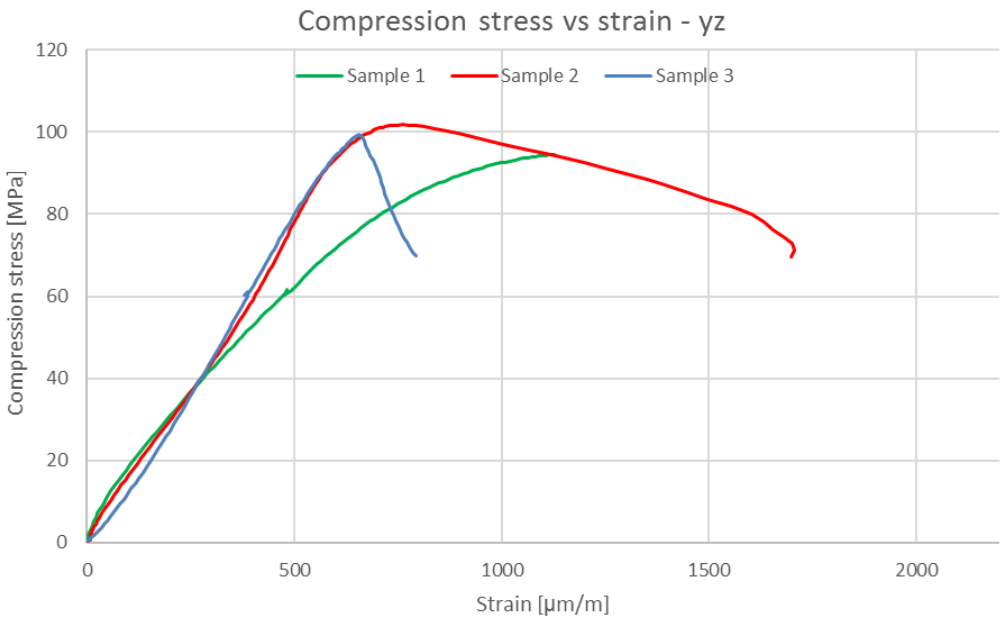

Figure 4.10 Compression stress vs strain of three CFC FS140® **yz** samples.

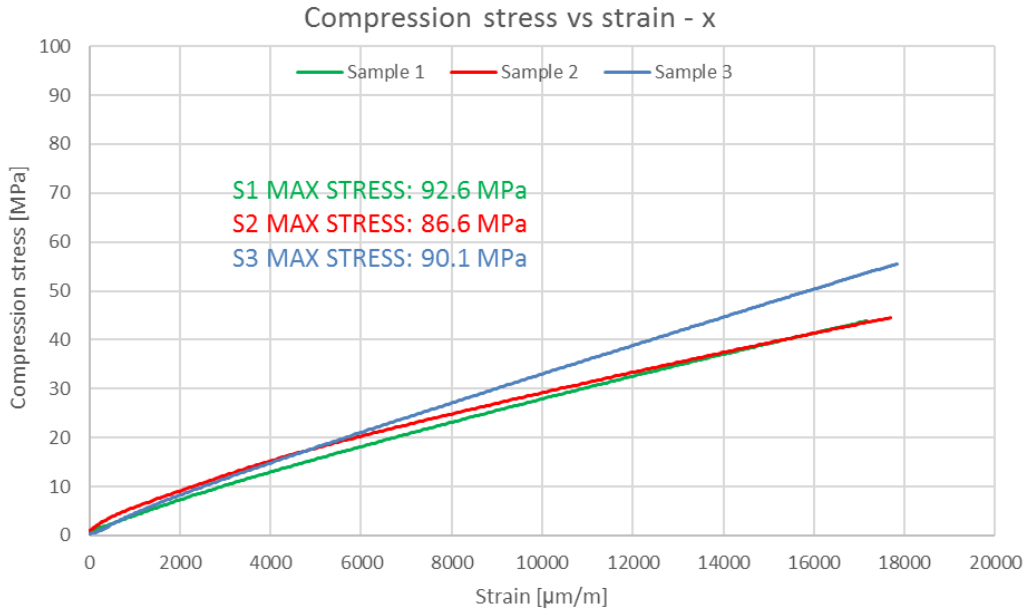

Figure 4.11 Compression stress vs strain of three CFC FS140® **x** samples.

In Figure 4.12 it is possible to appreciate the diverse kinds of fracture occurred in the *yz* and *x* samples.

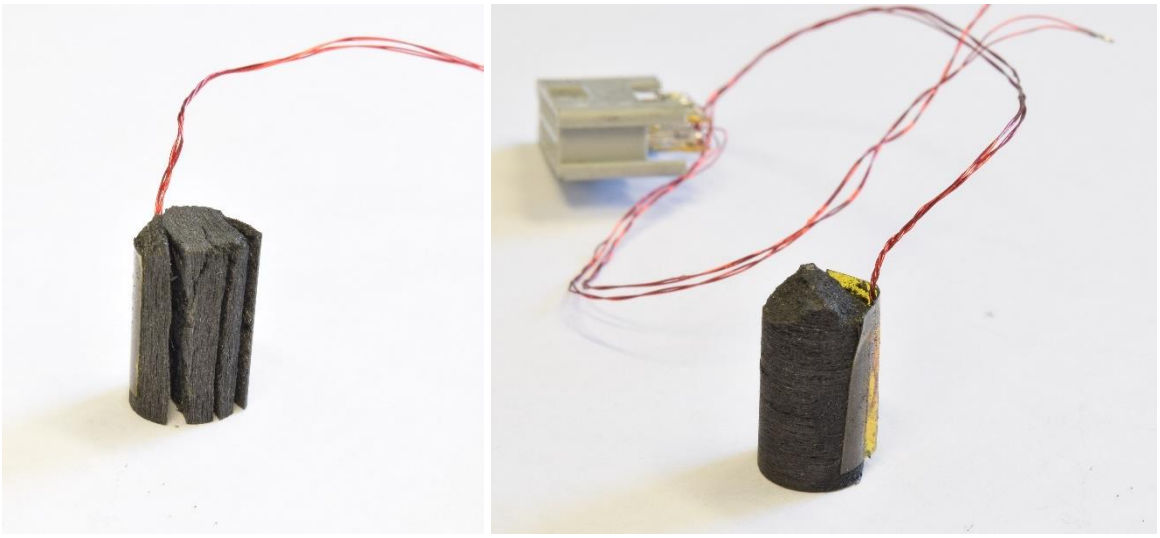

Figure 4.12 Diverse ways of fracture due to compression stresses in the CFC FS140® **yz** sample (left) and in the **x** one (right).

Flexural test

The 4-point bending test was performed with the configuration described in 3.3.1, over three samples per direction, cut in the shape stated in Table 3.1. In the pictures below, the results of the tests.

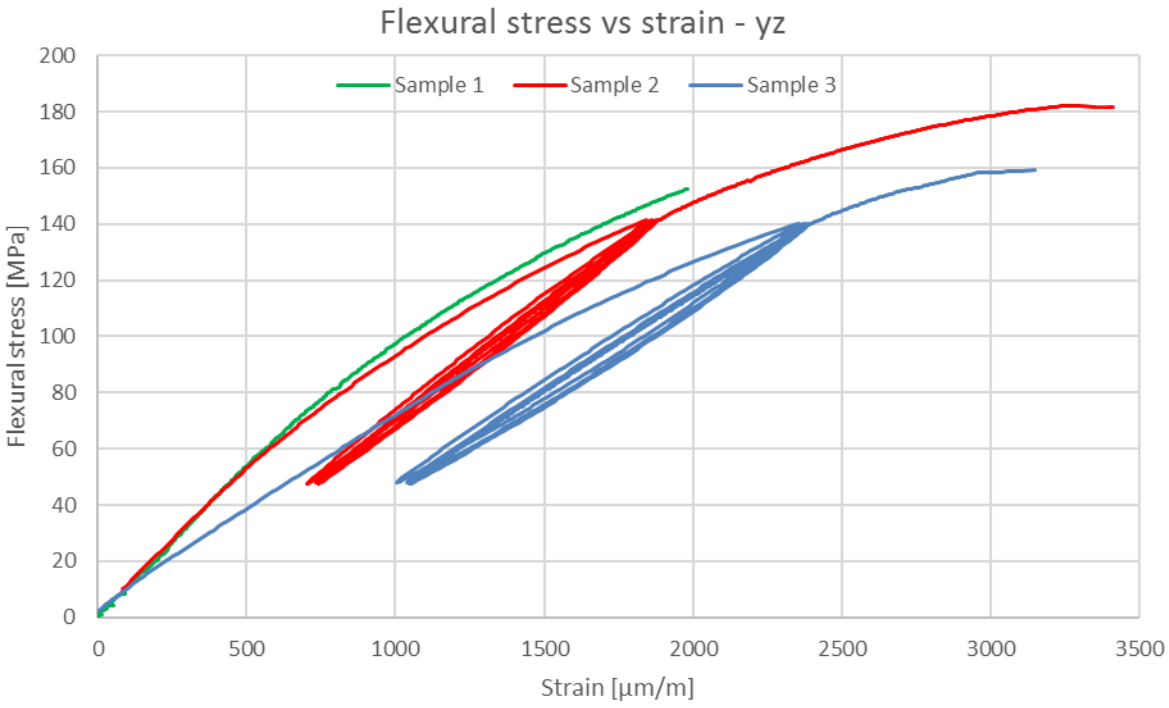

Figure 4.13 Flexural stress vs strain of three CFC FS140® **yz** samples.

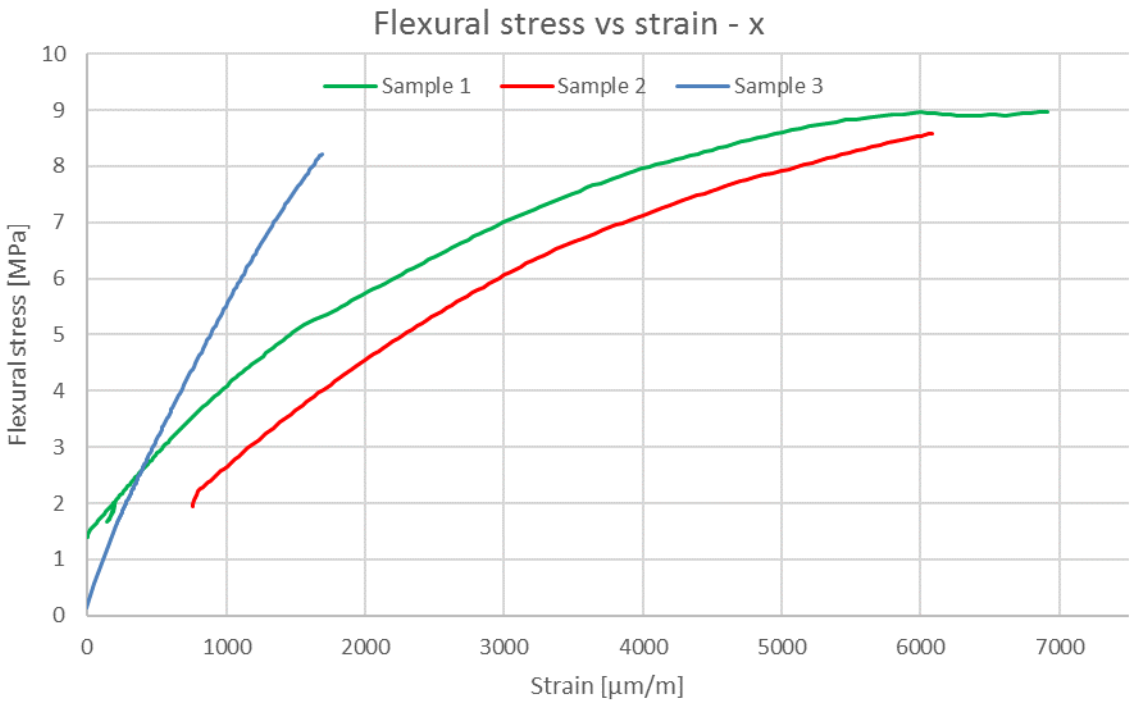

Figure 4.14 Flexural stress vs strain of three CFC FS140® **x** samples.

During the test over the "Sample 2 **yz**" and "Sample 3 **yz**" five loading/unloading cycles have been performed to determine the Young's modulus.

Flexural properties		Stress to rupture [MPa]	Strain to rupture [µm/m]	E [GPa]
yz	Sample 1	152.5	1980	-
	Sample 2	182.0	3414	80
	Sample 3	159.0	3150	66
x	Sample 1	9.0	7152	
	Sample 2	8.6	6084	-
	Sample 3	8.2	1689	

Table 4.4 Flexural properties of CFC FS140®.

The curves shown in Figure 4.14 corresponds to different tests conditions: for "Sample 1 x" and "Sample 2 x" a pre-load of 20 N was set and the strain gauge output signal set to zero when this preload was reached. Only at the end of the test, in the light of the total strain imposed, resulted that the initial strain achieved during the preload was not negligible. Consequently for "Sample 3" the pre-load was not applied. "Sample 2" initial point does not correspond to 0 µm/m because the strain gauge was not zeroed after the application of the pre-load.

In Figure 4.15 it is possible to appreciate the two different kinds of fracture for specimen when the load is applied perpendicularly or in parallel to the planes of the CFs.

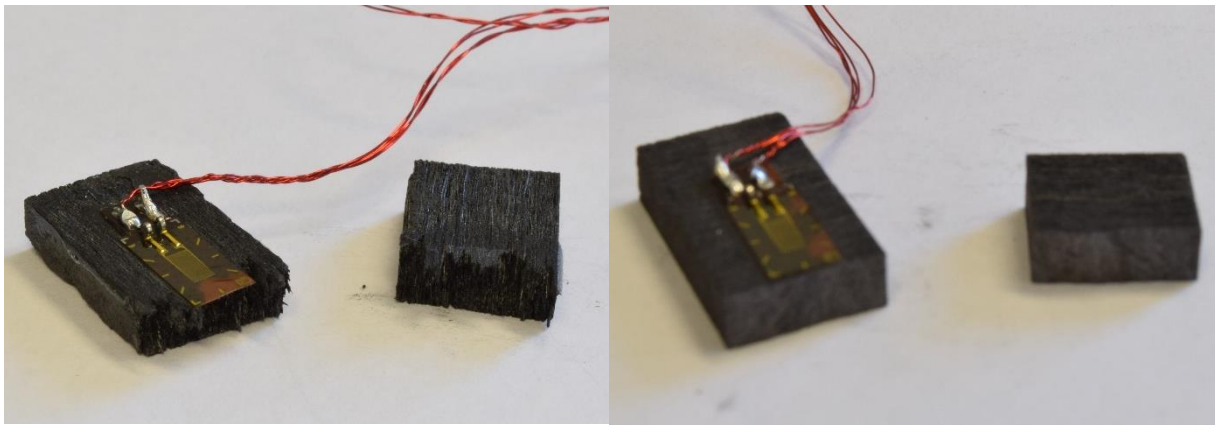

Figure 4.15 Diverse ways of fracture due to flexural stresses in the CFC FS140® **yz** sample (left) and in the **x** one (right).

Impact excitation technique

The measurement of the resonant frequencies of the material was carried out using the configuration described in 3.3.2. The tests are normally carried out over the same samples that will then be used in the destructive bending test. A first attempt of determining the first flexural mode of the material in the *yz* direction was done but it had been discarded in the light of the E modulus values determined with the flexural test. Additional tests were carried out over spare samples, to look for the modes of interest in a more suitable range of frequencies. Performing the test was challenging due to the damping of the material and the limit of the electronics, hence reliable results cannot be stated for this material.

4.2 MG-6403-Fc

4.2.1 Thermo-physical characterization

Thermal expansion and CTE

The thermal expansion is measured with the pushrod dilatometer described in 3.2.1 and the CTE evaluated with the method explained in 2.1.3. A measurement of each sample has been carried out with the parameters described in Table 3.8. The number of sample tested and their initial and final length are stated in Table 4.5.

The graphs below depict the thermal expansion and CTE against the temperature, for yz and x samples, measured during the heating and cooling phases. For the sake of clarity only one curve per set of samples is shown: the maximum deviation of the other two samples is stated for each case in the corresponding caption.

	Tested/received		Initial length [mm]	Final length [mm]
yz	3/3	Sample 1	14.969	-
		Sample 2	15.022	15.024
		Sample 3	15.021	15.022
x	3/3	Sample 1	14.965	14.993
		Sample 2	14.991	15.020
		Sample 3	14.976	15.016
Reference temperature			Heating phase: 30°C Cooling phase: 40°C	

Table 4.5 MG-6403-Fc dilatometry samples details.

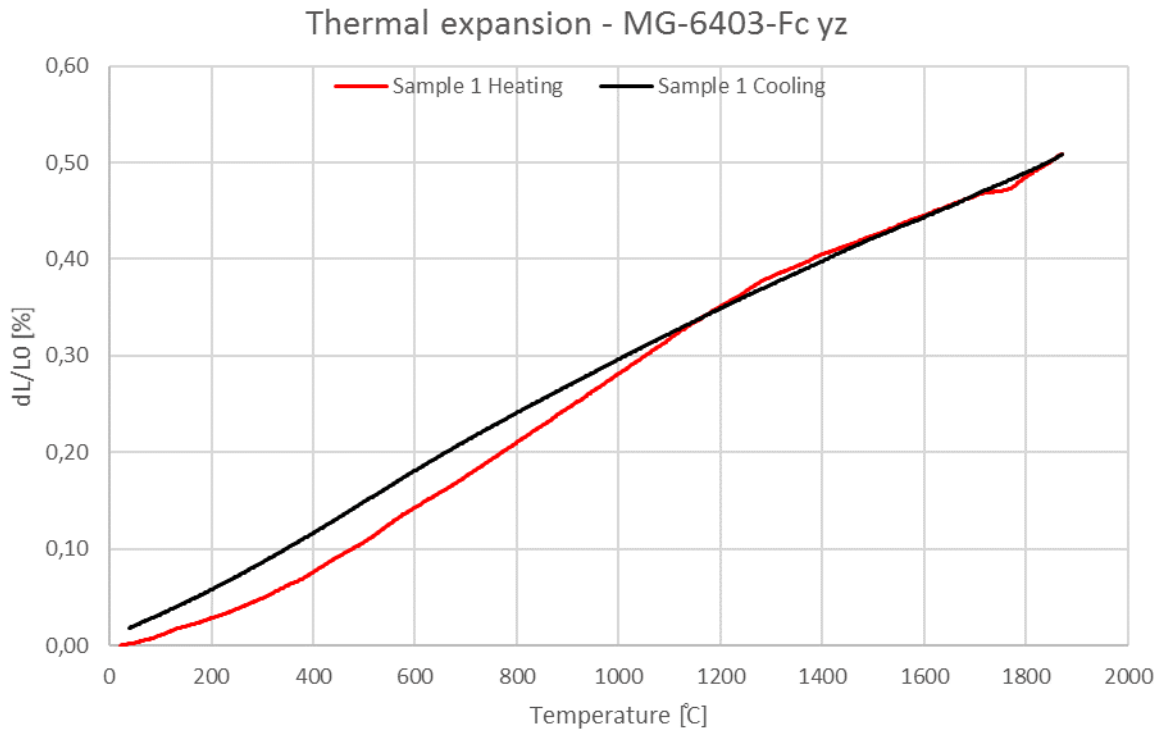

Figure 4.16 Thermal expansion against temperature for a **yz** sample of MG-6403-Fc, in the heating and cooling phases. Max deviation from these values is 22 10^{-3} %.

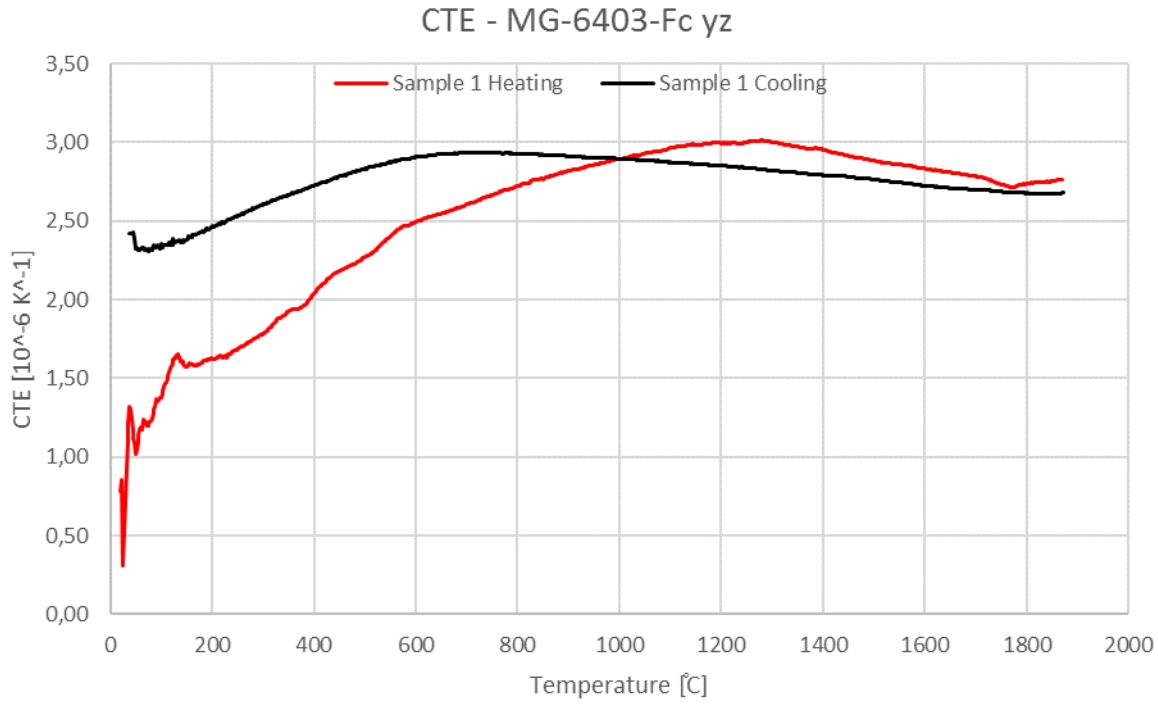

Figure 4.17 Coefficient of thermal expansion versus temperature for a **yz** sample of MG-6403-Fc, evaluated during the heating and cooling phases. Max deviation from these values is 0.15 10^{-6} K^{-1}.

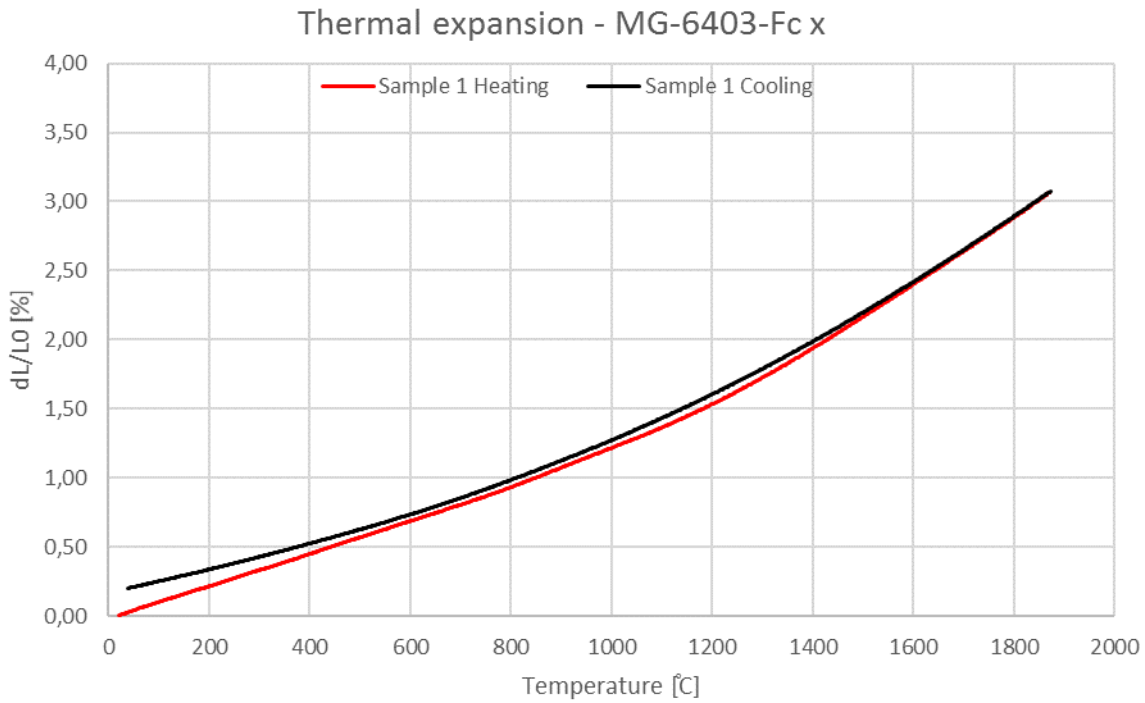

Figure 4.18 Thermal expansion against temperature for a **x** sample of MG-6403-Fc, in the heating and cooling phases. Max deviation from these values is 0.17 %.

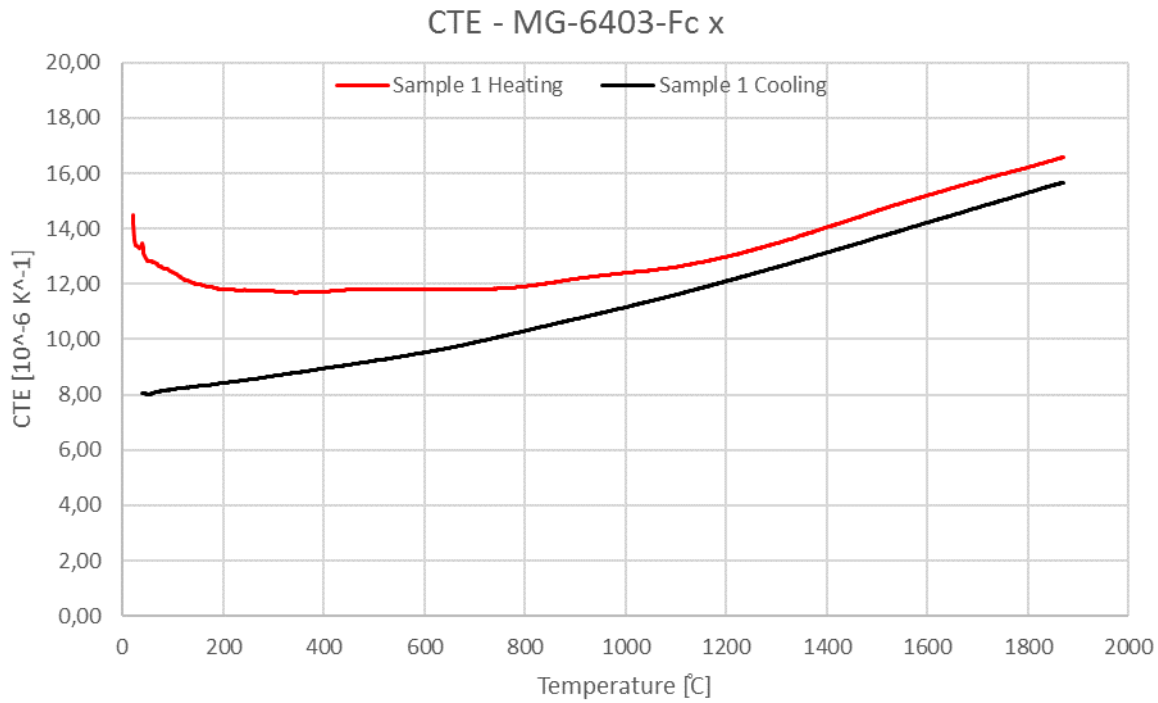

Figure 4.19 Coefficient of thermal expansion versus temperature for a **x** sample of MG-6403-Fc, evaluated during the heating and cooling phases. Max deviation from these values is 2 10^{-6} K^{-1}.

Specific heat

The specific heat of the material has been determined following the method explained in 2.1.2, with the differential scanning calorimeter described in 3.2.3. The temperature program is described in Table 3.12, and the details of the test samples are in the following Table 4.6.

Tested/received		Mass [mg]
3/3	Sample 1	39.4
	Sample 2	39
	Sample 3	40.6
Reference material	Sapphire	

Table 4.6 MG-6403-Fc calorimetry samples details.

Every specimen has been tested three times but in the graphs below only the average of these three tests is reported for each sample. The maximum standard deviation between measurements over the same sample is 0.02 J/gK.

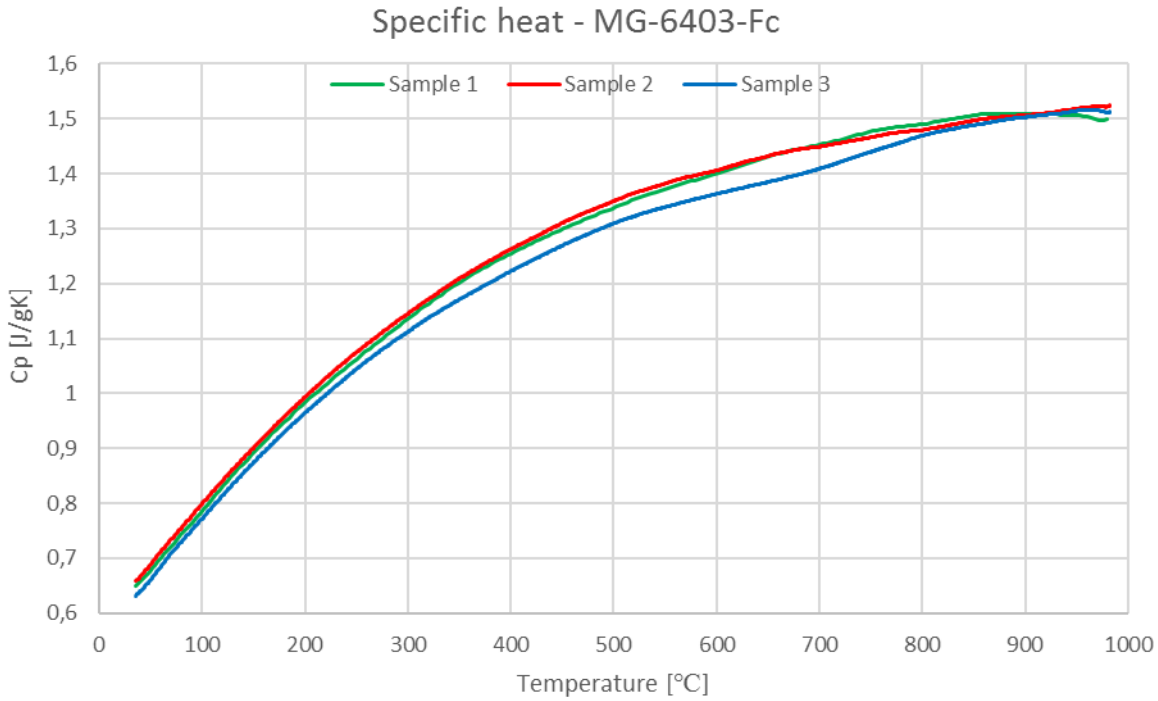

Figure 4.20 Average curves of specific heat vs temperature for three MG-6403-Fc samples.

Thermal diffusivity and thermal conductivity

The same method, instrument and test parameters used to measure the thermal diffusivity of the CFC FS140® have been used to test this MoGR grade. Also in this case, the variation of the specimen thickness is taken into account according to the CTE in the suitable direction. In

Figure 4.21 and Figure 4.22 is depicted the thermal diffusivity variation with the temperature for multiple MG-6403-Fc samples along the two directions. One test has been carried out on each sample.

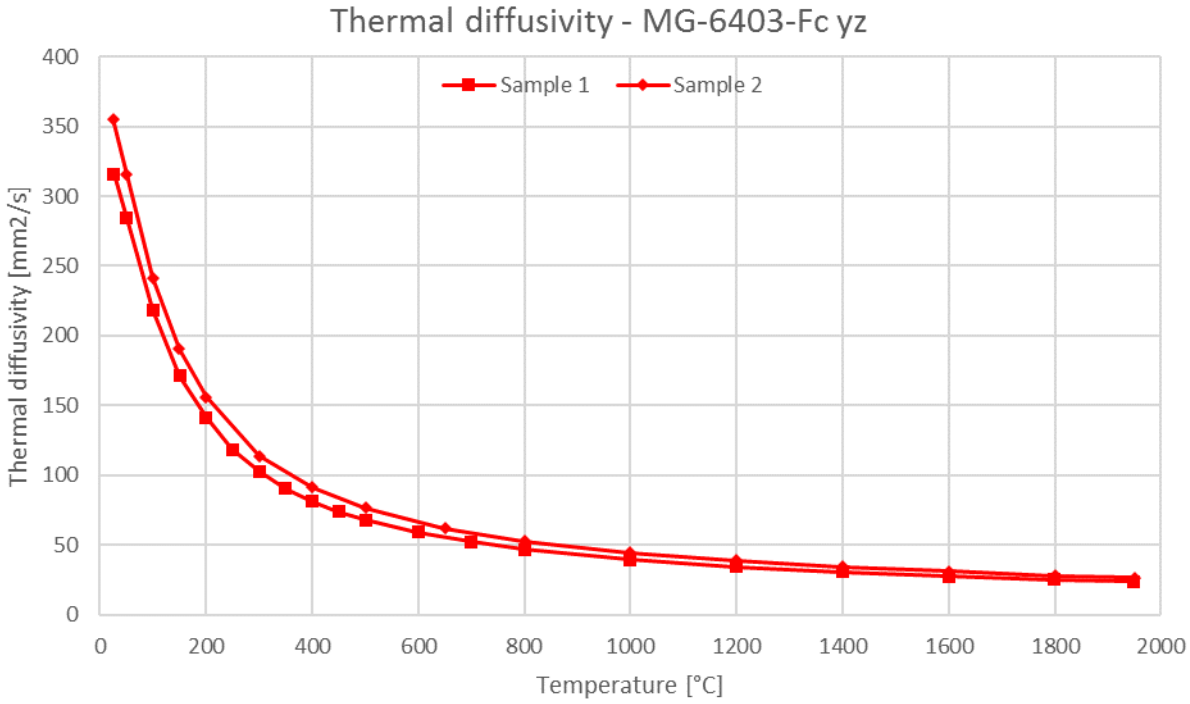

Figure 4.21 Thermal diffusivity vs temperature of two MG-6403-Fc **yz** samples.

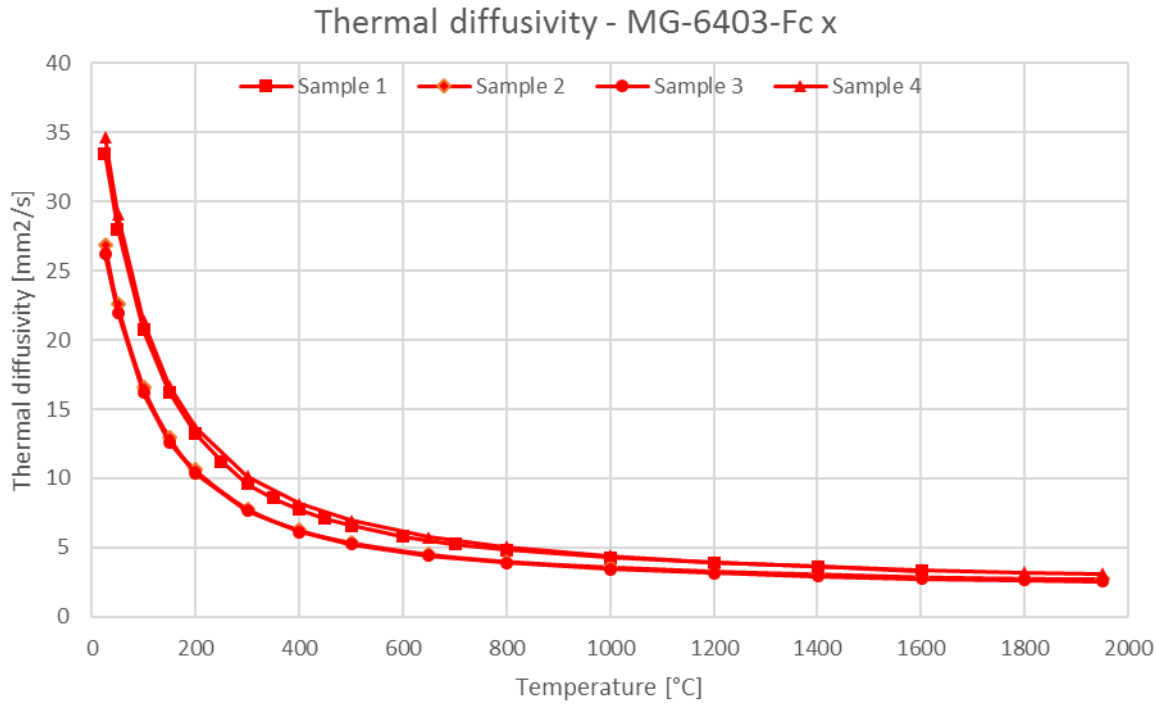

Figure 4.22 Thermal diffusivity vs temperature of four MG-6403-Fc **x** samples.

As for the CFC FS140®, the thermal conductivity has been evaluated with the formula 2.30. The variation of density is corrected thanks to the CTE values measured through dilatometry in the two directions. The specific heat has been measured from room temperature up to ~1000 °C: still being conservative, the value of specific heat used to evaluate the thermal conductivities in the range between 1000 and 1950 °C, has been kept constant and equal to its value at ~1000 °C. The resulting thermal conductivities variation with the temperature for samples in the two directions are depicted in Figure 4.23 and Figure 4.24.

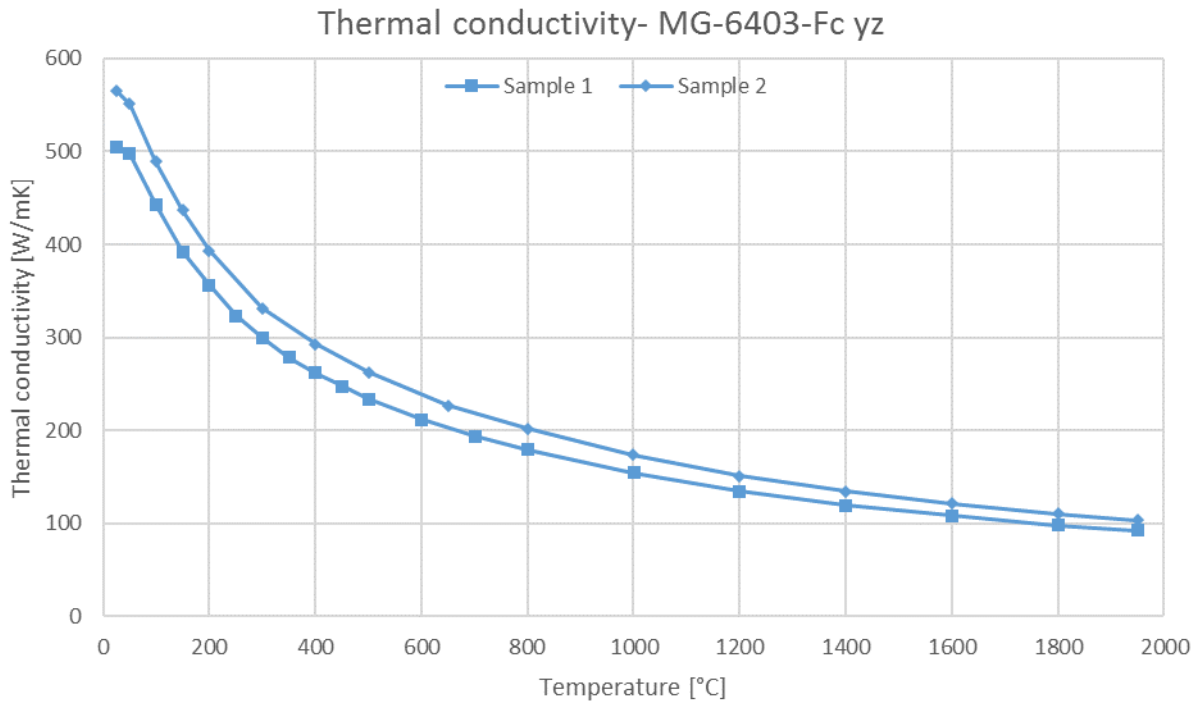

Figure 4.23 Thermal conductivity vs temperature of two MG-6403-Fc **yz** samples.

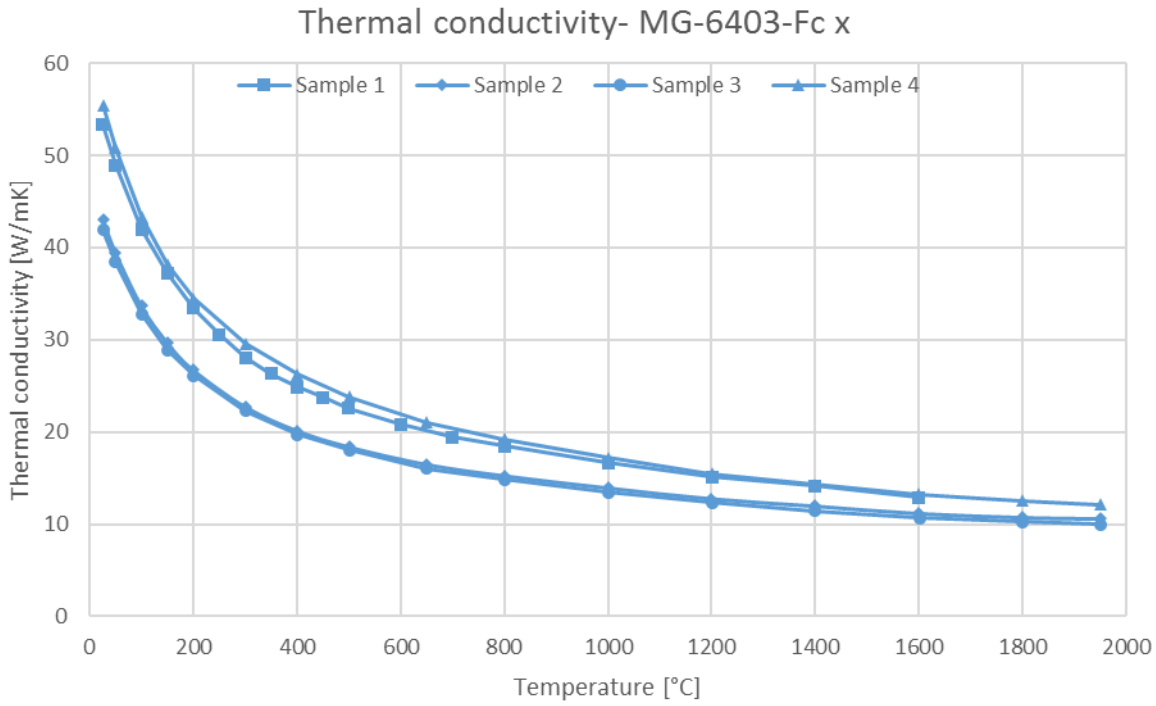

Figure 4.24 Thermal conductivity vs temperature of four MG-6403-Fc **x** samples.

4.2.2 Mechanical characterization

The mechanical characterization for this material consist in 4-point flexural tests and IET while the compressive behavior has not been investigated.

Flexural test

The test method is described in 3.3.1 with the fixture shown in Figure 3.10, over four *x* samples and five *yz* samples. The flexural stress versus strain curves, whose relationship is modeled by equation 2.41, are shown in the following Figure 4.25 and Figure 4.26. The values of maximum flexural stress and strain for each sample are collected in Table 4.7

Flexural properties		Stress to rupture [MPa]	Strain to rupture [μm/m]
yz	Sample 1	60.7	2763
	Sample 2	65.9	2155
	Sample 3	65.6	3027
	Sample 4	48.5	1620
	Sample 5	49.7	2610
x	Sample 1	10.4	4685
	Sample 2	11	4486
	Sample 3	10	5544
	Sample 4	11.8	2720

Table 4.7 Flexural properties of MG-6403-Fc.

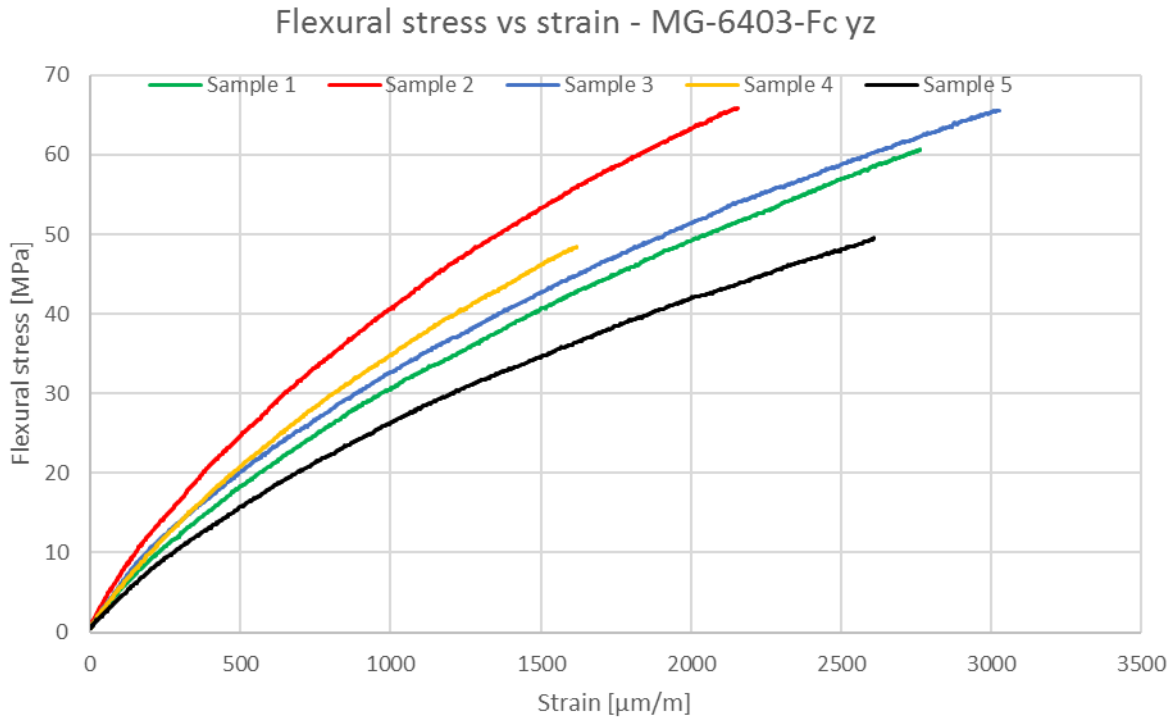

Figure 4.25 Flexural stress versus strain for five MG-6403-Fc **yz** samples.

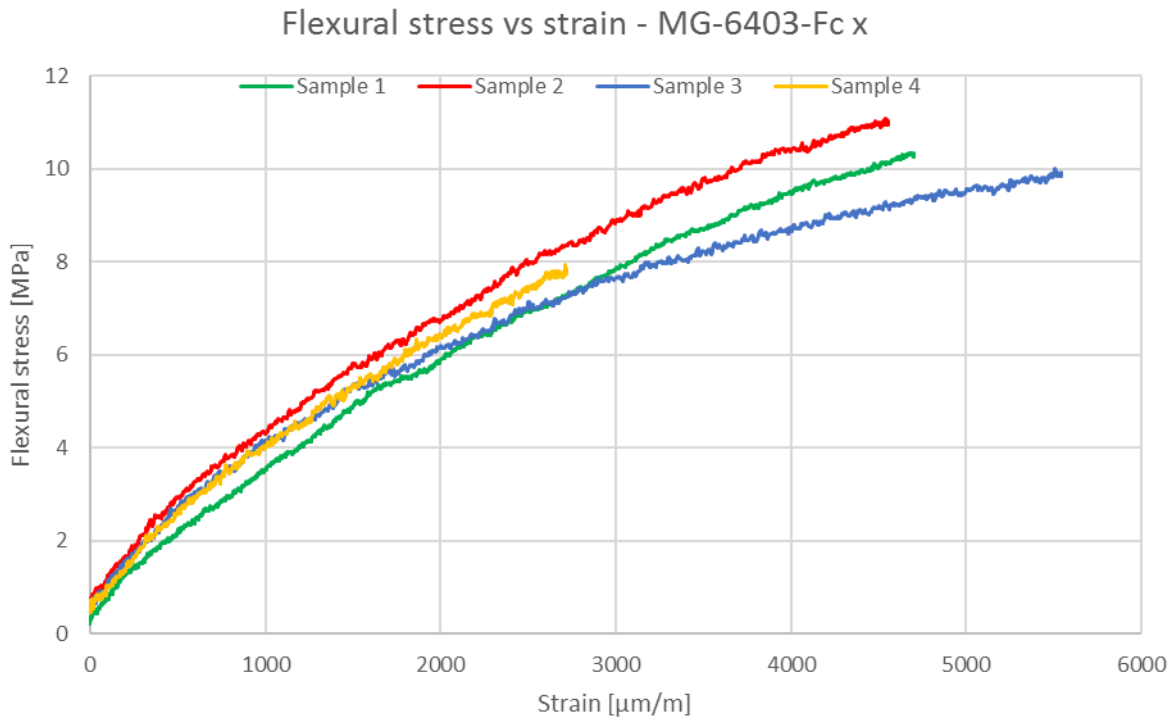

Figure 4.26 Flexural stress versus strain for four MG-6403-Fc **x** samples.

Impact excitation technique

The IET measurements have been done over the same samples available for the flexural tests. The method adopted is described in 2.2.2 while the set-up is shown in Figure 3.11. The first flexural modes were excited during the tests and their frequencies are stated in Table 4.8 and Table 4.9, together with the dimensions of the test specimens and the estimation of the Young's modulus in the hypothesis of elastic, homogeneous and isotropic material.

Sample yz	m [g]	L [mm]	b [mm]	t [mm]	ff [kHz]	E [GPa]
1	1.51	24.81	5.05	4.85	36.9	60.7
2	1.44	24.79	5.03	4.54	39.23	70.1
3	1.45	24.82	5.07	4.59	37.64	63.2
4	1.52	24.80	5.07	4.84	37.01	60.9
5	1.47	24.82	5.05	4.67	36.04	58.1

Table 4.8 Test specimens' mass and sizes, first flexural frequency and estimation of the Young's modulus (isotropic, homogeneous and elastic material) measured for MG-6403-Fc **yz** samples.

Sample x	m [g]	L [mm]	b [mm]	t [mm]	ff [kHz]	E [GPa]
1	3.33	24.95	9.93	5.03	8.28	3.37
2	1.88	24.95	5.68	5.08	8.54	3.45
3	1.56	25.05	5.09	4.79	8.12	3.40
4	1.65	25.00	5.09	5.04	8.81	3.69

Table 4.9 Test specimens' mass and sizes, first flexural frequency and estimation of the Young's modulus (isotropic, homogeneous and elastic material) measured for MG-6403-Fc **x** samples.

5 Discussion

In this part, the results shown in the previous chapter are discussed and analyzed from the point of view of the collimators' jaws required performances. The FoMs are evaluated and the critical properties compared with those of the previously developed materials.

5.1 CFC: general aspects

The CFC FS140® provided by the Japanese Tatsuno has been fully characterized both from the thermal and mechanical point of view, except for the IET analysis. The results obtained were in line with the expectation and the literature values stated for this composite. From the thermal point of view the material shows a very low CTE, typical of CFCs, which is negative in the direction parallel to the fibers up to ~ 1000 ℃ and below $0.7\ 10^{-6}K^{-1}$ at higher temperatures. In the direction x, perpendicular to the fibers it is below $11\ 10^{-6}\ K^{-1}$. The calorimetry analysis was limited to ~ 700 ℃, due to excessive noise in the DSC output signal: this results in non-ideal repeatability of the measurements. The noise was due to both oxidation and aged sample holder/furnace control issue. The values of specific heat at 25 ℃ were extrapolated from the c_p vs temperature curves and its average value is $717\ J/kgK$. Previous to the LFA analysis the samples were used to measure the density by means of an Archimedes' scale: during the measurement of the weight of the sample submerged in the ethanol, some liquid infiltrated in the voids of the materials, resulting in a slightly higher measured density. To avoid effects in the thermal diffusivity measurements the specimens were dried in a kiln at ~ 100 ℃ for almost

2 hours. The following LFA tests resulted unaffected. The thermal diffusivity is highly affected by the orientation: in the direction parallel to the fibers it is almost three times higher than perpendicularly: this fact, which also occurs in the MoGR composites, is linked to the properties of the graphene layers which are highly conductive in-plane and poorly conductive in the direction perpendicular to the planes. The same principle is valid when referring to the electrical conductivity: the measurements of electrical conductivity carried out in another laboratory following the standard test method ASTM C611 are stated in Table 5.1. The measurements were carried out perpendicularly and in two orthogonal direction in the plane: this was done because the currently used CFC AC150® showed anisotropy in the planes. The tests show that also CFC FS140® has different values of electrical conductivity in the plane.

As for the mechanical characterization, for the x samples it was not possible to obtain the strain to rupture in compression by means of the strain gauges which were not adequate to bear the strain occured. Consequently, the stress vs strain curves are incomplete and only the stresses to rupture could be measured. The Young's modulus evaluated with the IET cannot be stated with a known uncertainty due to the high damping of the material, which caused issues in the identification of the resonant frequencies. The material shows also radically different mechanical behaviors in the directions parallel and perpendicular to the fibers. The fibers act as a reinforcement, as can be deducted from the results of the flexural tests: the flexural stress to rupture measured for the parallel specimens ranges between $150 - 180\ MPa$. These values are more than 10 times higher than those measured in the perpendicular samples. The latter presents higher elongation. In Figure 4.15 it is clear how the fractures occurred in the two specimens. In the yz one the failure was due to the achievement of the admissible maximum stress of the fibers, which broke in distinct locations and resulted in a jagged surface. In the x samples the fracture consisted in the separation of layers, which are bonded with weak forces and results in a flat and uniform surface parallel to the basal planes. The material shows also higher stiffness in the direction of the fibers and the strain to rupture in this direction is almost half than that achievable in the perpendicular samples. The stress to rupture in compression has similar values in the two directions, since the fibers act as a reinforcement under tensile stresses. Therefore, in compression the behavior is mostly driven by the mechanical properties of the graphitic matrix. In the yz direction, the material shows a higher stiffness and the strain to rupture is limited: in Figure 4.12 it is possible to distinguish, as for the flexural tests, two diverse types of fracture. In the yz specimens, the fracture propagated along the planes that in this case were parallel to the loading direction. The x specimens showed a different surface of fracture typical of brittle materials. The higher strain achieved in the x samples can be explained

considering that the compression load is applied perpendicularly to the planes and tends to compact them, closing the voids, until the maximum admissible stress of the graphitic matrix is reached.

5.2 CFC: comparison

It is of paramount interest to compare the results of the characterization of CFC FS140® with those of the currently employed CFC AC150®, which was characterized in the Mechanical measurement laboratory in 2015. Some generic differences were known even before the characterization: the use of a different raw graphite, since Tatsuno changed the provider, which was the reason that justified the new characterization, and the final baking temperature. CFC AC150® was baked at 2800 °C while CFC FS140® at 2500 °C. From this latter information, it is possible to anticipate, prior to the tests, an expected lower thermal (and electrical) conductivity, that depends on the level of carbonization which in turn increases with the temperature. This expectation is confirmed by the measurements, as shown in Figure 5.1 and Figure 5.2:

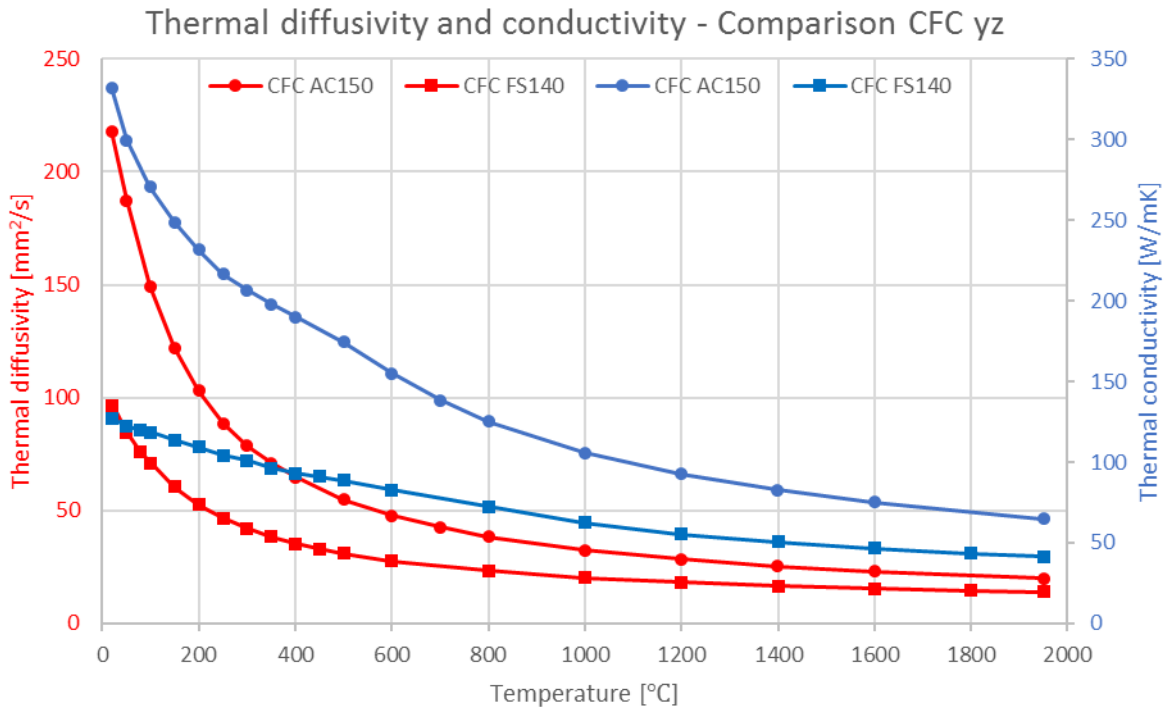

Figure 5.1 Comparison between CFC FS140® and CFC AC150® in terms of thermal diffusivity (red) and thermal conductivity (blue) in the **yz** direction.

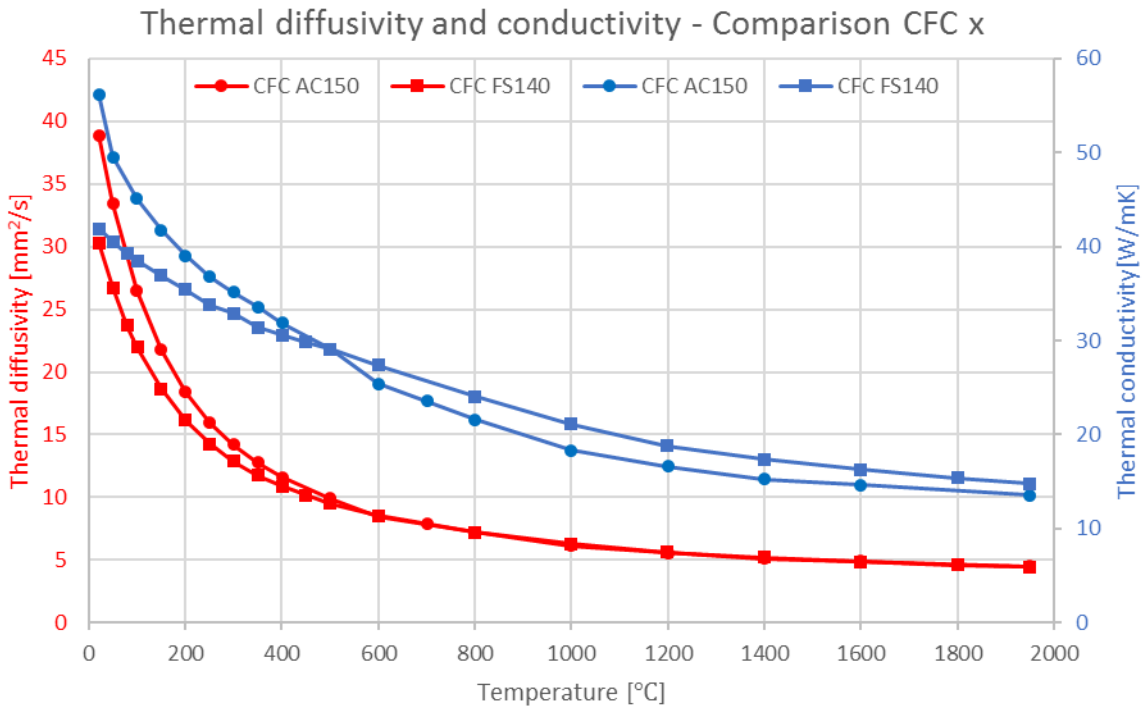

Figure 5.2 Comparison between CFC FS140® and CFC AC150® in terms of thermal diffusivity (red) and thermal conductivity (blue) in the **x** direction.

In the samples cut in the direction parallel to the fibers plane the thermal conductivity of the CFC FS140® is ~74% lower than the currently used CFC AC150®. The same decrease of properties can be noticed also for the electrical conductivity, in the three directions, as shown in Table 5.1.

Electrical conductivity [MS/m]	CFC AC150®	CFC FS140®
x	0.03	0.02
y	0.24	0.12
z	0.18	0.09

Table 5.1 Electrical conductivity of CFC FS140® and CFC AC150®. In the best direction, the electrical conductivity results ~50% lower than the older CFC.

From the thermal behavior point of view, only the thermal diffusivity/conductivity shows a substantial difference between the two materials while the other properties are comparable, as summarized in Table 5.2.

Property		Unit	CFC AC150®	CFC FS140®
Density at RT		g/cm^3	1.86-1.90	1.85-1.90
Specific heat	25℃	J/gK	0.755	0.724
	500℃		1.614	1.593
CTE_{yz}	RT-200℃	10^{-6} K^{-1}	-0.8	-0.97
	RT-500℃		-0.39	-0.51
	RT-1000℃		0.03	-0.07
	RT-1900℃		0.68	0.62
CTE_x	RT-200℃	10^{-6} K^{-1}	10.88	9.32
	RT-500℃		11.17	9.54
	RT-1000℃		11.64	9.93
	RT-1900℃		12.75	11.1
Thermal $diffusivity_{yz}$	20℃	mm^2/s	174	94
	500℃		42	30
Thermal $diffusivity_x$	20℃	mm^2/s	40	31
	500℃		10	9.6
Thermal $conductivity_{yz}$	20℃	W/mK	233	124
	500℃		126	85.7
Thermal $conductivity_x$	20℃	W/mK	54	42.5
	500℃		30	29

Table 5.2 Comparison of thermal properties between the CFC FS140® and CFC AC150®.

The mechanical characterization of CFC AC150® consisted in the flexural and compression tests. The comparison done with the available parameters is summarized in Table 5.3:

Property		Unit	CFC AC150®	CFC FS140®
Flexural strength	**yz**	MPa	104	165
	x		10	8.6
Flexural strain to rupture	**yz**	µm/m	1995	2850
	x		4287	4980
Compression strength	**yz**	MPa	70	98
	x		55	90
Compression strain to rupture	**yz**	µm/m	-	847
	x		-	-
Elastic modulus, E	**yz**	GPa	62	73
	x		-	-

Table 5.3 Comparison of mechanical properties between the CFC FS140® and CFC AC150®.

The new material shows slightly higher flexural properties in the direction of the fibers and higher strength in compression. In order to assess and compare the performance of the materials once embarked in the collimator's jaw the FoMs are evaluated.

FoM	CFC AC150®	CFC FS140®
TRI	1372	1943
TSI	47	28

Table 5.4 FoMs for CFC AC150® and CFC FS140®.

Despite the much lower thermal conductivity, the higher strength and strain to rupture lead to a more robust material with respect to the older one. On the other hand, the other two indexes, electrical conductivity and TSI, are lower for the new CFC FS140® and indicate a less stable material with a two times higher RF impedance.

5.3 MoGR

During both the thermo-physical and mechanical characterization of MG-6403-Fc, no particular issue or unexpected results were encountered, therefore the most interesting aspect is the comparison with the previously developed materials. Among these, two promising grades are chosen for the comparison: MG-6403-Ga and MG-6451-Aa, whose composition and production parameters are described in 1.6.2. The main difference in the production process between the two old grades and the one object of the characterization consists in the temperature of post-sintering. For MG-6403-Fc the post-sintering temperature was 2600 °C against the 2100 °C of its predecessors. This temperature is above the melting point of the molybdenum carbides, which in this step would melt again but in a pressure less condition. This might release the internal stresses raised during the hot-pressing cycle. To better understand this effect, it is useful to compare the residual deformation of the materials. Specifically, the residual deformation is here conventionally defined as the change of length measured on the dilatometry specimens after the dilatometry tests. The results, reported in Table 5.5, suggest that higher temperatures of post-sintering allow more release of internal stresses. The measurements show also that the material is always geometrically more stable in the direction parallel to the basal planes (yz).

Material		Residual deformation (%)
MG-6403-Ga	yz	0.02
	x	0.18
MG-6541-Aa	yz	0.02
	x	0.14
MG-6403-Fc	yz	< res.
	x	0.12

Table 5.5 Residual deformation of the dilatometry specimens for the three MoGR grades considered.

The other thermo-physical properties (together with the electrical conductivity) are collected in Table 5.6.

Property		Unit	MG-6403-Ga	MG-6451-Aa	MG-6403-Fc
Density at RT		g/cm^3	2.492	2.490	2.586
Specific heat	25℃	J/gK	0.604	0.643	0.624
	500℃		1.369	1.505	1.325
CTE_{yz}	RT-200℃	10^{-6} K^{-1}	2.03	2.31	2.56
	RT-500℃		2.32	2.44	2.91
	RT-1000℃		2.24	2.27	2.95
	RT-1900℃		2.08	2.06	2.73
CTE_x	RT-200℃	10^{-6} K^{-1}	9.26	10.04	8.57
	RT-500℃		10.2	11.04	9.32
	RT-1000℃		12.49	13.55	11.09
	RT-1900℃		17.52	18.43	15.36
Thermal $diffusivity_{yz}$	20℃	mm^2/s	364	317	353
	500℃		75.4	74.5	70.7
Thermal $diffusivity_x$	20℃	mm^2/s	37.0	28.1	30.6
	500℃		7.0	5.4	5.9
Thermal $conductivity_{yz}$	20℃	W/mK	547	507	547
	500℃		257	279	241
Thermal $conductivity_x$	20℃	W/mK	55.7	44.9	47.4
	500℃		23.8	20.1	20.3
Electrical $conductivity_{yx}$	25℃	MS/m	0.88	0.98	0.91
Electrical $conductivity_x$	25℃	MS/m	0.08	0.06	0.07

Table 5.6 Comparison of thermo-physical properties and electrical conductivity between three MoGR grades.

Overall the new grade MG-6403-Fc shows thermo-physical properties in line with those of the previous developed grades: the specific heat, thermal diffusivity, thermal conductivity and electrical conductivity are in between those of the predecessors. The materials result slightly denser and it has a higher CTE in the parallel direction, while it is lower in the perpendicular direction. The latter fact suggests a more isotropic nature.

The mechanical properties are listed below:

Property		Unit	MG-6403-Ga	MG-6451-Aa	MG-6403-Fc
Flexural strength	**yz**	MPa	73.5	79.5	61.1
	x		11.6	12.4	8.1
Flexural strain to rupture	**yz**	µm/m	2643	1910	2161
	x		4431	7065	4881
Elastic modulus, E	**yz**	GPa	64.9	85.8	61.4
	x		4.1	4.5	3.7

Table 5.7 Comparison of mechanical properties between three MoGR grades.

The material shows a flexural strength about 20% lower than the stronger grade and a modulus of elasticity about 30% smaller than the stiffer one. The analysis of these data shows that the addition of CF to the grade MG-6541-Aa, results in a higher strength but also a greater stiffness.

To compare the grades in terms of performance when employed as collimators absorbing materials it is necessary to evaluate their FoMs, see Table 5.8:

FoM	MG-6403-Ga	MG-6451-Aa	MG-6403-Fc
TRI	274.1	226	237
TSI	43.3	37.4	42.6

Table 5.8 FoMs for MG-6403-Ga, MG-6541-Aa and MG-6403-Fc.

Among the previous grades of MoGR, the candidate MG-6403-Fc averages the two predecessors. With respect to MG-6403-Ga it shows both lower TRI and TSI. TRI is lower due to the higher expansion and slightly lower strength, while the TSI is smaller because of the higher density and the lower thermal conductivity. Despite showing the best mechanical properties, the grade MG-6451-Aa has the lower TRI index, explainable with the higher CTE (in both directions). The overview of the performance parameters suggests that the modification of some production variables adopted to realize the new MG-6403-Fc (that has the same composition of MG-6403-Ga), doesn't bring to a more performing material. Therefore, improvement of this material should be sought in other aspects, such as ultra-high vacuum performances and radiation hardness.

6 Conclusions

Two ceramic-matrix composites, candidate for their use in the primary and secondary collimators jaws of the LHC, were characterized and assessed in terms of Figures of Merit, to rank their performances once embarked in the collimators. CFC FS140®, produced by the Japanese Tatsuno, is considered, since the CFC AC150®, also produced by the Asiatic company, had already been successfully employed for beam cleaning purposes at CERN. Carbon fibers – carbon materials show a good beam impact robustness and are often suitable materials for thermal management and nuclear plants devices. The reason which lead to a new characterization of the CFC was the different raw material and thermal treatment chosen by Tatsuno in recent years. The other material object of the study, MG-6403-Fc, is a molybdenum carbide reinforced graphite, realized within a collaboration with the Italian SME BrevettiBizz, that gave birth during years to more than 15 materials. The aim of the collaboration is to develop materials with some qualities typical of ceramic composites, such the already mentioned beam impact resistance but also low coefficient of thermal expansion, and increased thermal and electrical conductivities, the latter being of paramount importance to reduce the radio frequency impedance of the devices. After describing the models and the principles behind the measuring technique, the instruments and the test parameters are developed and finally the results of the characterization of both materials are stated.

The results of the analysis of the CFC FS140® shows some worse properties with respect to the older one. Both thermal and electrical conductivity are lower: at room temperature, the thermal conductivity is ~74% lower and the electrical conductivity ~50% lower. This can be explained

with a lower level of graphitization of the newer material, as a consequence of the lower final baking temperature: 2500 °C against 2800 °C of the CFC AC150®. On the other hand, the material shows increased mechanical properties, both in terms of flexural and compressive strength and elasticity modulus.

The development of the molybdenum carbide graphite leads actually to materials with the desired properties: generally, these materials show low enough CTE and higher thermal and electrical conductivity than CFCs (up to 5 times higher electrical conductivity). The liquid phase sintering process, permits to obtain high densification, thanks to the infiltration of liquid carbides in the voids, and catalytic graphitization, responsible of the highly oriented graphitic matrix. The results of MG-6403-Fc characterization are compared to those of two previously developed promising grades, with similar composition but slightly different production process (in the newer the post-sintering temperature is above the melting temperature of the molybdenum carbides and the atmosphere is air). Overall the material shows similar behavior and mean values of TRI and TSI, suggesting to look for improvement in other parameters of the synthesis.

The following Table 6.1 collect the FoMs of the tested material CFC FS140® and MG-6403-Fc, of the currently used CFC AC150® and of two others promising MoGR grades.

FoM	CFC AC150®	CFC FS140®	MG-6403-Ga	MG-6451-Aa	MG-6403-Fc
TRI	1372	1943	274.1	226	237
TSI	47	28	43.3	37.4	42.6
RFI	0.24	0.12	0.88	0.98	0.91

Table 6.1 Overview of the FoMs for the tested materials (CFC FS140® and MG-6403-Fc), the currently employed CFC AC150® and two other promising MoGR grades.

It is important to notice that both the CFC and MoGR are valid material for their use in the primary and secondary collimator and the choice of one of them does not discard the use of the other one. Nowadays, more than 100 collimators are installed and among these, for example, there are more than seven different versions of primary and secondary collimators. In fact, being impossible to find a jaw material with all the desired properties, it is often necessary to use different material in combination. Therefore, while a baseline is fixed a small number of special collimators would be installed in key point of the LHC to perform specific tasks, without affecting the overall collimation system performance. Moreover, the FoMs are not the criteria of choice among the materials but they represent a first criteria to select that materials worth to be simulated and submitted to further tests, like the outgassing test. So far, the baseline of the production of the new primary and secondary collimators has been identified with a grade of

MoGR, while the CFC ones would be produced as backup or where a lower dense collimator jaws is needed.

Future works

In the light of the results obtained, further steps must be done:

- Order another grade of CFC baked at higher temperature, to check if the thermal and electrical conductivity increase to acceptable values.
- Perform the tests over CFC along two directions in the plane of the fibers, due to the anisotropy found during the characterization of the old CFC AC150® and also during the current electrical conductivity measurements.
- Focus the parametric studies of the production of MoGR according to the latest results.

At CERN, in the framework of this R&D project, further investigations of the beam intercepting devices' materials are carried out, for example the observation of their behaviors when subjected to the proton beam. Experiments run in the High Radiation to Materials (HiRadMat) facility, are periodically conducted on the most promising batches of materials, and the next one is scheduled for fall 2017. In this facility, high-intensity pulsed beams (440 GeV) are provided to an irradiation area were materials samples are arranged inside a structure similar to the one in Figure 6.1.

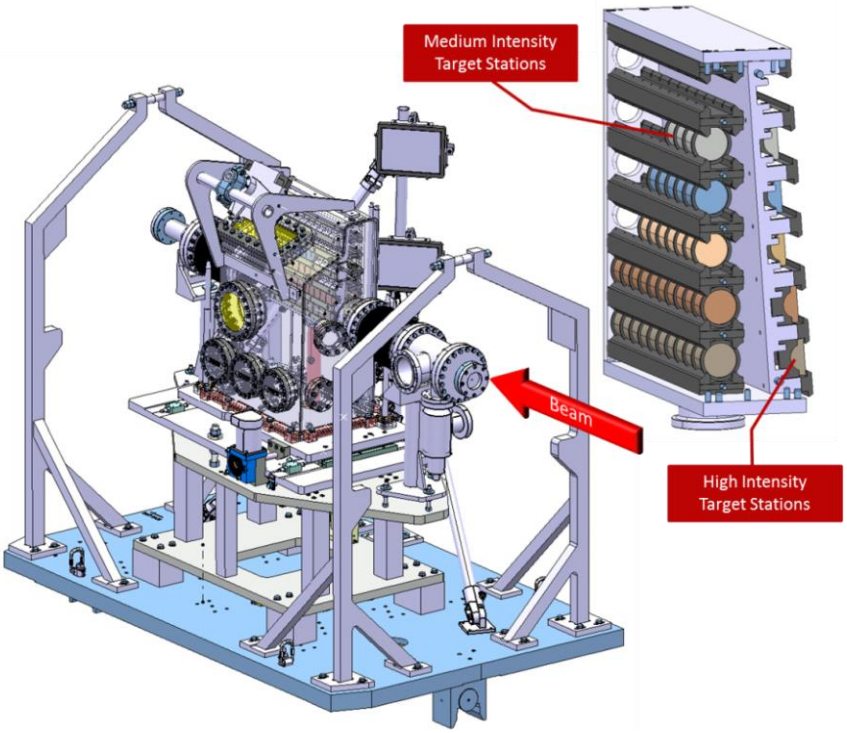

Figure 6.1 Overview of the HRMT-14 experiment test bench.

The samples are instrumented by the Mechanical measurement laboratory, which by means of thermocouples, strain gauges, high speed camera and laser doppler vibrometer, is able to provide data about shock waves, deformation, vibration, temperature increase and heat dissipation. The two materials object of this study, will be tested in the facility and the results of the observation will be of paramount importance to validate and develop the models, and to experience the actual behavior under operation and catastrophic scenario.

Currently it is also possible to perform mechanical tests (tensile, compression and bending tests) from room temperature to 1200 °C, thanks to the recent implementation of an electric furnace and laser extensometer system on the universal testing machine Zwick Z400 already installed in the mechanical measurement laboratory. This will allow to track the mechanical properties modification of the materials with the temperature in the range of temperatures actually reached during operation in the collimators.

Appendix

Working principle of a thermocouple

A thermocouple is a transducer that senses temperature gradient and converts it in an electric signal. The thermocouple is an electrical circuit realized with two conductors, made of different materials, which are joined at one of their extremities. The physical principle at the basis of its functioning is the Seebeck effect: when there is a temperature difference between the ends of the described circuit, a potential difference arises. This effect is also known as thermoelectric effect.

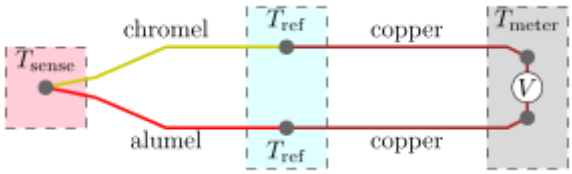

Figure A. 1 Scheme of a thermocouple: hot weld on the left side and cold junction of the right side.

The point where the conductors are joint is called measurement junction or hot weld, and it is the sensitive part of the sensor. The other two extremities represent the cold junction, and it is where the potential difference is measured. The hot weld is at the unknown temperature T_{sense}, while the cold junction is at a reference (known) temperature T_{ref}. The potential difference is proportional to the temperature gradient between the two junctions in a non-linear fashion:

$$\Delta T = \sum_{i=1}^{N} a_n V^n$$

Where the coefficients a_n depend on the materials used and N is chosen according to the level of precision desired. There are several different types of thermocouples, made out of different combinations of alloys, whose use depends upon melting point, chemical properties, stability, cost, output etc. The types installed in the instrument employed for the characterization are described in the table below.

Type	Instrument	Materials	Output [mV/°C]	Range of temperature
W3%Re-W25%Re	LFA, DIL	Tungsten - Rhenium	4	0 - 2325 °C
S	DSC	Platinum - Rhodium	7	0 - 1650 °C

Working principle of a LVDT

The linear variable differential transformer is an electromechanical transducer which converts a linear displacement into an electrical signal. It is an absolute output device: in case of power cut the output signal after the restarting remains the same than before. Consequently, the null point repeatability is extremely high. This sensor is composed by three solenoidal coils placed around a tube in which a ferromagnetic core can move, see Figure A. 2. The central coil is the primary, the two lateral are the top and bottom secondary coils, and they are simetrically positioned with respect to the primary. The core is mechanically linked to the object whose displacement is of interest.

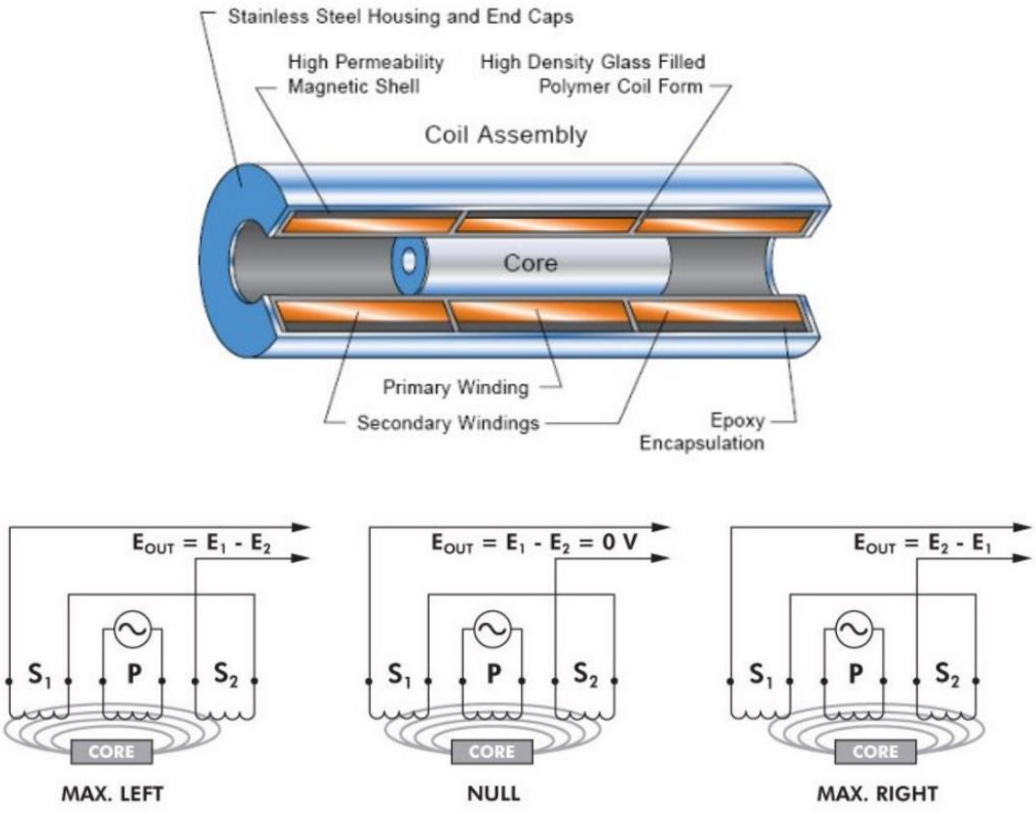

Figure A. 2 LVDT's components and electrical circuits scheme. Credits **(22)**.

The primary coil is driven by an AC current of constant amplitude and frequency ranging between 1 to 10 kHz: this generates an alternating magnetic field which induces an electric signal on the two secondary coils, depending on the position of the core. When the core is at the center, the same voltage is induced on the secondary coils, and the output signal is zero. As the core moves, the mutual inductions between the primary and the secondary coils differ and the output signal is positive or negative according to the displacement direction. The output of the LVDT is very linear within a specified range of core motion.

Working principles of a strain gauge

The strain gauge is a sensor widely used to measure the strain of an object, converting the strain in an electrical output signal. The most common type of strain gauge is composed by a metallic foil pattern (3÷6 μm thick) embedded in an insulating support film. The working principle is based on the definition of electrical resistance R of a conductor:

$$R = \rho_{el} \frac{L}{A}$$

Where ρ_{el} is the electrical resistivity of the material, L the length of the active coil and A its section area. When the strain gauge is glued on the test specimen it is subjected to the same strain than the surface, therefore it changes its length and its cross section: if stretched it will become longer and narrower.

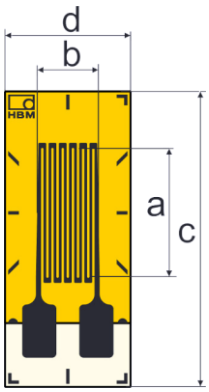

Figure A. 3 Strain gauge. Credits HBM.

Measuring R allows to evaluate the strain of the test piece. The sensitivity to the measured strain is given by the gauge factor GF:

$$GF = \frac{\Delta R/R_0}{\Delta L/L_0} = \frac{\Delta R/R_0}{\epsilon}$$

The gauge factor can be expressed as a function of the Poisson's ratio of the conductor material:

$$GF = \frac{\Delta \rho/\rho}{\epsilon} + 1 + 2\nu$$

Measured strain are rarely larger than millistrain, which results in very small changes in R. To measure tenths of Ohms, the strain gauge is configured in a Wheatstone bridge.

Wheatstone bridge

The Wheatstone bridge is a two legs electrical circuit: one leg contains one known resistance and the unknown resistance (for example the strain gauge), the other leg contains two known resistances, one of them variable.

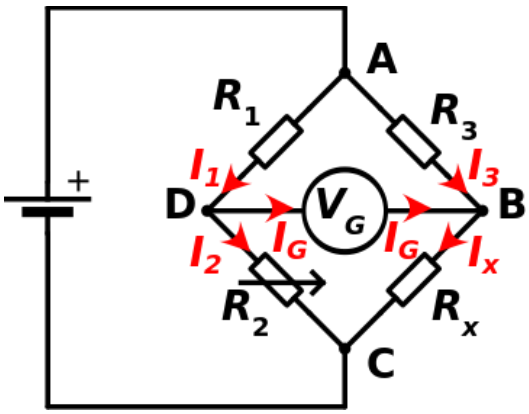

Figure A. 4 Wheatstone bridge circuit.

In Figure A. 4, V_G is the voltage across the bridge (measured input quantity), R_1 and R_2 are the known constant resistances, R_x the unknown resistance of the component and R_2 is the variable resistance. The exciting voltage is V_s.

Kirchhoff's first rule to junction B and D leads to:

$$I_3 + I_G - I_X = 0$$

$$I_1 - I_G + I_2 = 0$$

And Kirchhoff's second rule to the loops ABD and BCD:

$$I_1 R_1 + I_G R_G - I_3 R_3 = 0$$

$$I_2 R_2 - I_X R_X - I_G R_G = 0$$

When the bridge is balanced, $I_G = 0$ and the above equations lead to:

$$I_3 R_3 = I_1 R_1$$

$$I_x R_x = I_2 R_2$$

From which:

$$R_X = \frac{R_3 R_2}{R_1}$$

The measured tension in the bridge is:

$$V_G = \left(\frac{R_2}{R_1 + R_2} - \frac{R_x}{R_3 + R_x}\right) V_s$$

The R_2, can either be adjustable or not: when using strain gauges and resistance thermometer, R_2 is normally not adjustable because it is faster to read the voltage across the bridge than to adjust the resistance to balance the bridge.

Working principle of a load cell

A load cell is an electro-mechanical transducer able to convert a force acting on it in an electrical output signal. There are several types of load cell, based on different principle of sensing the force. For example, resistive load cells correlate the entity of the force by measuring the induced strain on the device, while capacitive load cells are based on the principle of change of capacitance when a voltage is applied to the sensor. All the load cells used in the mechanical characterization of MG-6403-Fc and CFC FS140® are resistive load cells relying on the deformation measured through strain gauges. For example, in the load cell shown in Figure A. 5 four strain gauges have been installed and when the load F is applied, two of them will be in compression and two in traction.

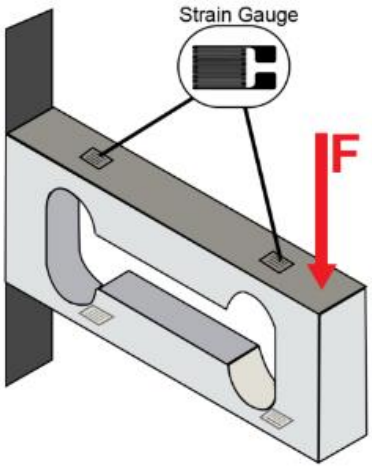

Figure A. 5 Load cell scheme and position of the strain gauges. **(23)**

The four strain gauges are installed in a Wheatstone bridge. Knowing the relationship between the state of tension and strain in the points of installation of the gauges allows to correlate the electrical reading of the bridge to the force applied.

Uncertainty of a measurement

Measuring is not an exact science, and repeated measurement of the same dimension lead to different values. All the results of a measurement are affected by errors, of unknown amplitude, therefore the result of the measurement itself is dispersed around the “true" value of the measurand. The uncertainty of a measurement expresses the lack of knowledge of the value of the measurand. When reporting the result of a measurement it is always good practice to express it as its best estimate plus/minus its uncertainty. Before describing the two types of uncertainties, it is useful to recall some statistics definition:

Probability, p: a real number in the range 0-1, associated to a random event.

Random variable, X: a variable which can assume any of the values of a set, associated to a probability distribution.

Probability distribution: a function that expresses the probability that a random variable takes any given value or belong to a range of values

Distribution function, F: a function giving for every value x of the set the probability that the random variable X is equal to or less than x.

$$F(x) = Pr(x \leq X)$$

Probability density function, p(x): is the derivative of the distribution function. Example:

$$P(a < x < b) = \int_a^b p(x)dx$$

Expectation (expected value, mean), μ:

for a discrete random variable $\mu = E(x) = \sum_{i=1}^{N} p_i x_i$

for a continuous random variable $\mu = E(x) = \int_{-\infty}^{+\infty} xp(x)$

Variance, σ^2: is the expectation of the square of the centered random variable.

$$\sigma^2 = E\big[\big(X - E(X)\big)\big]$$

Standards deviation, σ: $\sqrt{\sigma^2}$

Gauss distribution (normal distribution):

$$p(x) = \frac{1}{\sqrt{2\pi}\sigma} \exp\left(-\frac{x-\mu}{2\sigma^2}\right)$$

Confidence interval for Gauss distribution:

- 1σ: $P[(\mu - \sigma) < x < (\mu + \sigma)] = 68.3\%$
- 2σ: $P[(\mu - 2\sigma) < x < (\mu + 2\sigma)] = 95.5\%$
- 1σ: $P[(\mu - 3\sigma) < x < (\mu + 3\sigma)] = 99.7\%$

Estimation: operation of assigning, from the observation of in a sample, numerical values to the parameters of a distribution chose as the statistical model of the population from which this sample is taken.

Arithmetic mean, $\bar{x}$: it is an estimate for the expectation.

$$\bar{x} = \frac{1}{n}\sum_{k=1}^{n} x_k$$

Estimation of the variance: $s^2(x_i) = \frac{1}{n-1}\sum_{k=1}^{n}(x_i - \bar{x})^2$

Variance of the arithmetic mean: $s^2(\bar{x}) = \frac{s^2(x_i)}{n}$

Standard deviation: positive square root of the variance.

Covariance: represent the measure of the mutual dependence between two random variables y and z.

$$cov(y,z) = E\big[\big(y - E(y)\big)\big(z - E(z)\big)\big]$$

Degree of freedom, ν: $\nu = n - 1$

Type A uncertainty

Let's consider the case in which n independent observation of the measurand x_k have been done under the same conditions. The best estimate of the measurand is the arithmetic mean of the observed values, $\bar{x}$. The experimental standard deviation of the mean, $s(\bar{x})$ represent the uncertainty associated to the best estimate of the measurand:

$$s(\bar{x}) = \frac{s(x)}{\sqrt{n}} = \sqrt{\frac{1}{n(n-1)}\sum_{k=1}^{n}(x_k - \bar{x})^2}$$

The result of the measurement can be reported as:

$$x = \bar{x} \pm u_A = \bar{x} \pm \frac{s(x)}{\sqrt{n}}$$

Relative uncertainty, u_r: $u_r(y) = u(y)/\bar{y}$, it is dimensionless and allows to compare uncertainties associated to measurand of different nature.

Expanded uncertainty, U: it refers to an interval of values around $\bar{x}$, where it is expected to find the measurand with a certain probability.

$$U = Ku$$

Where k is the coverage factor (for a Gauss distribution, $k = 2$ produces an interval having a level of confidence of 95%, $k = 3$ of approximately 99%).

Type B uncertainty

If repeated measurements have not been taken, the estimate of the measurand and of its variance must be done by scientific judgment based on available information, like:

- Previous measurement data
- Knowledge or experience of the behavior of the measurand
- Manufacturer's specification
- Data provided in calibrations or other certifications
- Uncertainties assigned to reference data taken from handbook

It is needed to:

1. Define an interval around the expected value, with an associated probability to find the values of the measurand.
2. Define a probability distribution function (example: Gauss, triangular or uniform)
3. Evaluate expectation, variance and standard deviation

Uniform probability distribution function: the interval around the expected value a_0, has a width of $2a$. The probability is:

$$p(x) = \begin{cases} 0, x < a_0 - a \\ \frac{1}{2a}, a_0 - a < x < a_0 + a \\ 0, x > a_0 + a \end{cases}$$

The other parameters are:

$$\mu(x) = \int_{-\infty}^{+\infty} x \frac{1}{2a} dx = a_0$$

$$\sigma^2(x) = E\left[\left(x - \mu(x)\right)\right] = \frac{\Delta x^2}{12}$$

$$\sigma = \frac{\Delta x}{\sqrt{12}}$$

Triangular probability distribution: the interval around the expected value a_0 has a width of $2a$. The parameters of the distribution are:

$$\mu(x) = a_0$$

$$\sigma^2(x) = \frac{\Delta x^2}{24}$$

$$\sigma = \frac{\Delta x}{\sqrt{24}}$$

The uncertainty of the triangular distribution is lower than the one of the uniform distribution.

Combined standard uncertainty

Direct measurement: $u_c^2(x) = u_A^2(x) + u_B^2(x)$

Indirect measurement

The quantity of interest y rises from a combination of N measured quantities x_i, which are the input parameters:

$$y = f(x_1, x_2, \dots, x_N)$$

The estimated value of y is simply obtained substituting in f the estimated $\overline{x_i}$. The uncertainty of $\bar{y}$, is a combination of the uncertainty of the x_i.

$$u_C\ (y) = \sqrt{\sum_{i=1}^{N} \left(\frac{df}{dx_i}\right)^2 u^2(x_i) + 2 \sum_{i=1}^{N-1} \sum_{j=i+1}^{N} \left(\frac{df}{dx_i}\right)\left(\frac{df}{dx_j}\right) u(x_i, x_j)}$$

Where we can define the sensitivity coefficient:

$$c_i = \left(\frac{df}{dx_i}\right)_{\bar{y}}$$

And the correlation coefficient:

$$r_{ij(x_i,x_j)} = \frac{u(x_i, x_j)}{u(x_i)u(x_j)} \in [-1; 1]$$

$r_{ij} = 0$ if the input parameter are statistically independent. With these coefficients it is possible to write another expression for the combined uncertainty:

$$u_C\,(y) = \sqrt{\sum_{i=1}^{N} c_i^2 u^2(x_i) + 2\sum_{i=1}^{N-1}\sum_{j=i+1}^{N} c_i c_j r_{ij} u(x_i)u(x_j)}$$

Specific cases:

- $\boldsymbol{r_{ij} = 0}$**, independent variables:** $u_c(y) = \sqrt{\sum_{i=1}^{N}\left(\frac{df}{dx_i}\right)^2 u^2(x_i)}$
- $\boldsymbol{\bar{y} = n_1\bar{x}_1 \pm n_2\bar{x}_2 \pm \cdots \pm n_N\bar{x}_N}$**:** $u_c(y) = \sqrt{\sum_{i=1}^{N} n_i^2 u^2(x_i)}$
- $\boldsymbol{\bar{y} = \bar{x}_1^{n_1} * \bar{x}_2^{n_2} * \ldots * \bar{x}_N^{n_N}}$**:** $u_{r,C}(y) = \sqrt{\sum_{i=1}^{N} n_i^2 u_r^2(x_i)}$ and if $n_i = \pm 1$, $u_{r,C}(y) = \sum_{i=1}^{N} u_r^2(x_i)$.

References

[1] https://cds.cern.ch/record/1092437/files/CERN-Brochure-2008-001-Eng.pdf, 14/01/2017

[2] https://lhc-machine-outreach.web.cern.ch/lhc-machine-outreach/beam.htm, 1401/2017

[3] https://lhc-machine-outreach.web.cern.ch/lhc-machine-outreach/components/ magnets.htm, 14/01/2017

[4] S. Redaelli, https://lhc-collimation.web.cern.ch/lhc-collimation/files/SRedaelli_HB2006_1.pdf, 2006

[5] A. Bertarelli et al., https://lhc-collimation-upgrade-spec.web.cern.ch/lhc-collimation-upgrade-spec/Files/Misc/ABertarelli_HB2014_NovelMaterials_paper.pdf, 2014

[6] A. Oya, H. Marsh, “Review - Phenomena of catalytic graphitization”, Joural of materials science, no. 17, 1982

[7] Harada, Y., “Graphite-Metal Carbide Composites”, 1966

[8] R. B. Matthews, G. M. Jenkins, “The high temperature interaction between molybdenum and graphite”, Journal of material science, no. 10, 1975

[9] O'Neill, M. J., “Measurement of specific heat functions by differential scanning calorimetry”, Analytical Chemistry, vol. 38, no. 10, 1966

[10] J. D. James, J. A. Spittle, S. G. R. Brown, R. W. Evans, “A review of measurement techniques for the thermal expansion coefficient fo metals and alloys at elevated temperatures”, Measurement science and technology, VOL. 12, 2001

[11] W. J. Parker, R. J. Jenkins, C. P. Butler and G. L. Abbot, “Flash method of determining thermal diffusivity, heat capacity and thermal conductivity”, Journal of Applied Physics, vol. 32, no. 9, 1962

[12] Cowan, Robert D., “Pulse method of measuring thermal diffusivities at high temperatures”, Journal of applied physics, vol. 36, no. 4, 1963

[13] Lehman, J. A. Cape and G. W., “Temperature and finite pulse time effects in the flash method for measuring thermal diffusivity”, Journal of applied physics, vol. 34, no. 7, 1963

[14] Taylor, L. M. Clark and R. E., “Radiation loss in the flash method for thermal diffusivity”, Journal of applied physics, vol. 46, no. 2, 1975

[15] J. D. Lord, R. Morrell, “Elastic modulus measurement”, Measurement Good Practice Guide No. 98, February 2007

[16] ASTM International, “E228 -11 Standard test method for linear thermal expansion of solid materials with a push-rod dilatometer”, 2011

[17] ASTM International, “E2585-09 Standard practice for thermal diffusivity by the flash method”, 2009

[18] DEUTSCHE NORM, “DIN 51 007 General principles of differential thermal analysis”, 1994

[19] ASTM, “Standard test method for compressive strength of carbon and graphite”, 1991

[20] ASTM International, “ASTM C1161 Standard test method for flexural strength of advanced ceramics at ambient temperature”, 2002

[21] ASTM, “ASTM C1259: Standard test method for dynamic Young’s modulus, shear modulus, and Poisson’s ratio for advanced ceramics by impulse excitation of vibration”, 2001

[22] http://www.te.com/usa-en/industries/sensor-solutions/insights/lvdt-tutorial.html#chapter-2-dl, 28/02/2017

[23] http://www.loadstarsensors.com/what-is-a-load-cell.html, 14/03/2017

Bibliography

* N. Mariani, “Development of novel, advanced molybdenum-based composites for high energy physics application”, Doctoral Dissertation, 2014
* P. Di Marco, Handouts of Applied Thermofluidodynamics classes, 2006
* Robert C. Juvinall, Kurt M. Marshek, “Machine Component Design”, Wiley, 5th Edition International Student Version, 2012
* Evaluation of measurement data — Guide to the expression of uncertainty in measurement, JCGM 100:2008 GUM 1995 with minor corrections, First edition September 2008

List of figures

List of tables